Electron Quantum Interference in Small Metal Wires and Loops

A Dissertation

Presented to the Faculty of the Graduate School

of

Yale University

in Candidacy for the Degree of

Doctor of Philosophy

by

Venkat Chandrasekhar

May 1989

Acknowledgements

It is with pleasure that I acknowledge the support and advice of the many people with whom I have had interactions during my time at Yale.

To Professor Dan Prober, my thesis advisor, I owe my progress towards refinement as a physicist. His support and advice have been essential, and his insistence on clarity of thought and presentation, as well as his physical insight into complex problems, have succeeded many times in turning obtuse notions into concrete results.

P. Santhanam, Shalom Wind and Michael Rooks have been closely associated with much of the work in this thesis. Between them, they have taught me the folklore of the field and the necessary experimental techniques. Santhanam introduced me to the twin mysteries of quantum interference and microlithography, and has remained a collaborator through the years. Shalom Wind taught me, with patience and understanding, the many secret ways of experimental life in DProberLab. Michael Rooks' hard work in device fabrication and expertise in electron-beam lithography were essential to the experiments in this thesis. Michael set up the electron-beam writer at Yale, and both Michael and Shalom taught me how to make full use of it. Working on these experiments with them has been an enjoyable experience.

Professor R.G. Wheeler's office door I have always found to be open, whether it was for discussing questions of physics or The Commercial Applications of High Temperature Superconductivity. Professor Subir Sachdev has listened to and answered patiently my incessant questions on Fermi liquid theory. I also thank Professors Dan Prober, R.G. Wheeler, A.D. Stone and Subir Sachdev for being on my thesis committee,

and Professor S.C. Feng for agreeing to be my outside reader.

Dean Face and Elie Track were senior graduate students who provided both the technical expertise and the general philosophy to keep DProberLab going. Tom Kopley, apart from helping me improve my game of squash, also provided the oxidised silicon substrates on which the later samples were fabricated. Chris Tigges was a reliable source of experimental advice and chocolate chip cookies. Steve Klepper did the electron-beam lithography for the Au loops discussed in this thesis. Steve, along with Hodge Worsham, Paul Dresselhaus and Paul McEuen, also made sure that the equipment in the lab kept humming.

Much of the equipment used in the experiments, from cryostats to mask holders, were made or worked on by Clif Sneider. The late June Yarosh did a phenomenal job of taking care of paperwork, and her efficiency masked many of the bureaucratic entanglements of complex tasks like ordering equipment. Dr. Alan Pooley took scanning electron micrographs of many of the samples in this thesis. Jayne Miller provided help with a number of administrative details, big and small; her sources of chocolate are impeccable. Administrative help was also provided by Linda Schwarz and Arline Bjorkli.

Funding for this work was provided primarily by National Science Foundation Grant No. DMR-8505539, and also ECS-8509135. Support for the microlithographic facilities at Yale was provided by National Science Foundation Grant No. DMR-8213080, IBM Corp., Shipley, Inc., and Yale University.

Finally, I would like to thank my family and my fiancee, Melodie Swanson, for their strong support and encouragement through my years at graduate school.

Table of Contents

List of Abbreviations and Symbols

1D	One dimensional
2D	Two dimensional
AL	Aslamazov-Larkin
DUV	Deep ultra-violet
IPA	Isopropyl alcohol
MIBK	Methyl isobutyl ketone
MR	Magnetoresistance
MOSFET	Metal oxide semiconductor field effect transistor
MT	Maki-Thompson
MW	Molecular weight
PID	Proportional integral differential controller
PMMA	Poly methyl methacrylate
RPM	Revolutions per minute
SEM	Scanning electron microscope

h	Planck's constant
$\hbar$	$h/2\pi$
c	speed of light
e	magnitude of electron charge
Φ_S	superconducting flux quantum $hc/2e$
Φ_O	normal metal flux quantum hc/e

k_B	Boltzmann's constant
μ_B	Bohr magneton
ψ	Electron wave function
$\mathbf{k}$, $\mathbf{Q}$	Electron wave vectors
$E_{\mathbf{k}}$	Electron energy at momentum $\mathbf{k}$
ΔE	Electron energy difference
k_F	Fermi momentum
v_F	Fermi velocity
$N(0)$	Electron density of states at the Fermi surface
$\mathbf{L}$	Electron angular momentum
$\mathbf{s}$	Electron spin momentum
$\sigma_{ss'}$	Pauli spin matrix
κ	Inverse electron screening length
D	Electron diffusivity
q_p	Most probable phonon wavevector
λ_p	Most probable phonon wavelength
v_s	Velocity of sound
ω_D	Debye frequency
$\mathbf{S}$	Magnetic impurity spin
J	Exchange integral
$G(\mathbf{r},\mathbf{r}')$	Electron propagator
$C(\mathbf{Q},\omega)$	Particle-particle propagator
$D(\mathbf{q},\omega)$	Particle-hole propagator

Ψ	Digamma function
σ	Electrical conductivity
$\Delta\sigma$	Conductivity correction due to weak localisation
$\Delta\sigma_{MT}$	Conductivity correction due to Maki Thompson fluctuations
G	Conductance
g	Reduced conductance=$G/(e^2/h)$
G_{xy}	Transverse conductance
G_{xx}	Longitudinal conductance
ΔG	rms conductance fluctuation amplitude
ΔG_{ϕ}	ΔG for a phase coherent sample
$\Delta G_{hc/e}$	Amplitude of the hc/e Aharonov-Bohm oscillations
R	Resistance
ΔR	Resistance change or fluctuation
$R_{\square}$	Sheet resistance
I	Current
V	Voltage
δR	Magnetoresistance
t	Metal film thickness
W	Sample width
L	Sample length
W_p	Probe width
L_p	Probe length
θ	Angle subtended by 2D probe

S	Loop perimeter
a	Loop radius
A	Loop area
N_m	Concentration of magnetic impurities
H	Magnetic field
ΔH	Magnetic field difference
A	Magnetic vector potential
Φ	Magnetic flux
$\Delta\Phi$	Magnetic flux difference
β	Larkin parameter
d	dimension (1, 2, 3)
τ	Total scattering time
τ_ϕ	Phase coherence time
τ_{ee}	Electron-electron scattering time
τ_N	Nyquist scattering time
τ_{ep}	Electron-phonon scattering time
τ_{so}	Spin-orbit scattering time
τ_s	Paramagnetic scattering time
ℓ	Elastic scattering length
ℓ_ϕ	Electron phase coherence length
$\ell_{\phi 2D}$	ℓ_ϕ in two dimensions
ℓ_T	Thermal diffusion length

ℓ_{so}	Spin-orbit scattering length
ℓ_s	Magnetic scattering length
H_o	Characteristic field for elastic scattering
H_ϕ	Characteristic field for phase breaking
H_c	Conductance fluctuation correlation field
T	Temperature
T_K	Kondo temperature
T_c	Superconducting critical temperature
T_g	Spin glass transition temperature
F	Conductance fluctuation correlation function

List of Figures

List of Tables

ABSTRACT

Electron Quantum Interference in Small Metal Wires and Loops

Venkat Chandrasekhar

Yale University

1989

The interference of electron waves scattered off impurities in a disordered metal gives rise to quantum corrections to the classical Drude resistance. These quantum corrections have been investigated in thin film samples whose dimensions are on the order of the electron phase coherence length ℓ_ϕ, which can be a few microns at 1 K. The films were prepared by thermal evaporation onto substrates previously patterned by electron-beam lithography, and were measured using a four-point bridge technique in a perpendicular magnetic field at liquid He^4 temperatures.

Quantum interference effects in these samples are strongly influenced by the measurement probes. In experiments on short Ag wires with different probe configurations, both the shape and the magnitude of the weak localisation magnetoresistance are found to be dependent on the specific probe configuration. Similar effects are seen on conductance fluctuations in these samples. The theory of weak localisation has been extended to incorporate the effects of the measurement probes, and excellent quantitative agreement with experiment is obtained.

Measurements of single normal metal loops have been performed in search of Aharonov-Bohm magnetoresistance oscillations. Oscillations of period hc/2e and hc/e are observed in single rings of Al, Ag and Au. Quantum interference effects in these loops are also found to be strongly affected by the measurement probes. In addition,

the effect of magnetic scattering on the Aharonov-Bohm oscillations in single Ag loops has been investigated. It is found that a small amount of surface Co impurities suppresses the hc/2e oscillations, but leaves the hc/e oscillations unaffected. These results are discussed in terms of the current understanding of electron dephasing in disordered metals.

1. Introduction

Sixty years after the discovery of quantum mechanics, we are still surprised at phenomena which are essentially quantum mechanical in nature, more so when these phenomena occur in as well studied a subject as the electrical transport of normal metals. In the decade since the prediction and verification of electron localisation in normal metals [Bergmann, 1984; Lee and Ramakrishnan, 1985], the number of quantum corrections to the classical Drude theory of electron transport has grown to include, among other effects, the Aharonov-Bohm effect [Stone and Imry, 1986; Aronov and Sharvin, 1987] and conductance fluctuations [Stone, 1988; Imry, 1986]. As in other branches of physics, these quantum corrections are observable only in systems whose dimensions are comparable to some microscopic length scale. For electrons, these length scales are small, and the observation of these effects is only made possible by the recent ability to fabricate metal structures on the scale of nanometres [Howard and Prober, 1982; Rooks *et al.*, 1987]. Even with such small devices, these effects are difficult to observe. More recently, with the fabrication of high mobility semiconductor structures in which quantum length scales can be tens of micrometres [Timp *et al.*, 1987], effects on the order of the resistance of the sample have been observed, making feasible the practical application of phenomena that, just a few years ago, were of purely academic interest.

1.1 Quantum Interference

The introduction of randomly distributed impurities changes the electrical

characteristics of a metal. In the semiclassical theory of electron conduction, these impurity sites act solely as elastic scattering centres for the delocalised electrons, with no correlation between different scattering events from the same impurity, or scattering events from different impurities. In reality, however, an electron wave scattering off an impurity produces partial waves which can interfere coherently amongst themselves, and it is this interference that leads to corrections to the classically expected behaviour [Khmelnitskii, 1984]. The size of these corrections is strongly dependent on the length over which the waves can retain phase memory: The shorter this length, the smaller the interference effects.

So far, what we have said can apply to the propagation of any wave phenomenon in a disordered medium; indeed, the effects of this coherent interference have been observed in a number of different systems, ranging from light propagation in liquid suspensions of small polystyrene balls [Van Albada and Lagendijk; Wolf and Maret, 1985] to the propagation of acoustic waves in piano wire [He and Maynard, 1986]. Electron waves have particular properties that distinguish them from other waves. First, electrons carry charge, and so any correction to the classical behaviour of a metal due to interference is immediately observable in the resistance. Second, the phase of an electron is sensitive to a magnetic field [Aharonov and Bohm, 1959]: by application of an external magnetic field, one can change the phase difference between different paths in a metal. This changes the interference pattern, and therefore the resistance. The length over which the electrons retain phase memory, which we shall denote by ℓ_ϕ (and variously call the electron phase coherence length or the electron phase breaking length), is as short as a few micrometres, even at liquid helium temperatures. This is the parameter that sets the length scale for

electron interference. Therefore, in order to see electron interference effects, we need devices whose dimensions are comparable to this length.

1.2 Weak Localisation

Historically, weak localisation was the first quantum interference effect to be investigated. Thouless [1977] and Abrahams *et al.* [1979] predicted that the localisation of electrons induced by the presence of disorder would, at low temperatures, lead to an increase in the resistance of a metal over the residual resistance due to impurity scattering. Early experiments on weak localisation attempted to observe this increase in resistance. However, due to the presence of electron-electron interaction effects, which also give rise to an anomalous increase in the resistance, the results of these early experiments were not unambiguous [Giordano *et al.*, 1979; Masden and Giordano, 1982]. Later, it was recognised that the sensitivity of the weak localisation correction to external magnetic fields provided a way to separate these two contributions to the resistance. Since then, numerous experiments on thin films and wires have demonstrated unambiguously the presence of a quantum correction at low temperatures, in detailed agreement with the quantitative predictions of the microscopic theory of weak localisation [Lee and Ramakrishnan, 1985]. In fact, weak localisation has now established itself as a versatile tool to probe the dynamics of electrons in disordered metals. Experiments of thin films and long narrow wires have been used to verify predictions for electron-electron scattering rates and electron-phonon scattering rates [Santhanam *et al.*, 1987], and are now being used to investigate the Kondo effect [Bergmann, 1986, 1987; Bergmann *et al.*, 1987; Van Haesondonck *et al.*, 1987].

1.3 Conductance Fluctuations and the Aharonov-Bohm Effect

The experiments described above were carried out on macroscopic metal films and wires, samples for which at least one dimension was much longer than ℓ_ϕ. As new technology permitted the size of the devices to be reduced to lengths comparable to or less than ℓ_ϕ, in the so-called "mesoscopic" size regime, further new effects were observed.

The first experiments on such mesoscopic samples were intended to verify predictions about the Aharonov-Bohm effect, the periodic oscillation in the conductance of a loop with the magnetic flux through the loop. Aharonov-Bohm oscillations of two different periods in flux had been predicted: those of period hc/2e, and those of period hc/e. Aharonov-Bohm oscillations of period hc/2e had already been observed in metal cylinders for which the height of the cylinder was much longer than ℓ_ϕ [Sharvin and Sharvin, 1982]. However, no periodic oscillations were observed in the first experiments on metal cylinders with height much smaller than ℓ_ϕ, i.e., single loops. Instead, aperiodic fluctuations of the conductance were found [Umbach *et al.*, 1984; Skocpol *et al.*, 1984; Blonder *et al.*, 1984]. These "conduction fluctuations" are now known to be ubiquitous in mesoscopic samples, and have became a subject of interest in their own right [Washburn, 1988; Kaplan and Hartstein, 1988]. We shall discuss them in detail in this thesis.

Soon after the first observation of conductance fluctuations, Aharonov-Bohm oscillations of period hc/e and hc/2e were also observed in single metal loops. Webb *et al.* (1985) were the first to observe oscillations of period hc/e in single loops of Au. Subsequently, oscillations of both periods were observed in single loops of Al and

Au [Chandrasekhar *et al.*, 1985]; some of these experiments are described in this thesis. The Aharonov-Bohm effect is perhaps the clearest illustration of quantum interference in mesoscopic systems, and its observation clearly confirmed the physical picture of quantum interference in disordered metals.

1.4 Mesoscopic Systems

The general qualitative features of conductance fluctuations and the Aharonov-Bohm effect in mesoscopic systems have now been well confirmed by experiment. There are two problems, particular to mesoscopic systems, which make a detailed *quantitative* analysis difficult.

First- until recently, quantitative agreement between the experimentally observed data from mesoscopic samples and the available theories of weak localisation and conductance fluctuations was not at the same level as it was for weak localisation in macroscopic samples. This was because these theories did not take into account the effects of the measurement probes of the sample. In mesoscopic systems, due to the nonlocal nature of quantum interference, the measurement probes strongly affect the measurement of all quantum interference effects. Attempts to measure quantum interference phenomena at a single point measure instead a region of size ℓ_ϕ; in mesoscopic systems, this region includes the measurement probes outside the lithographically defined sample. The properties of the probes therefore show up in the measurement. Recent experiments on conductance fluctuations [Benoit *et al.*, 1987; Skocpol *et al.*, 1987] have shown that the measurement probes can have large effects on quantum interference in mesoscopic samples. In these experiments, conductance fluctuations of amplitude much larger than the predicted "universal" value of e^2/h

were seen. Similar anomalous results had been observed earlier in weak localisation in short metal wires [Masden and Giordano, 1982]. These results could not be understood quantitatively on the basis of theories of conductance fluctuations and weak localisation available at the time, which did not take into account the effect of measurement probes.

Second, for a quantitative comparison to theory, one must be able to reliably determine the electron phase coherence length ℓ_ϕ. In a normal metal, the only way to infer ℓ_ϕ is to fit the low field magnetoresistance to the standard theory of weak localisation. As mentioned above, for macroscopic samples such as thin films and long wires, this works remarkably well. For mesoscopic samples, a mesoscopic theory of weak localisation is required. Until recently, no such theory was available.

Both these problems were encountered during the early part of this thesis work, which involved a successful effort to observe Aharonov-Bohm oscillations in single loops. It was found that the macroscopic theory of weak localisation and the hc/2e Aharonov-Bohm effect did not quantitatively describe the data from these samples, and, if one insisted on fitting the data to these theories, the phase coherence lengths so inferred did not agree with previous studies on similar films. At the time these experiments were done, the effect of measurement probes on mesoscopic systems was not fully understood. Experiments on loops of different sizes, however, did show that the problems were more acute in smaller loops, and these results led us to investigate the simpler case of short wires, where similar results were found.

Sometime before, the anomalous results on conductance fluctuations mentioned above had initiated a flurry of theoretical activity (which still continues) aimed at extending the theory of conductance fluctuations to account for the effect of the

measurement probes [see Stone and Szafer, 1988, for a review]. These studies were generally successful in explaining the behaviour seen in the mesoscopic devices. For the case of weak localisation, the theory of mesoscopic systems with probes has recently been developed; some of that work forms a part of this thesis, and will be discussed in Chapter 2. This theory has been successful in explaining the data from our short wires, and provides a means of determining the phase coherence length self-consistently from magnetoresistance data mesoscopic samples.

The major part of this thesis is devoted to an attempt to develop a quantitative understanding of quantum interference in the short metal wires and loops we have measured, in light of the recent developments in the theory. We shall try to apply our knowledge of weak localisation and electron scattering mechanisms in macroscopic systems to better understand the physics of quantum interference in mesoscopic systems.

1.5 Overview of this Thesis

In the following chapter, after a brief review of the quantum field theory description of conductivity, we derive the localisation correction for a number of mesoscopic systems. A discussion of the theory of conductance fluctuations follows. We then discuss in detail the mechanisms which lead to the dephasing of electrons, with particular attention to the differences between dephasing mechanisms for weak localisation and conductance fluctuations. In Chapter 3, details of device fabrication and measurement are described. Chapter 4 deals with the experimental study of the effect of measurement probes on weak localisation and conductance fluctuations in short metal wires. Chapter 5 is concerned with the experimental results on the

Aharonov-Bohm effect in single loops. In Chapter 6, we compare our results with other work on quantum interference in mesoscopic systems and Chapter 7 contains a summary of our results and conclusions.

2. Theory

The quantum effects that are the subject of this thesis arise from the interference of electron waves scattered from randomly distributed impurities or defects. Conceptually, it is not difficult to include scattering due to random impurities in a description of the electron gas- we only need know the position of each impurity. Practically, however, it is neither possible nor desirable to know the position of each of the large number of impurities present in a typical metallic sample, and some sort of statistical description of the impurity distribution is needed. One way of doing the statistics is provided by impurity-averaged perturbation theory [Abrikosov and Gorkov, 1959], the formalism we shall use here to describe the theoretical results on quantum interference in disordered metals. A detailed description of this technique can be found in a number of textbooks, and will not be repeated here [see, for example, Abrikosov *et al.*, 1975; Rickayzen, 1980]. The description of the electrical conductivity in this technique not only provides an elegant quantum mechanical derivation of the classical Drude formula, it also predicts a number of quantum corrections [Altshuler *et al.*, 1982], the most extensively studied of these being weak localisation. However, due to the very nature of the impurity averaged formalism, calculations of the electrical conductivity are not able to predict interference effects which depend on the specific impurity arrangement in the metallic sample, effects such as conductance fluctuations and the hc/e Aharonov-Bohm effect. For sample specific effects, one needs to calculate higher moments of the conductivity [Altshuler, 1985; Lee and Stone, 1985]. One of the successes of impurity averaged

perturbation theory has been its ability to make unambiguous quantitative predictions; frequently, these predictions have preceded a full physical understanding of quantum interference phenomenona.

In this chapter, after a brief overview of the theory of electrical conductivity in the field theory formalism, we shall first discuss weak localisation in the absence of an external magnetic field and spin-dependent scattering, deriving the weak localisation correction for different sample geometries. Next, we shall briefly go over the theory of conductance fluctuations. The last part of the chapter deals with different electron scattering mechanisms. In that section, we shall first deal with electron-electron and electron-phonon scattering and their effect on quantum interference. We shall then discuss spin-dependent scattering mechanisms and their effect on weak localisation and conductance fluctuations.

2.1 Electrical conductivity

The propagation of an electron from a point $\mathbf{r}$ to a point $\mathbf{r}'$ is described by the Green's function

$$G(\mathbf{r},\mathbf{r}') = -(i/\hbar)\langle T\psi(\mathbf{r})\psi^{+}(\mathbf{r}')\rangle \qquad (2.1)$$

the diagram for which is shown in Fig. 2.1a. Here T is the time-ordering operator, and the ψ's are the field operators for the electrons [Rickayzen, 1980]. For free electrons, the electron wave function $\sim e^{i(\mathbf{k}.\mathbf{r}-E_{\mathbf{k}}t/\hbar)}$, where $\mathbf{k}$ is the momentum of the electron and $E_{\mathbf{k}}$ its energy. With the introduction of random impurities, an electron, on average, can travel for only a time τ before being scattered elastically by an impurity. This introduces a finite lifetime in the electron wavefunction, $e^{i(\mathbf{k}.\mathbf{r}-E_{\mathbf{k}}t/\hbar)-t/\tau}$. Diagrammatically, this is depicted by graphs similar to Fig. 2.1b,

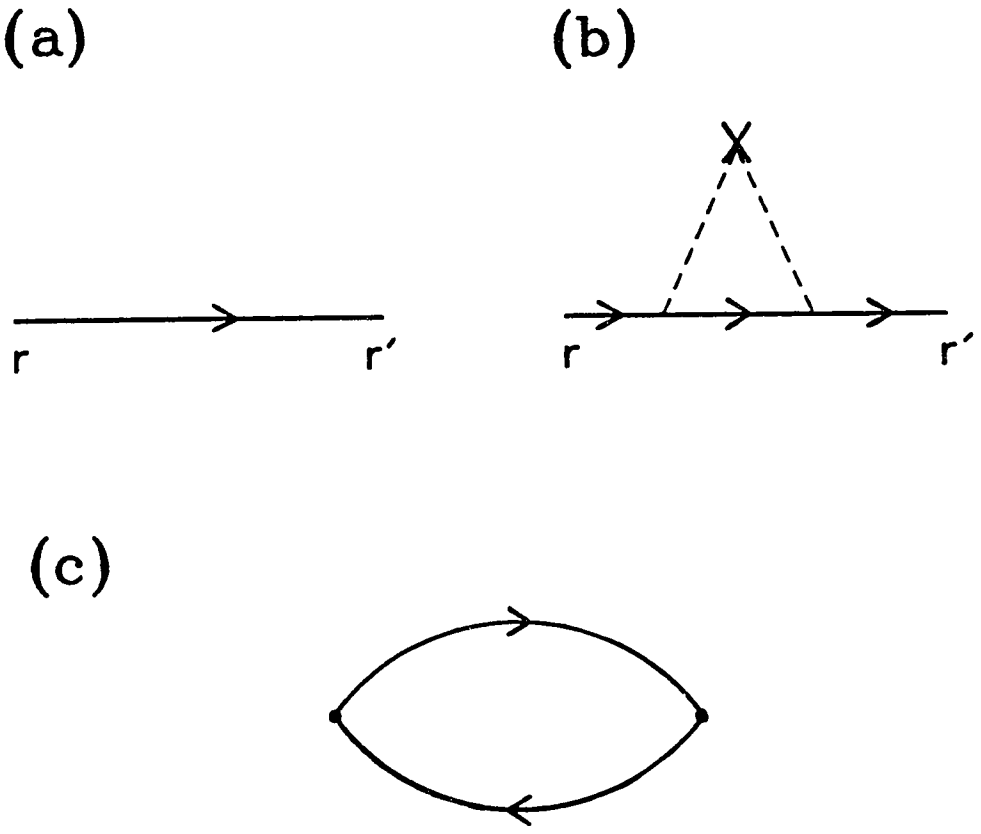

Figure 2.1 (a). Real space Green's function of a free electron. (b). Green's function of an electron in the presence of random electrostatic impurities. Dashed lines represent the impurity interaction. (c). Graph for the electrical conductivity.

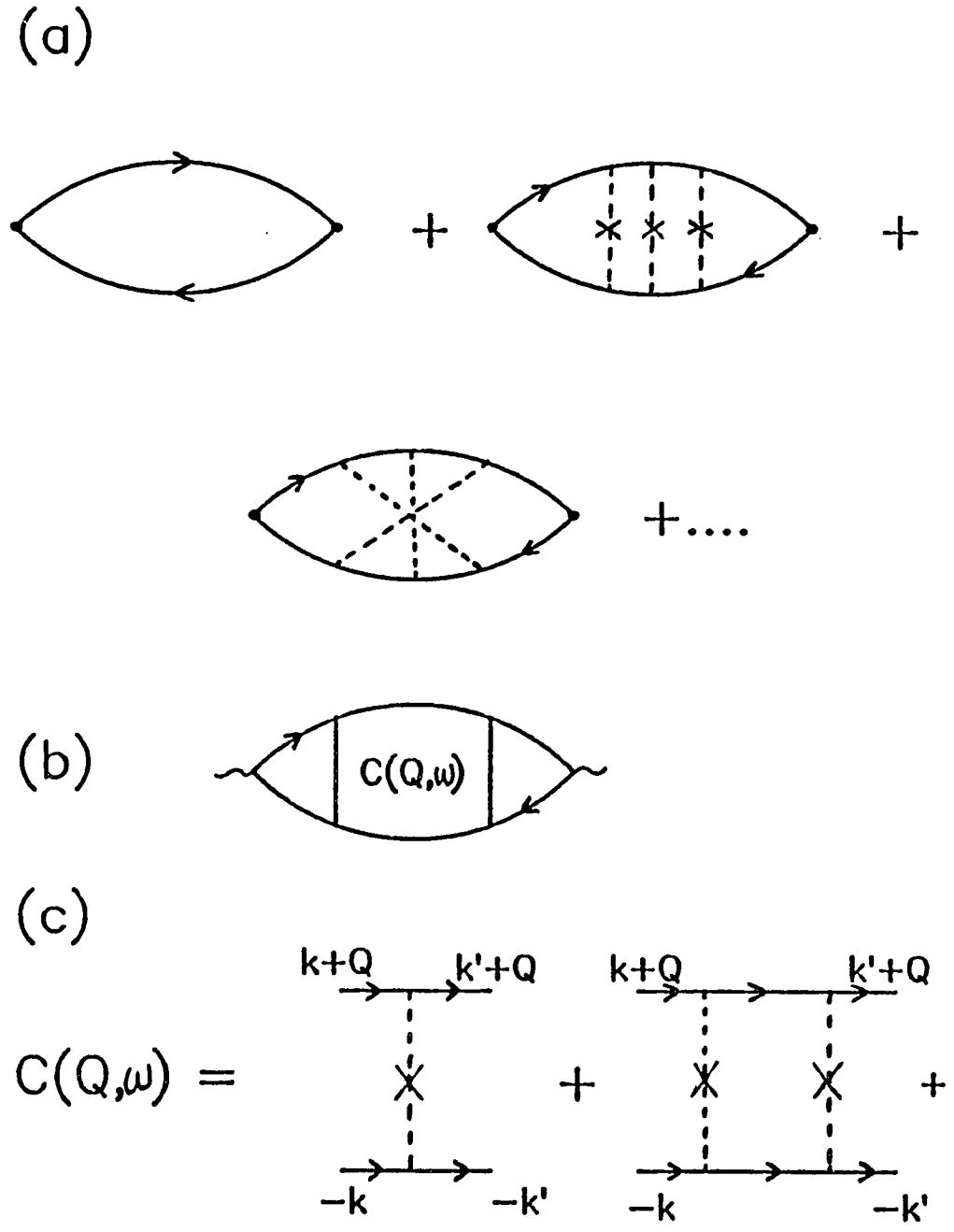

Figure 2.2 (a). The conductivity graphs with impurity scattering. (b). Momentum space representation of the maximally crossed diagrams, the weak localisation graphs. (c). The series for the Cooperon C(Q,ω), also called the particle-particle propagator.

where the dashed lines denote scattering by an impurity. In this formalism, the electrical conductivity in the absence of impurity scattering is given by the diagram in Fig. 2.1c. Impurity scattering can be introduced by drawing impurity lines (as in Fig 2.1b) in all possible ways. Examples of three different types of graphs that result from introducing impurity lines are shown in Fig. 2.2a. (In order to avoid cluttering the figure with impurity lines, each single line in Fig. 2.2a actually represents the Green's function in the presence of impurity scattering, (Fig. 2.1b)). The total conductivity is given by a sum of all such graphs. The first graph in Fig. 2.2a has no impurity lines connecting the particle and hole propagators. The second graph does have impurity lines connecting the two propagators, but these impurity lines do not cross each other. The first graph and the sum of all graphs similar to the second give the semiclassical Drude formula for the conductivity [Abrikosov *et al.*, 1959].

The third class of graphs have crossed impurity lines connecting the particle and hole propagators. These are the graphs which give the weak localisation contribution to the conductivity [Gorkov *et al.*, 1979]. Due to the crossing of the impurity lines, the contribution of this class of graphs is $1/k_F\ell$ smaller than the first two graphs, where k_F is the Fermi momentum, $\ell = v_F\tau$ the elastic mean free path and v_F the Fermi velocity. Because of this, they were ignored in the first calculations of the conductivity [Abrikosov *et al.*, 1975].

2.2 Weak Localisation: The Diffusion Equation

For actual calculations, it is more convenient to represent the diagrams in Fourier space. The sum of the third class of conductivity graphs of Fig. 2.2a in this representation is shown in Fig. 2.2b. The kernel $C(\mathbf{Q},\omega)$ is called the Cooperon, in

analogy to the superconducting case. To evaluate $C(\mathbf{Q},\omega)$, it is convenient to reverse the direction of the lower Green's function, which describes the propagation of a hole, converting it into a particle propagator. This can only be done in the absence of any interactions which break the time-reversal symmetry between the particle and hole. The result is a geometric series, the ladder graphs (Fig. 2.2c).

The series in Fig. 2.2c can be summed to give

$$C(Q,\omega) = \frac{1}{2\pi N(0)\tau} \frac{1}{DQ^2\tau - i\omega\tau}, \qquad (2.2)$$

where $D = (1/3)v_F\ell$ is the diffusion constant and $N(0)$ the electron density of states at the Fermi energy. The correction to the conductivity $\Delta\sigma$ is obtained by summing over all values of $\mathbf{Q}$,

$$\Delta\sigma(\omega) = -\frac{2e^2D}{\pi} 2\pi N(0)\tau^2 \sum_Q C(Q,\omega) = -\frac{2e^2D}{\pi} \sum_Q \frac{1}{DQ^2 - i\omega}. \qquad (2.3)$$

We shall define the sum in the last expression as $C(\mathbf{r},\mathbf{r};t,t)$ where $C(\mathbf{r},\mathbf{r}';t,t')$ is the solution of the equation

$$\left(\frac{\partial}{\partial t} - D\nabla^2\right) C(\mathbf{r},\mathbf{r}';t,t') = \delta(\mathbf{r}-\mathbf{r}')\delta(t-t'). \qquad (2.4)$$

By expressing the delta functions in terms of the free electron eigenfunctions of the problem, $e^{i(\mathbf{Q}.\mathbf{r}-\omega t)}$, one can get an eigenfunction expansion for C. Then, by setting $\mathbf{r}'=\mathbf{r}$ and $t'=t$, one obtains the sum in Eq. (2.3). $C(\mathbf{r},\mathbf{r}')$ is the probability that an electron at $\mathbf{r}$ will diffuse to $\mathbf{r}'$; $C(\mathbf{r},\mathbf{r})$ is the probability that it will return to the origin, and is therefore a measure of the probability that it will remain localised at $\mathbf{r}$.

Before we go any further, we need to include the effects of an external magnetic field and electron phase breaking. The effect of an external magnetic field $\mathbf{H}$ on an electron is to transform the momentum $\mathbf{k}$ of the electron to $\mathbf{k}$-eA/c, where

the magnetic vector potential **A** is related to the magnetic field **H** by **H**=curl**A**. The vector **Q** in Eq. (2.3), which is the sum of two such momenta, changes to **Q**-2e**A**/c, and $-\nabla^2$ in Eq. (2.4) correspondingly changes to $(-i\nabla-2eA/c)^2$. To take into account the effects of electron-phonon and electron-electron scattering, one also introduces phenomenologically a rate τ_ϕ^{-1} into the denominator of the sum in Eq. (2.3), which now becomes $DQ^2-i\omega+\tau_\phi^{-1}$ [Altshuler *et al.*, 1980]. τ_ϕ is related to the electron phase breaking length ℓ_ϕ, introduced in the previous chapter, by the equation $\ell_\phi^2=D\tau_\phi$. Finally, since we are interested in the static conductivity, we set $\omega=0$. Putting all this together, and remembering our $\hbar$'s, we obtain the weak localisation correction to the conductivity

$$\Delta\sigma = -\frac{2e^2D}{\pi V}\int C(\mathbf{r},\mathbf{r})d^3\mathbf{r}, \qquad (2.5)$$

where $C(\mathbf{r},\mathbf{r}')$ is the solution of the diffusion equation

$$[(-i\nabla - (2eA/\hbar c))^2 + \ell_\phi^{-2}]\, C(\mathbf{r},\mathbf{r}') = \delta(\mathbf{r}-\mathbf{r}')/\hbar D. \qquad (2.6)$$

Note that $\Delta\sigma$ as defined above is essentially an average of $C(\mathbf{r},\mathbf{r}')$ over the volume V of the sample [Altshuler *et al.*, 1984].

With these two formulae, we have, at least conceptually, a simple recipe to determine the weak localisation correction for any metal sample: Solve Eq. (2.6) with boundary conditions appropriate to the sample geometry and put the result into Eq. (2.5). In practice, the solution of Eq. (2.6) for arbitrary sample geometry is not trivial, and can be found analytically only for a few simple cases. One thing to note is that, in the absence of a magnetic field, ℓ_ϕ is the only length scale in Eq. (2.6), and is therefore the length that determines the dimensionality of the localisation problem. We shall see this explicitly in the next section, where we shall derive the localisation correction for one-dimensional (1D) systems, i.e., metal wires whose

thickness t and width W are much smaller than ℓ_ϕ.

2.3 Weak Localisation in One Dimensional Systems

2.3.1 One Dimensional Systems Without Probes: Long Wire and Single Loop

To illustrate the method, consider the weak localisation correction for the simplest 1D case- a long narrow wire of length L ($>>\ell_\phi$), width W and thickness t, in a perpendicular magnetic field [Altshuler and Aronov, 1981]. The geometry is defined in Fig 2.3. The magnetic field points towards the positive z axis, $\mathbf{H}=H\,\hat{z}$. We choose the gauge $\mathbf{A}=Hx\,\hat{y}$. The boundary condition on an insulating boundary is given by

$$[\ -i\nabla_n - (2eA_n/\hbar c)\ ]\ C(\mathbf{r},\mathbf{r}') = 0, \tag{2.7}$$

where ∇_n and A_n are the components of the appropriate vectors normal to the surface. Physically, this is just the condition that at an insulating boundary, there can be no current normal to the surface. We impose the additional boundary condition that $C(\mathbf{r},\mathbf{r}')=0$ at the ends of the wire which are connected to the current and voltage contacts. Putting $\mathbf{A}$ into Eq. (2.6), we obtain

$$\left[-\nabla^2 + 2i\,\frac{2eHx}{\hbar c}\,\frac{\partial}{\partial y} + \left[\frac{2eHx}{\hbar c}\right]^2 + \frac{1}{\ell_\phi^2}\right] C(\mathbf{r},\mathbf{r}') = \frac{\delta(\mathbf{r}-\mathbf{r}')}{\hbar D}. \tag{2.8}$$

The second and third terms in the LHS in the equation above are treated as perturbations. The eigenfunctions of this equation in the absence of these perturbations which satisfy the boundary conditions are

$$\psi(x,y,z) = (8/LWt)^{1/2}\cos(Q_x x)\cos(Q_y y)\cos(Q_z z), \tag{2.9}$$

where the $\mathbf{Q}$ vectors are quantised by the boundary conditions into

$$Q_x = (2\pi m/W),\ Q_y = (2\pi n/L),\ Q_z = (2\pi p/t), \tag{2.10}$$

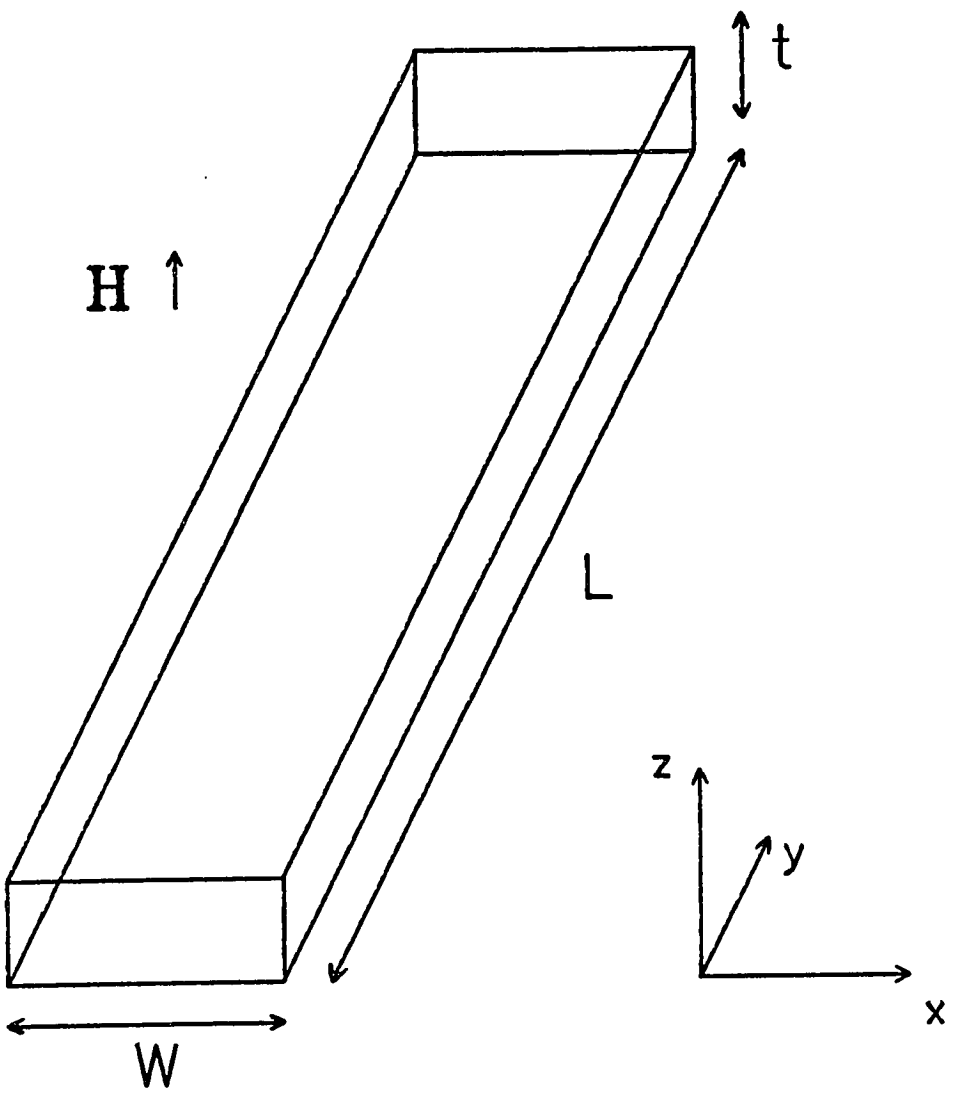

Figure 2.3. Geometry for the calculation of the localisation correction for a long wire.

and m, n and p can take on the values 0, ±1, ±2,... The perturbations are calculated to first order. This means that our results will only be valid at small magnetic fields [Santhanam, 1985]. The second term in Eq. (2.8) gives zero since it is odd in x and the eigenfunctions are even in x. The first order contribution from the third term is combined with ℓ_ϕ to give a field dependent ℓ_ϕ defined by

$$\ell_\phi(H)^{-2} = \ell_\phi^{-2} + (1/3)(WeH/\hbar c)^2. \qquad (2.11)$$

After integrating over the volume, the localisation correction can then be written as

$$\Delta\sigma = -\frac{2e^2}{\pi\hbar}\frac{1}{LWt}\sum_{Q_i}\frac{1}{Q_x^2 + Q_y^2 + Q_z^2 + \ell_\phi(H)^{-2}} \cdot \qquad (2.12)$$

If W and t are much smaller than $\ell_\phi(H)$, we need take only the m=0 and p=0 contributions in the sum over Q_x and Q_z. What is left is a 1D sum over Q_y. Thus, ℓ_ϕ determines the dimensionality of the contribution. If $L >> \ell_\phi$, we can convert the sum to an integral and obtain

$$\Delta\sigma(H) = -\frac{e^2}{\pi^2\hbar}\frac{1}{Wt}\int_{-\infty}^{\infty}\frac{dQ_y}{Q_y^2 + \ell_\phi^{-2}} = -\frac{e^2}{\pi\hbar}\frac{\ell_\phi(H)}{Wt} \cdot \qquad (2.13)$$

This is usually written in terms of the fractional change in resistance $(\Delta R/R) = -(\Delta\sigma/\sigma)$

$$\frac{\Delta R(H)}{R} = \frac{R_\square}{(\pi\hbar/e^2)}\frac{\ell_\phi(H)}{W} \cdot \qquad (2.14)$$

$R_\square = (1/\sigma t)$ is the sheet resistance of the wire and $(\pi\hbar/e^2) = 12.9$ kΩ is a fundamental unit of resistance. Putting in some typical parameters, $R_\square = 1$ Ω, $\ell_\phi = 1$ μm and W = 0.1 μm, gives $\Delta R/R \sim 8 \times 10^{-4}$. This, as noted before, is a small correction.

If we take the two ends of our wire and put them together, we form a loop. The weak localisation contribution for this case was first derived by Altshuler, Aronov, and Spivak (AAS) [1981]. They obtained

$$\frac{\Delta R(H)}{R} = -\frac{R_\square}{(\pi\hbar/e^2)}\,\frac{\ell_\phi(H)}{W}\,\frac{\mathrm{sh}[S/\ell_\phi(H)]}{\mathrm{ch}[S/\ell_\phi(H)] - \cos(2\pi\Phi/\Phi_S)}\,, \qquad (2.15)$$

where S is the perimeter of the loop, Φ is the magnetic flux through the area of the loop, Φ_S = hc/2e is the superconducting flux quantum, and sh and ch are the hyberbolic sine and cosine functions respectively. The resistance of the loop oscillates with the applied magnetic flux with a period Φ_S: this is the Aharonov-Bohm effect of period hc/2e, which is essentially a weak localisation effect. We shall refer to this as the AAS hc/2e Aharonov-Bohm effect, to distinguish it from the conductance fluctuation effect to be discussed later. In the limit of large S, the oscillations are suppressed and we regain the long wire result, Eq. (2.14).

2.3.2 One Dimensional Systems with Probes

In one important respect the two examples that we have looked at so far are idealised systems: Both the long wire and the single loop have no measurement probes attached to them. Experimentally, contact must be made to the rest of the world by means of current and voltage probes, which are usually made of the same metal as the sample itself, so it is not unexpected that the probes should affect the measurement. When the dimensions of the sample are much greater than ℓ_ϕ, the probes, as we shall see, have little effect on the measurement, and thus Eq. (2.14) describes well the localisation correction for a *long* wire. For the loop, whose perimeter S must be comparable to ℓ_ϕ in order to see the Aharonov-Bohm effect, Eq. (2.15) does not adequately describe the experimental results, and we must include the effects of the measurement probes.

To do this, we follow the approach of Doucot and Rammal [1985, 1986], who

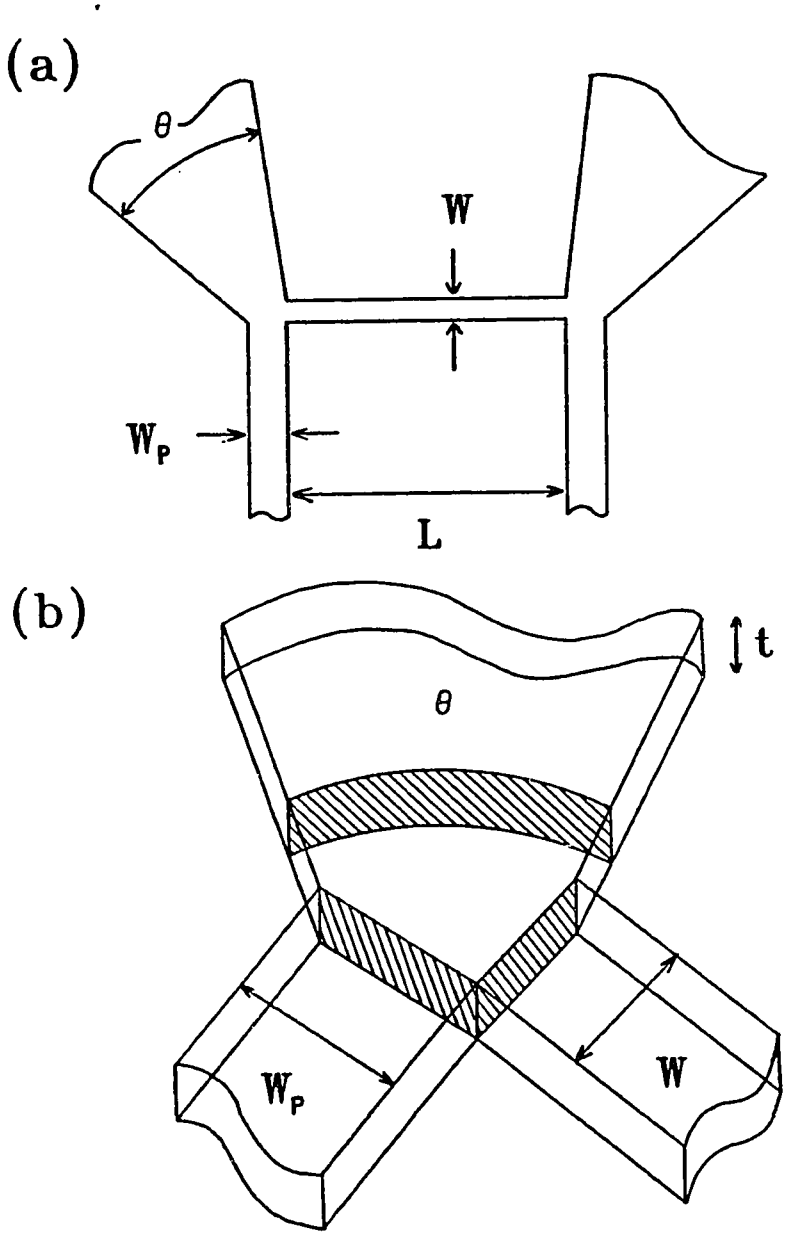

Figure 2.4. (a). Geometry for the calculation of the weak localisation correction for a 1D wire with probes. (b). Blowup of one end of the wire, showing the juncture of the wire, the 1D probe and the 2D probe.

derived the localisation correction for a network of 1D wires. We are interested in a short 1D wire of length L and width W which has two measurement probes made from the same material on each end. The geometry of the wire is shown in Fig. 2.4. One of these probes is a one dimensional wire of width W_p and the other is a 2D film which subtends an angle θ at the end of the wire. Both the probes are assumed to extend to infinity. Within the wire and the 1D probe, the diffusion equation is one dimensional. We shall initially work in zero magnetic field, generalising the result later to finite field.

Instead of expanding $C(\mathbf{r},\mathbf{r}')$ in terms of the eigenfunctions of the differential operator as we did for the long wire, we solve Eq. (2.6) for $C(\mathbf{r},\mathbf{r}')$ directly. For the 1D wire, $C(\mathbf{r},\mathbf{r}')$ in the wire depends only on the coordinates x and x' along the wire [$C(\mathbf{r},\mathbf{r}')\sim C(x,x')$], so we shall drop the remaining coordinates in the following discussion. Let C_a be the value of C(x,x') at one end of the short wire (x=0), C_b the value at the other end (x=L), and C_o the value at the point x', which is somewhere in the middle of the wire. Between x=0 and x=x', C(x,x') obeys the homogenous 1D equation

$$\left[-\frac{d^2}{dx^2} + \frac{1}{\ell_\phi^2} \right] C(x,x') = 0 \ , \qquad (2.16)$$

with the boundary conditions that $C(x,x')=C_a$ at x=0 and $C(x,x')=C_o$ at x=x'. The solution of this equation is [Doucot and Rammal, 1986]

$$C(x,x') = C_a ch(x/\ell_\phi) + [C_o - C_a ch(x'/\ell_\phi)] \frac{sh(x/\ell_\phi)}{sh(x'/\ell_\phi)} \ . \qquad (2.17)$$

A similar solution can be found for the strand between x=x' and x=L and for the two 1D probes on either end of the wire. For the 1D probes, however, since the length of the probes is infinite, the boundary condition at the end of the probe farthest

from the wire is irrelevant. This can be seen by setting $x' \to \infty$ in Eq. (2.17), whereupon the term containing C_0 (the value of C(x,x') at the end of the probe farthest from the wire) vanishes.

Eq. (2.17) gives C(x,x') in terms of C_a and C_b, which are still unknown and must be determined by the boundary conditions at x=0 and x=L. The appropriate boundary condition can be determined by integrating the diffusion equation over a very small volume v around the point **r**

$$\int_v (-\nabla.\nabla + \ell_\phi^{-2})\ C(\mathbf{r},\mathbf{r}')\ d^3\mathbf{r} = \int \frac{\delta(\mathbf{r}-\mathbf{r}')}{\hbar D}\ d^3\mathbf{r}. \qquad (2.18)$$

The first term under the integral sign can be converted by the divergence theorem into a surface integral. The second term can be neglected if the volume of integration v is small in comparison to $\ell_\phi^2 t$ (t is the thickness of the film). For a short wire of width W, with one 2D probe and one 1D probe (of width W_p) on each end, the maximum volume of the integration region is $W_p W t$. Thus, when W and $W_p << \ell_\phi$, the second term can be neglected. The term on the RHS is zero if the region of integration does not contain **r'**, and unity if it does. Eq. (2.18) then becomes

$$-\int_s \nabla C(\mathbf{r},\mathbf{r}')\ d^2\mathbf{r} = \frac{\delta_{\mathbf{r},\mathbf{r}'}}{\hbar D}\ . \qquad (2.19)$$

where the surface s encloses the volume v. Since the boundary condition Eq. (2.7) still holds for the component of the gradient perpendicular to the surface of the metal, the only contribution to the integral in Eq. (2.19) is from the component within the plane for the 2D film, and along the 1D strands for the wires.

Let us now apply Eq. (2.19) at the point x=0, the juncture of the wire, the 1D pad and the 2D film. The surface of integration is shown in Fig. 2.4b. The only

contribution to the integral comes from the three regions of the surface which are shaded in Fig. 2.4b. The first is in the 2D film, and is part of the surface of a right circular cylinder of radius r and height t. Over this surface, the gradient of C(r,r') is constant and has the value $-(C_a/r)/[\ln(2\ell_{\phi 2D}/\ell)]$ [Appendix I], where $\ell_{\phi 2D}$ is the phase breaking length in the 2D film, which can be different from ℓ_ϕ in the 1D wire [Santhanam *et al.*, 1987], and ℓ is the elastic mean free path. Integrating over this region of the surface then gives $-\theta t C_a/[\ln(2\ell_{\phi 2D}/\ell)]$. The value of $\nabla C(\mathbf{r},\mathbf{r}')$ over the two other regions in the 1D strands can be calculated from Eq. (2.17). As before, $\nabla C(\mathbf{r},\mathbf{r}')$ is constant over each of the two regions, and the surface integral just gives the surface areas of each region, which are Wt and $W_p t$ for the wire and the probe respectively. Noting that the RHS of Eq. (2.19) is zero for the particular volume of integration (since it does not contain $\mathbf{r}'$), we obtain, after a bit of algebra,

$$-C_a(\eta_1 + \eta_2) + \alpha \left[\frac{C_o}{sh(x')} - C_a\, cth(x') \right] = 0, \qquad (2.20a)$$

where $\eta_1 = \theta/[\ln(2\ell_{\phi 2D}/\ell)]$, $\eta_2 = W_p/\ell_\phi$, $\alpha = W/\ell_\phi$ and, to save space, the arguments of the hyperbolic functions are written with respect to ℓ_ϕ. This equation is the equivalent of the network equations of Doucot and Rammal [1986], generalised to take into account 2D components and 1D strands of different widths. Following Doucot and Rammal, we call the small volume of integration a "node." Two other equations are obtained from the nodes at x=x' and x=L

$$C_o[cth(x') + cth(L-x')] - \frac{C_a}{sh(x')} - \frac{C_b}{sh(L-x')} = \frac{\ell_\phi}{\hbar D t W}, \qquad (2.20b)$$

and

$$-C_b(\eta_1 + \eta_2) + \alpha \left[\frac{C_o}{sh(L-x')} - C_b\, cth(L-x') \right] = 0. \qquad (2.20c)$$

Eqs. (2.20) are three equations which can be solved for the three unknowns C_a, C_o and C_b. Once we know C_a, C_o and C_b, we can determine C(x,x') anywhere in the wire, using Eq. (2.17). In general, one can write such network equations for geometries with any number of nodes. For N nodes (including the source node at x'), we need to solve N linear equations in N unknowns. In complicated geometries, this may not be possible to do in closed form.

For weak localisation we require C(x,x). This is just the value of C(x,x') at x=x', i.e., C_o. Thus, we only need to solve the three linear equations (2.20) for C_o and put this into Eq. (2.5). After much algebra, one obtains for $C(x)=C(x,x)=C_o$

$$C(x) = \frac{1}{2}\frac{\ell_\phi}{\hbar DtW}\frac{\{[\eta^2+\alpha^2] - [\eta^2-\alpha^2][\mathrm{ch}(L-2x)/\mathrm{ch}(L)] + 2\alpha\eta\,\mathrm{th}(L)\}}{\{[\eta^2+\alpha^2]\,\mathrm{th}(L) + 2\alpha\eta\}}, \quad (2.21)$$

where $\eta=\eta_1+\eta_2$. The final result for the fractional change in resistance is [Chandrasekhar *et al.*, 1988]

$$\frac{\Delta R}{R} = \frac{R_\square}{(\pi\hbar/e^2)}\frac{\ell_\phi}{W}\frac{[(\eta^2+\alpha^2)\,\mathrm{cth}(L) - (\ell_\phi/L)(\eta^2-\alpha^2) + 2\alpha\eta]}{[\eta^2 + \alpha^2 + 2\alpha\eta\,\mathrm{cth}(L)]}. \quad (2.22)$$

2.3.3 Short Wires: Specific Examples

From the integral in Eq. (2.5), the change in resistance of the wire due to localisation depends only on the average value of C(x) over the sample. We can gain some insight into the effect of the measurement probes on weak localisation by examining the behaviour of C(x) as a function of x in the wire. Figure 2.5 shows a plot of C(x) from Eq. (2.21) in units of $(1/2\hbar Dt)$ as a function of (x/L) for a number of different values of L/ℓ_ϕ. For $L>>\ell_\phi$, C(x) is essentially the long wire value $1/\alpha$

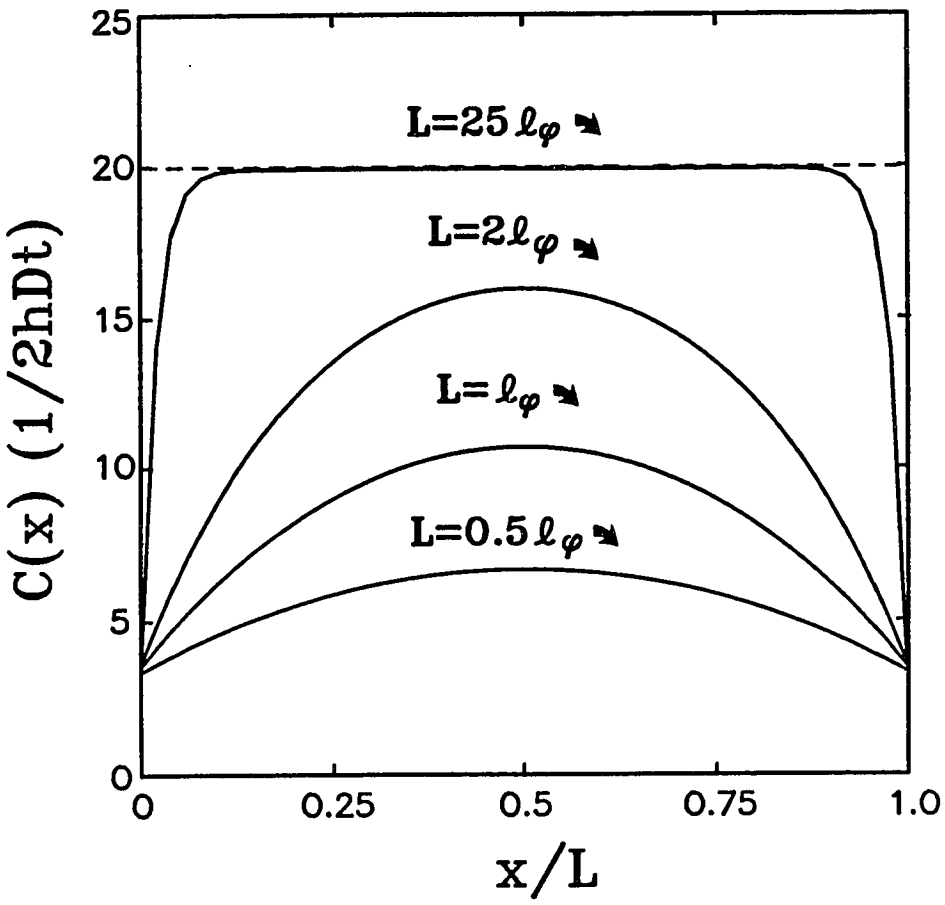

Figure 2.5. Plot of C(x) (Eq. (2.21)) in units of $(1/2\hbar Dt)$ as a function of (x/L) for different values of L/ℓ_ϕ. $\eta=0.5$ and $\alpha=0.05$ for all curves. Dotted line is the value of C(x) for a long wire.

through most of the wire. The probes only affect C(x) at distances ℓ_ϕ into the long wire, a small fraction of its total length. For shorter wires, where $\ell_\phi \sim L$, the amplitude of C(x) is reduced throughout the length of the wire, because each point in the wire is no more than ℓ_ϕ away from one of the probes.

The curves in Fig. 2.5 are all for $\eta=0.5$ and $\alpha=0.05$. The parameter η is a measure of the "leakage" of the Cooperon into the probes, and a specific value of η corresponds to a specific configuration of the measurement probes. For $\eta=0$, there is no leakage into the probes, and for $\eta=\infty$, all the Cooperon "current" which finds its way into the probes is lost. As η increases, the amplitude of C(x) in the wire itself decreases, reducing the value of $\Delta R/R$.

To see this graphically, let us take a closer look at three specific measurement probe configurations with different values of η. The first configuration is shown in Fig. 2.6a. This is similar to Fig. 2.4a, with $\theta=\pi/2$. For definitiveness, we shall take $L/\ell_\phi=1$, $\alpha=0.02$, $\eta_1=0.23$, $\eta_2=0.08$, so that $\eta=0.31$. The second configuration (Fig. 2.6b) is similar to the first, except that there are no 1D probes and each 2D probe extends over a half plane. For this configuration, $\theta=\pi$, so $\eta_1=0.46$. Since there are no 1D probes, $\eta_2=0$, and the sum $\eta=0.8$. All other parameters remain the same. The last configuration is shown in Fig. 2.6c. Here, the 2D probes of Fig. 2.4a have been replaced by 1D probes; the width of these 1D probes is the same as that of the wire, so that $\eta_1=\eta_2=\alpha$ and $\eta=2\alpha=0.04$.

Figure 2.7 shows a plot of C(x) as a function of x for all three configurations, for the parameters given above. As expected, the configuration of Fig. 2.6b results in the smallest amplitude of C(x), and the standard four-terminal configuration (Fig. 2.6c) the largest. Qualitatively, the amplitude of C(x) in the wire is inversely proportional

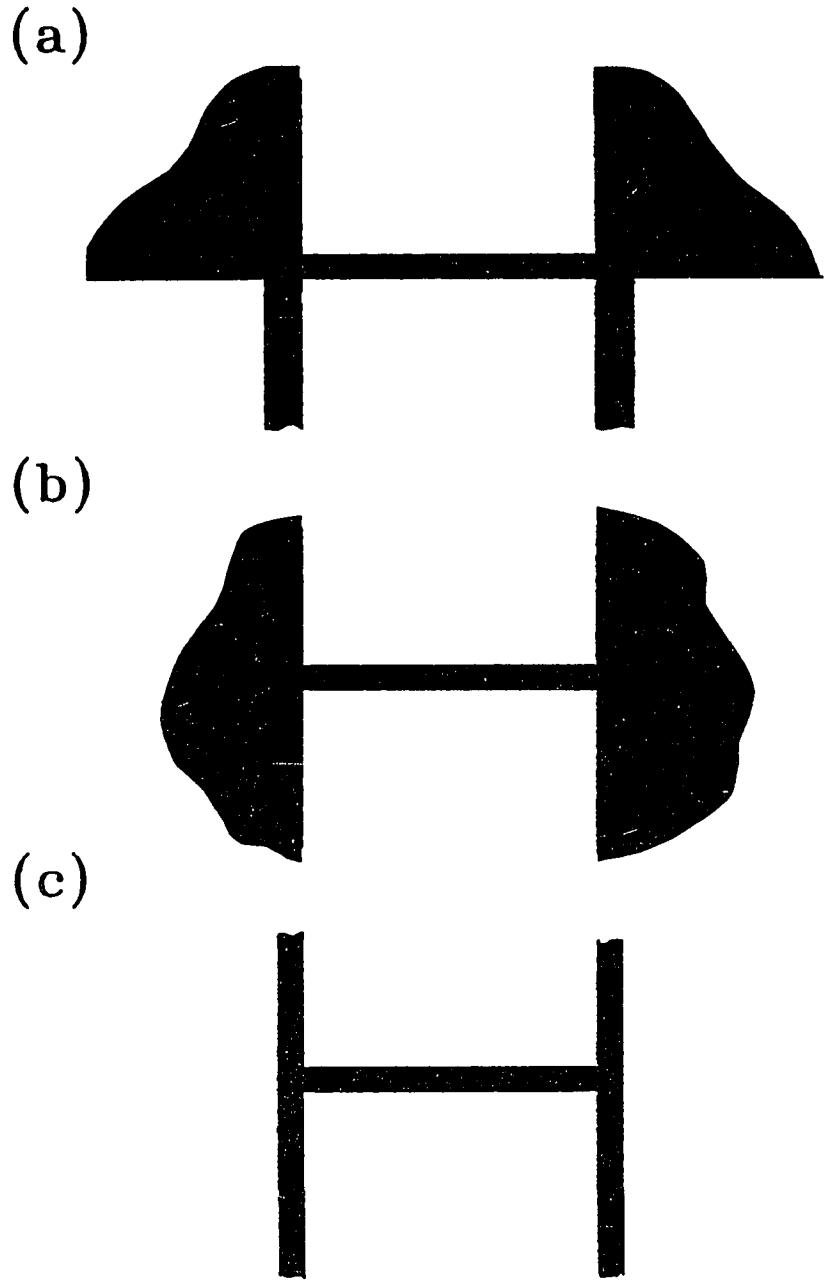

Figure 2.6. Short wire measurement probe configurations. (a). Four probe configuration, with two 2D probes and two 1D probes. (b). Quasi two terminal configuration, with two 2D probes. (c). Standard four terminal configuration, with four 1D probes.

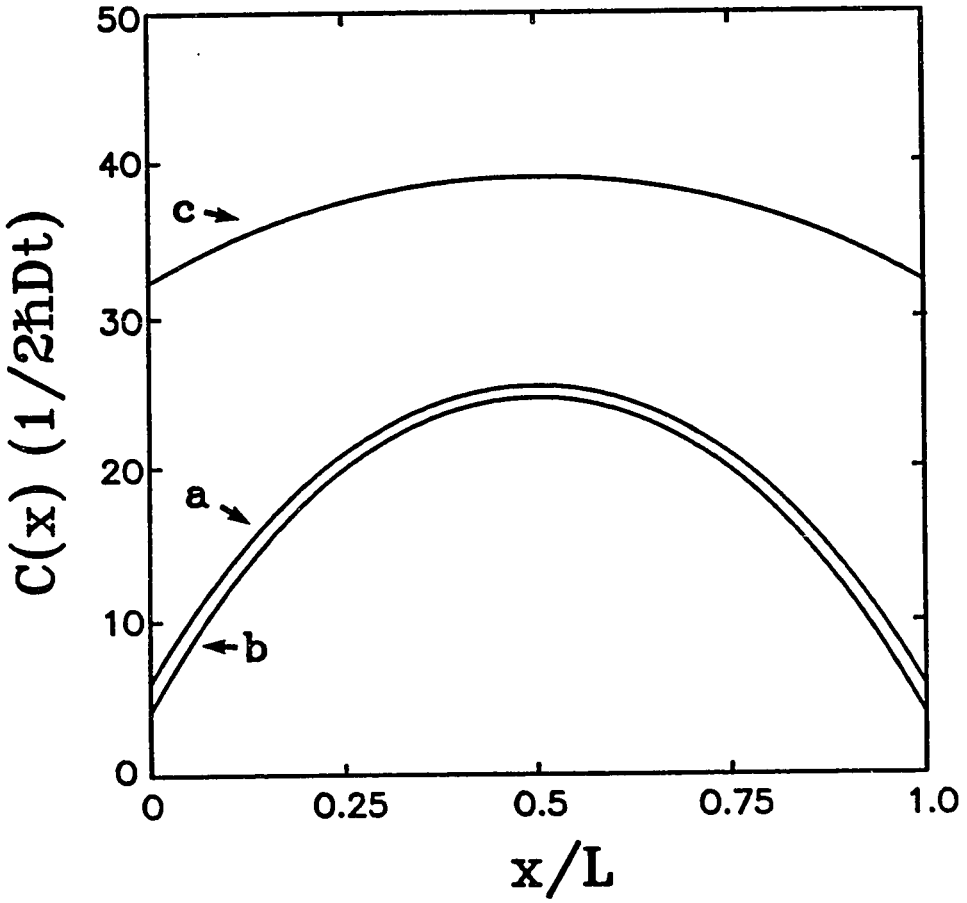

Figure 2.7. Plot of C(x) vs x/L for short wires with the three different configurations shown in Fig. 2.6, $\alpha=0.02$. Small letters (a, b, c) correspond to the configurations of Fig. 2.6. (a) $\eta=0.31$, (b) $\eta=0.46$, and (c) $\eta=0.04$. $L/\ell_\phi=1$ for all cases.

to the number (and volume) of the probes attached to it, because diffusion into the probes reduces the amplitude of $C(\mathbf{r},\mathbf{r}')$. The parameter η is a measure of this diffusion.

This relationship between the number of probes and the amplitude of C(x) is best seen by means of an example. Consider the localisation correction for the configuration of Fig. 2.6c. Setting $\eta_1=\eta_2=\alpha$ in Eq. (2.21), we obtain

$$C(x) = -\frac{1}{2}\frac{\ell_\phi}{\hbar DtW}\frac{[5 - 3[ch(L-2x)/ch(L)] + 4th(L)]}{[5th(L) + 4]}, \qquad (2.23)$$

giving for $\Delta R/R$

$$\frac{\Delta R}{R} = \frac{R_\square}{(\pi\hbar/e^2)}\frac{\ell_\phi}{W}\frac{[5cth(L) - 3(\ell_\phi/L) + 4]}{[5 + 4cth(L)]}. \qquad (2.24)$$

These two equations, in slightly different form, were first derived by Santhanam [1987] using the network formalism of Doucot and Rammal [1986]. Now consider the short wire limit ($L<<\ell_\phi$) of Eq. (2.24). In this limit, Eq. (2.24) reduces to exactly half the long wire result, Eq. (2.14). This factor of two reduction can be understood as follows. The amplitude of C(x) at a point x is determined by the number of paths within a distance ℓ_ϕ into which diffusion can occur. For the long wire, most of the points in the wire are more than ℓ_ϕ away from the probes, and therefore have, in essence, only two wires into which diffusion can occur. At each point in the short wire, however, diffusion can occur into the four measurement probes. Effectively, the value of η for the short wire is twice that for the long wire, leading to a factor of two reduction in $\Delta R/R$.

Not only does the parameter η determine the magnitude of the weak localisation correction, it also determines the shape of the weak localisation magnetoresistance

(MR), defined as

$$\frac{\delta R}{R}(T,H) = \left[\frac{\Delta R}{R}(T,H) - \frac{\Delta R}{R}(T,0) \right] , \qquad (2.25)$$

at a particular temperature T. This is because η is not a constant, but a function of the magnetic field H. For different probe configurations, η will have a different functional dependence on H, which will show up in the MR. This enables one to distinguish *experimentally* between the magnetoresistance of wires with different probe configurations.

To determine η(H), we need to include the magnetic field in our analysis. For the 1D probes and wire, this means replacing ℓ_ϕ by ℓ_ϕ(H), where ℓ_ϕ(H) is given by Eq. (2.11). The parameter η_2 in Eqs. (2.21) and (2.22) is now field dependent, $\eta_2(H) = W_p/\ell_\phi(H)$. For the 2D probes, the field dependence of the parameter η_1 is given by [Appendix I]

$$\eta_1 = -2\theta/[\ln(H/4H_o) + \Psi(1/2 + H_\phi/H)] , \qquad (2.26)$$

where Ψ is the digamma function, $H_o = \hbar c/4e\ell^2$ and $H_\phi = \hbar c/4e\ell_{\phi 2D}{}^2$.

To see how the probe configuration can actually show up in the MR, let us take, as a specific example, the configuration of Fig. 2.6b. With $\theta = \pi$, in the limit $L \to 0$, Eq. (2.22) becomes

$$\frac{\Delta R}{R} = \frac{R_\square}{(\pi\hbar/e^2)} \frac{1}{\eta} = - \frac{R_\square}{(2\pi^2\hbar/e^2)} [\Psi(1/2 + H_\phi/H) + \ln(H/4H_o)] . \qquad (2.27)$$

This is identical to the weak localisation MR of a 2D film. Even though we are measuring a 1D wire, the MR is characteristic of the 2D pads. Note that in this formula, there is no reference to the parameters of the wire itself, only to the probes through the parameter η. For a wire with only 1D probes, $(\Delta R/R) \propto (1/\eta) = [\ell_\phi(H)/2W_p]$,

giving the long wire result Eq. (2.14), but with the $\ell_\phi(H)$ and W_p of the probes. Thus the nature of the probes can be seen directly in the MR of the short wire.

2D probes have the most visible effect on the MR of a short wire: Because of the large value of η, the magnitude of the MR is greatly reduced, and the characteristic magnetic field dependence of the 2D probes contrasts with the MR signature of the 1D wire. 1D probes also affect the magnitude and the shape of the MR, but the effects are more subtle. First, the reduction in the amplitude of the MR is not as great as for the 2D probes. Second, as the signature of the probes is now also 1D, it is not as easy to see the effects of the probes in the shape of the MR. The effect of the probes on the shape of the MR is greatest when they are of a different width than the 1D wire, since then, from Eq. (2.11), $\ell_\phi(H)$ is different for the probes and the 1D wire. Nonetheless, ignoring the effects of even narrow 1D probes can lead to errors in the quantitative analysis of the MR data of short wires.

The presence of measurement probes also affect other quantum interference effects. Santhanam [1988], using the network formalism of Doucot and Rammal, has calculated numerically the effect of narrow 1D probes on the AAS Aharonov-Bohm effect, and finds that the presence of the probes reduces the amplitude of the hc/2e MR oscillations. In the next section, we shall find that the presence of measurement probes has a similar effect on conductance fluctuations.

2.4 Conductance Fluctuations

2.4.1 Conductance Fluctuations in 1D Systems

The weak localisation MR of a mesoscopic sample is frequently swamped by a much larger contribution to the MR which, unlike weak localisation, has no particular

functional dependence on the magnetic field, and is present even at very high magnetic fields [Umbach *et al.*, 1984]. Although this contribution is random in magnetic field and thus appears like noise, it is found to be quite reproducible. Such reproducible random fluctuations are also found as a function of other system parameters; for example, as a function of the gate voltage in a silicon metal oxide semiconductor field effect transistor (MOSFET). In terms of the conductance, these random fluctuations are characterised by an rms amplitude of order e^2/h, and their origin lies in the phase coherent scattering of electrons from the random arrangement of impurities in the mesoscopic sample.

The classical conductivity and the weak localisation correction calculated above are averages over an ensemble of many samples with different impurity configurations. The conductivity of any one sample will actually be a random function of a number of parameters, and will most probably deviate from the impurity-averaged properties calculated above. A measure of this deviation is given by the variance [Altshuler, 1985]

$$\delta\sigma^2 = \langle\sigma^2\rangle - \langle\sigma\rangle^2 \qquad (2.28)$$

where the brackets denote averaging with respect to the impurity configuration. This quantity is given by diagrams in which two conductivity loops are connected by impurity lines. Some of these diagrams are shown in Fig. 2.8.

Experimentally, one does not perform the average in Eq. (2.28) over an ensemble of samples with different impurity configurations, but over some external parameter in a single sample. Typically, this external parameter is the magnetic field. According to the so called ergodic hypothesis [Lee and Stone, 1985], averaging over a large magnetic field range is equivalent to averaging over impurity configurations. Since

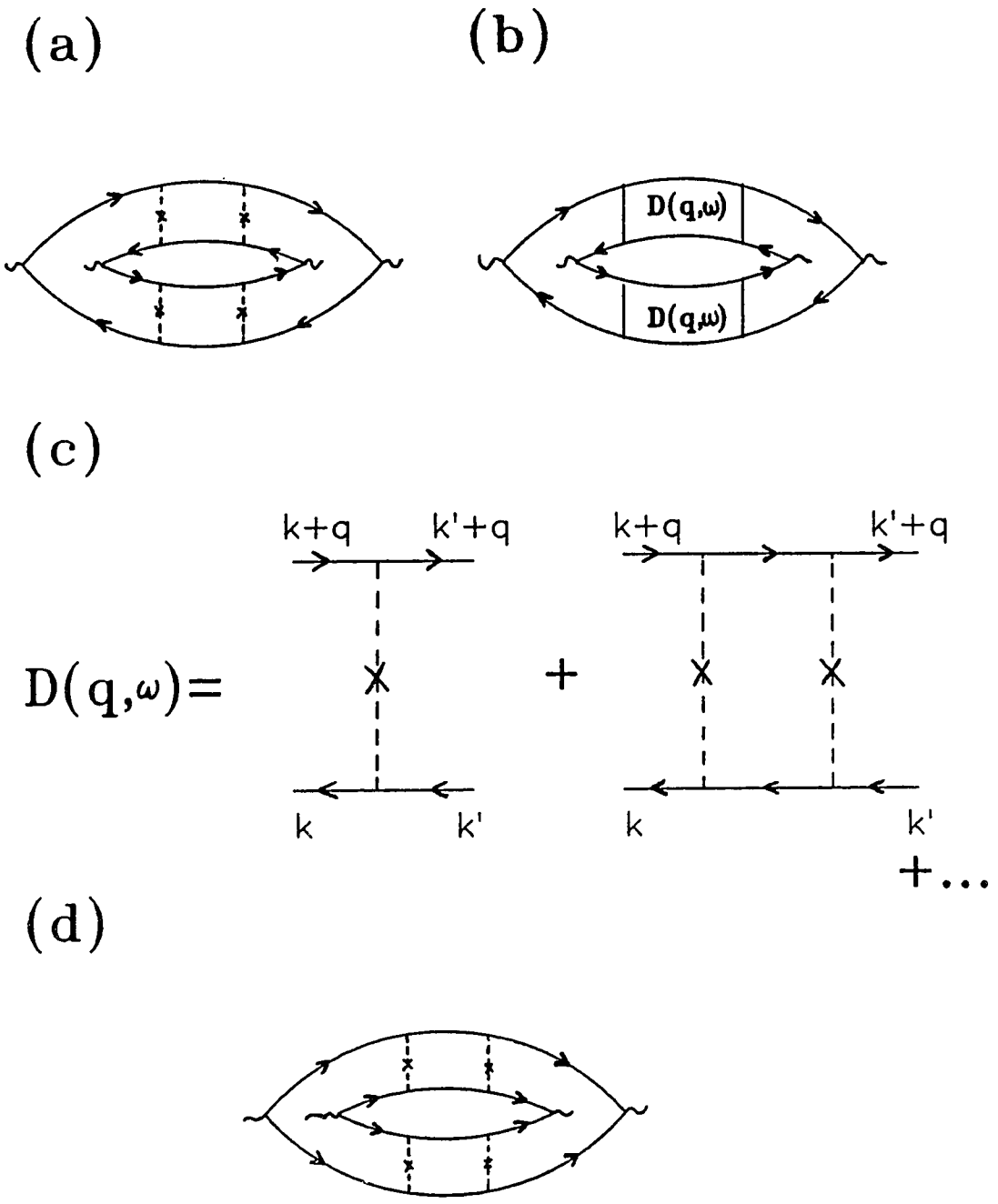

Figure 2.8. Some of the diagrams which contribute to $\delta\sigma^2$

the presence of a magnetic field affects the phase of an electron, changing the magnetic field by a sufficiently large amount randomises the phases of the interfering electrons. Changing the impurity configuration has the same effect. The amount the magnetic field must change to sufficiently randomise the phase is given roughly by $H_c \sim \Phi_o/\ell_\phi^2$ for a 2D film and $H_c \sim \Phi_o/W\ell_\phi$ for a 1D wire of width W. Φ_o is the normal flux quantum hc/e. A more rigorous proof of the validity of this hypothesis has been presented by Altshuler *et al.* [1986].

For statistical analyses, it is more useful to calculate the correlation function

$$F(H,\Delta H) = \langle G(H)G(H+\Delta H)\rangle - \langle G(H)\rangle^2, \qquad (2.29)$$

where G is the conductance of the sample [Lee and Stone, 1985]. In terms of Feynman diagrams, the quantity $G(H)G(H+\Delta H)$ is represented by two conductivity loops, one at magnetic field H and the other at $H+\Delta H$, and the average over impurity configurations is accomplished by connecting the loops by impurity lines [Altshuler, 1985; Lee and Stone, 1985]. Examples of such diagrams are shown in Fig. 2.8. In connecting the two loops by impurity lines, two distinct classes of diagrams are formed. In diagrams of the first class, an example of which is shown in Fig. 2.8a, a particle propagator of one loop is connected by impurity lines to a hole propagator of the other. The sum of all such graphs of the type in Fig. 2.8a is given by Fig. 2.8b, where the "Diffuson" $D(\mathbf{q},\omega)$ is given by the series in Fig 2.8c. $D(\mathbf{q},\omega)$, also called the particle-hole propagator, is independent of the absolute value H of the magnetic field but is a function of the field difference ΔH. Because of this, the conductance fluctuations are not suppressed even at high magnetic fields. The Diffuson obeys a diffusion equation similar to Eq. (2.6) for the Cooperon, except that the vector potential 2A in Eq. (2.6) is replaced by vector potential difference $\Delta\mathbf{A}$ [Lee and Stone,

1985; Altshuler and Khmelnitskii, 1985].

The second class of diagrams is identical to the first, except that a particle propagator of one loop is connected to a particle propagator of the other (Fig. 2.8d). The contribution of all such graphs in the second class, which are equal in number to those in the first class, is determined by the particle-particle propagator or Cooperon, which is dependent both on the field difference ΔH and the absolute field H. The contribution of the particle-particle graphs, which is equal to the contribution of the particle-hole graphs at zero magnetic field, is suppressed at high magnetic fields.

To calculate the conductance fluctuations in a 1D wire of length L, the diffusion equation must first be solved in the wire, subject, as in the case of weak localisation, to appropriate boundary conditions. In the original calculations by Altshuler and Khmelnitskii (AK) [Altshuler, 1985; Altshuler and Khmelnitskii, 1985] and Lee *et al.* [Lee and Stone, 1985; Lee *et al.*, 1986], the boundary condition applied was $D(\mathbf{r},\mathbf{r}')$ (or $C(\mathbf{r},\mathbf{r}')$)$=0$ at the ends of the wire. The details of the calculation of the diagrams can be found in the review paper by Lee, Stone and Fukuyama (LSF) [1986], whose notation we shall use in the following discussion. At $T=0$, their result for a one dimensional wire for $H=0$ and $\Delta H=0$ is

$$\mathrm{rms}(G) = [F(0,0)]^{1/2} \sim 0.729\ (e^2/h), \qquad (2.30)$$

so that, in terms of the reduced conductance $g=G/(e^2/h)$, the amplitude of the fluctuations is of order unity. In large magnetic fields, contributions from diagrams which contain a particle-particle propagator (as in Fig. 2.8d) are suppressed, and the value of F is reduced by a factor of two.

Consider now what happens at $T>0$. As the temperature is increased, ℓ_ϕ, which is temperature dependent in the absence of magnetic scattering, eventually becomes

shorter than the wire length L. The 1D wire now consists of a number $N=L/\ell_\phi$ of mutually incoherent regions, each of length ℓ_ϕ. Within each region, the amplitude of the fluctuations is rms[g(ℓ_ϕ)], but fluctuations in different regions are not correlated. Since R, the total resistance of the wire, is the sum of the resistances of each region, the total resistance fluctuation ΔR is given by the classical relation $(\Delta R)^2=\Sigma(\Delta R_i)(\Delta R_j)=N(\Delta R_i)^2$, where $\Delta R_i=\text{rms}[G(\ell_\phi)]R_i^2$ is the resistance fluctuation in the ith region. Then, since $\Delta G=(\Delta R)/R^2$, we obtain [Lee *et al.*, 1986].

$$\text{rms}(g) = \left[\frac{\ell_\phi}{L}\right]^{3/2} \text{rms}[g(\ell_\phi)]. \qquad (2.31)$$

Thus, the introduction of phase breaking reduces the amplitude of the fluctuations. This result can also be obtained by direct evaluation of the diagrams with finite ℓ_ϕ.

At finite temperature, there is another process which reduces the amplitude of the fluctuations. To obtain a physical understanding of this mechanism, we must go back to the interference picture of conductance fluctuations. Consider two electron waves at two different energies ΔE which interfere after a time t. The phase difference between the two electron waves due to the energy difference after this time is given by $\Delta Et/\hbar$. For the electrons to remain in phase, $\Delta Et/\hbar<1$. Now the distance an electron diffuses in time t is just given by $(Dt)^{1/2}$, where D is the diffusion coefficient. If the electrons diffuse more than a distance ℓ_ϕ, they will certainly be dephased by some inelastic process such as electron-electron scattering, so that we do not worry about dephasing due to energy differences on time scales longer than $t_c\sim\ell_\phi^2/D$. For the electrons to diffuse through a distance ℓ_ϕ without becoming dephased due to the energy difference ΔE, ΔE must be smaller than a critical energy $E_c\sim\hbar/t_c=D/\ell_\phi^2$. At $T>0$, the electron energies have a spread k_BT. Electrons within an energy band of width E_c will be coherent. The number of such

mutually incoherent bands is $N=k_BT/E_c$. The total conductance $g(\ell_\phi)$ is the sum of the conductances g_i of each of these bands, so that the conductance fluctuations scale with N as $rms[g(\ell_\phi)]=(N)^{1/2}\ rms(g_i)$, where $rms(g_i)$ is the zero temperature value given by Eq. (2.30). In terms of the length $\ell_T=(\hbar D/k_BT)^{1/2}$, $rms[g(\ell_\phi)]=(\ell_T/\ell_\phi)rms(g_i)$. The conductance fluctuations in a wire of length L then have the functional dependence [Altshuler and Khmelnitskii, 1985; Lee *et al.*, 1986]

$$rms(g) \sim \left[\frac{\ell_T}{L}\right]\left[\frac{\ell_\phi}{L}\right]^{1/2} , \qquad (2.32)$$

when $L>\ell_\phi>\ell_T$.

At finite ΔH, $F(\Delta H)$ can be obtained from Eq. (2.32) by putting in the field dependence of ℓ_ϕ, which is given by Eq. (2.11) with H replaced by $\Delta H/2$. $F(\Delta H)$ will then decay as a function of ΔH. Defining the field correlation length H_c as the value of ΔH at which $F(H_c)=(1/2)F(0)$, we obtain $H_c=(3/\pi)\Phi_o/\ell_\phi W$.

Unlike localisation, where the only temperature dependent length scale is ℓ_ϕ, the amplitude of conductance fluctuations is determined by two temperature dependent length scales, ℓ_ϕ and ℓ_T. Putting in some typical numbers for a wire of length L=2 μm at T=2 K, $\ell_T=0.2$ μm, and $\ell_\phi=1$ μm, we get $rms(g)\sim 0.07$. In contrast, the localisation correction for a short wire, using Eq. (2.24), is of order unity. Thus, it would appear that the amplitude of the fluctuations is small compared to the localisation correction. Part of this comparative reduction in the amplitude of the conductance fluctuations is due to the "energy averaging" factor (ℓ_T/L). We shall also see in the next section that the predicted value of the conductance fluctuations, Eq. (2.30), is a consequence of the boundary condition chosen for the problem, and that the conductance fluctuations can be much greater than e^2/h for samples in which $L<<\ell_\phi$ when more appropriate boundary conditions are used.

Conductance fluctuations have one further property that distinguishes them from weak localisation. The weak localisation corrections we have discussed are all symmetric in the magnetic field. For conductance fluctuations, however, it is possible for a current in the x direction to induce fluctuations in a perpendicular direction, so that the transverse conductance g_{xy} will also show fluctuations of order e^2/h, even in zero magnetic field [see, for example, Ma and Lee, 1987]. In a conventional four probe measurement of a mesoscopic sample, some component of g_{xy} may be included in a measurement of g_{xx}. The measured magnetoconductance will therefore be asymmetric with respect to field [Umbach *et al.*, 1984]. The problem of magnetic field asymmetry has also been treated by Buttiker [1986] in the transmission matrix approach. He showed that by appropriately switching measurement leads, one can extract a purely symmetric and a purely antisymmetric component of the MR. This was demonstrated experimentally by Benoit *et al.* [1986]. This asymmety is also seen in the samples studied in this thesis.

2.4.2 Effect of Measurement Probes

Given the prediction that a 1D metal wire should show conductance fluctuations with the universal amplitude of e^2/h, the discovery of conductance fluctuations with amplitude much greater than e^2/h in 1D metal and silicon wires in the regime $L<\ell_\phi$ came as a surprise [Benoit *et al.*, 1987; Skocpol *et al.*, 1987]. The anomalously large conductance fluctuations are now understood to be due to the effect of the measurement probes.

To understand the prediction of the amplitude of the fluctuations being of order e^2/h, we must go back to the boundary conditions used to derive Eq. (2.30). The

problem involves solving the diffusion equation for $D(\mathbf{r},\mathbf{r}')$ (or $C(\mathbf{r},\mathbf{r}')$) in the sample geometry, with appropriate boundary conditions. (We shall use $C(\mathbf{r},\mathbf{r}')$ in the discussion here.) The amplitude of the conductance fluctuations is then proportional to $\int d\mathbf{r}d\mathbf{r}' |C(\mathbf{r},\mathbf{r}')|^2$. (See Appendix II). Now the boundary condition applied in the original papers by AK and LSF is that $C(\mathbf{r},\mathbf{r}')=0$ at the ends of the wire. As discussed in the section on weak localisation, this corresponds to the case $\eta=\infty$. We saw that this value of η gave the lowest average C in the wire. A finite value of η would give a larger value of C in the wire, and hence a larger amplitude of the conductance fluctuations. Physically, the condition $\eta=\infty$ corresponds to an electron in the wire diffusing into the probes with no chance of returning phase coherently. A finite value of η corresponds to a finite probability that the electron will return to the wire phase coherently, and thus contribute to the conductance fluctuations.

Our qualitative analysis of the effect of different measurement probe configurations on weak localisation can be directly extended to discuss conductance fluctuations. Consider first the case $\eta=0$, which corresponds to a wire with no measurement probes. Since the value of C is the largest in this configuration, the amplitude of the conductance fluctuations will also be the largest. Adding probes will increase the value of η, and thus reduce the amplitude of the conductance fluctuations. For example, we should expect that of the three measurement configurations shown in Fig. 2.6, Fig. 2.6c should have the largest amplitude of conductance fluctations and Fig. 2.6b the smallest. We should also expect that the width of the 1D probes in Fig. 2.6c should affect the amplitude of the conductance fluctuations, since the width affects the parameter η. As we found for the case of weak localisation, the specific measurement probe configuration should become

irrelevant when $L >> \ell_\phi$.

A more quantitative calculation of the correlation function F involves evaluating $\int d\mathbf{r}d\mathbf{r}' |C(\mathbf{r},\mathbf{r}')|^2$, where the integral over $\mathbf{r}$ is a line integral over the path from one voltage probe to the other voltage probe, and the integral over $\mathbf{r}'$ is an integral over the path from one current probe to the other current probe. The complete integral can be separated into two contributions [DiVincenzo and Kane, 1988; Hershfield and Ambegaokar, 1988]. The first contribution is an integral over that part of the sample common to both the current and voltage paths, and was shown by the authors above to be equal to $F_{sa}=F_s-F_a$, where F_s is the component of the correlation function which refers to the fluctuations symmetric in the magnetic field, and F_a the component which refers to fluctuations antisymmetric in the field. The second contribution is an integral over the measurement probes, and is equal to F_a alone.

The correlation function has been calculated by a number of authors for wires with 1D probes [Maekawa *et al.*, 1987; Kane *et al.*, 1988; DiVincenzo and Kane, 1988; Hershfield and Ambegaokar, 1988], but not for wires with 2D probes. We calculate here the correlation functions for wires with 2D probes and wires with 1D probes. Due to the complexity of the calculation, we shall only evaluate the integral over the region of the sample common to both the current and voltage paths. Thus, what we obtain is only the component $F_{sa}=F_s-F_a$ of the correlation function. Furthermore, the calculation does not include the effects of energy averaging, and we neglect the diagrams with two Cooperons, so that our result is valid only in large magnetic fields where the Cooperon contribution is suppressed. Finally, since the integrals over $\mathbf{r}$ and $\mathbf{r}'$ are difficult to calculate analytically, we evaluate them numerically.

Figure 2.9 shows F_{sa} for two short wires with different probe configurations,

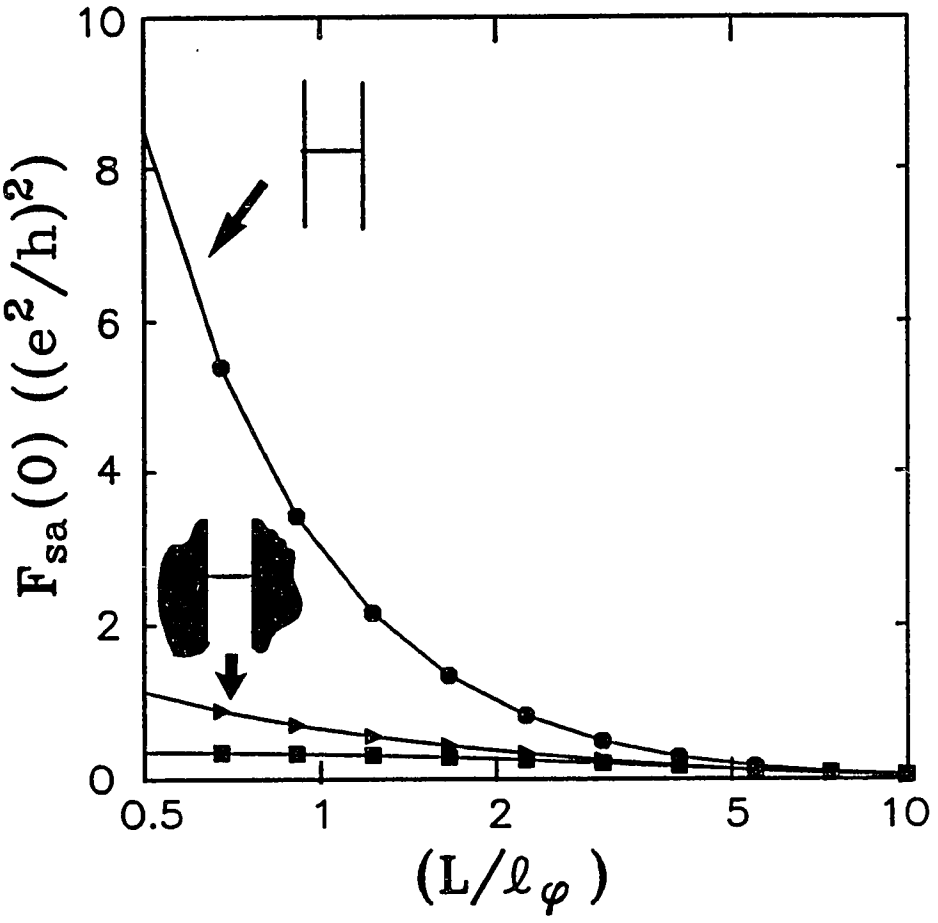

Figure 2.9. Conductance fluctuation correlation function F_{sa} for wires with different probe configurations. $\alpha=0.05$ for all wires. Circles, short wire with four narrow probes, $\eta=0.1$; triangles, short wire with two 2D probes, $\eta=0.5$; squares, short wire with $\eta=10^8(\sim\infty)$, corresponding to the boundary condition $C(\mathbf{r},\mathbf{r}')=0$ at the ends of the wire.

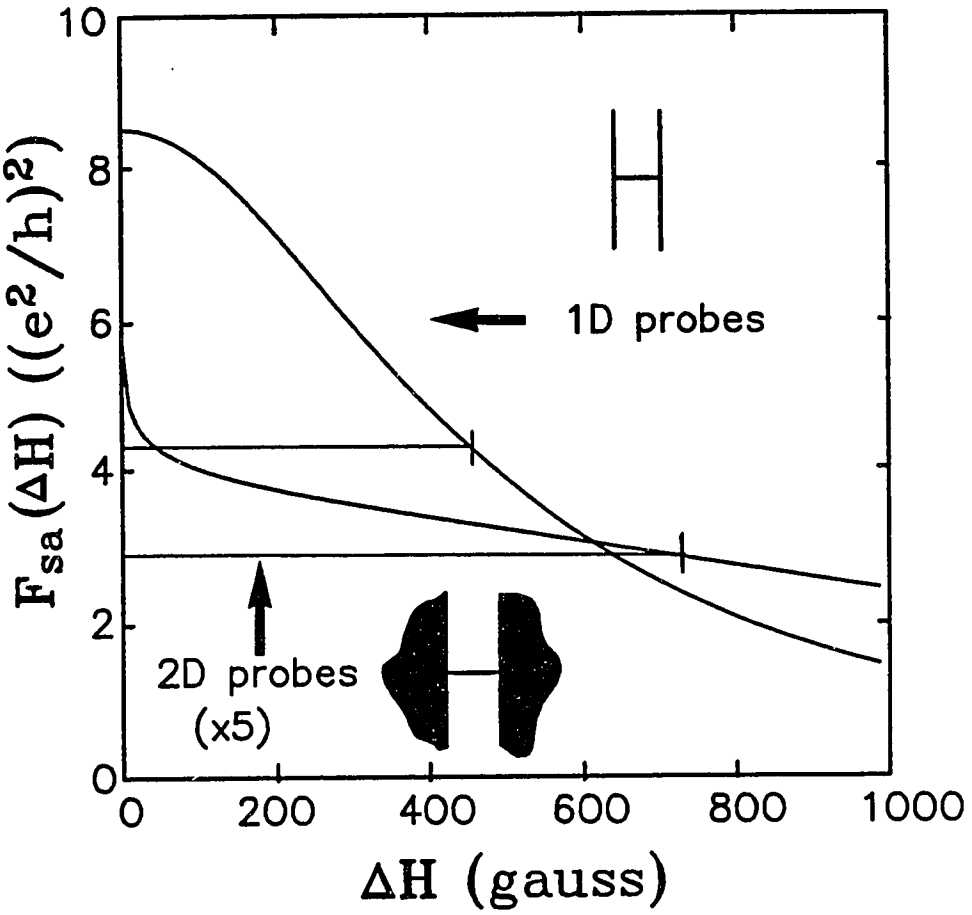

Figure 2.10. $F_{sa}(\Delta H)$ at T=0 for wires with different probe configurations. W=0.05 μm, L=0.5 μm, and $\ell_\phi(0)=1.0$ μm, corresponding to $\alpha=0.05$ at zero field. Curve marked "1D probes" is for a short wire with four narrow probes of width $W_p=0.05$ μm (Fig. 2.6c), corresponding to $\eta=0.1$. Curve marked "2D probes" is for a short wire with two 2D probes (Fig. 2.6b) with $\ell_{\phi 2D}=4.5$ μm and $\ell=15$ nm, corresponding to $\eta=0.49$ at zero field. The correlation field H_c for both wires is also shown.

one with four narrow measurement probes, and the other with two 2D probes. For $L<\ell_\phi$, $F_{sa}(0)$ for both wires is larger than $(e^2/h)^2$, but as we go to smaller values of L/ℓ_ϕ, $F_{sa}(0)$ for the wire with narrow probes increases much more rapidly than that for the wire with wide probes, as expected from our discussion in the preceding paragraphs. For $L>>\ell_\phi$, $F_{sa}(0)$ for both wires has the same value. For comparison, we also show the correlation function for a short wire with $\eta=\infty$, corresponding to the boundary condition $C(\mathbf{r},\mathbf{r}')=0$ at the ends of the wire.

In addition to the amplitude of the conductance fluctuations, we find that, in analogy to the effects of probes on weak localisation, the measurement probes also affect the dependence of the the correlation function $F_{sa}(\Delta H)$ on the the magnetic field difference ΔH. Figure 2.10 shows $F_{sa}(\Delta H)$ for two short wires with different probe configurations. $F_{sa}(\Delta H)$ for the wire with four narrow probes has a shape similar to that calculated by Lee et al. [1986] for a wire with $C(\mathbf{r},\mathbf{r}')=0$ at the ends. $F_{sa}(\Delta H)$ for the short wire with 2D probes, however, is more complicated. At low fields, $Fs_a(\Delta H)$ decreases rapidly with increasing ΔH. Beyond this, $F_{sa}(\Delta H)$ falls off more slowly with ΔH. The rapid decrease in the correlation function near zero ΔH is a signature of the 2D probes of this short wires. Note that the correlation field H_c, defined above by $F_{sa}(H_c)=(1/2)F_{sa}(0)$, is different for the two short wires, being much larger for the short wire with 2D probes, although L, W and $\ell_\phi(0)$ are the same for both wires. The field dependence of $F_{sa}(\Delta H)$, and therefore H_c, are determined by the probes when $L<\ell_\phi$. Thus, the simple estimate of $H_c\sim\Phi_o/\ell_\phi W$ may not be correct in the mesoscopic size regime.

A note about the validity of the calculation presented above. First, this calculation, like the calculations on wires with 1D probes by the other authors

mentioned above, does not include the effects of energy averaging. Thus, the results are not strictly valid at finite temperature, where the the effects of energy averaging are expected to be important. Second, Figs. 2.9 and 2.10 show only the component $F_{sa}=F_s-F_a$ of the correlation function. In the experiments on short wires to be described later, the quantity we measure is $Fs+F_a$, so that, for a quantitative comparison, one needs to calculate the component F_a as well. For a short wire with 1D probes, the calculation has been done by a number of authors [DiVincenzo and Kane, 1988; Hershfield and Ambegaokar, 1988; Baranger *et al.*, 1988]. They find that in the limit $L<<\ell_\phi$, $F_s(0)$ and $F_a(0)$ are approximately equal, whereas in the limit $L>\ell_\phi$, the major contribution to F(0) comes from $F_s(0)$. The calculation of F_a for a short wire with 2D probes is more difficult, and we can only estimate the integrals involved in the calculation. We find that, in the regime $L<\ell_\phi$, the component F_a for the wire with 2D probes is much smaller than the corresponding quantity for the wire with 1D probes, as is the case for the component F_{sa}. Thus, we expect the qualitative differences between the wires with 1D probes and the wires with 2D probes seen Fig. 2.9 should still be observable when F_a is taken into account.

2.4.3 The hc/e Aharonov-Bohm Effect

Perhaps the clearest demonstration of the quantum interference nature of conductance fluctuations is to be found in a single metal loop. If A is the area of the loop, the correlation function F oscillates as a function of the magnetic flux difference $\Delta\Phi=(\Delta H)A$ through the loop. For $\ell_T<\ell_\phi$, $F(\Delta\Phi)$ for a single isolated loop is given by (Appendix II)

$$F(\Delta\Phi) \sim \left[\frac{\ell_T}{\pi a}\right]^2 \left[\frac{\ell_\phi}{\pi a}\right] \left[1 + 2 \sum_{n=1}^{\infty} \exp[-(2\pi na/\ell_\phi)] \cos(2\pi n\Delta\Phi/\Phi_o)\right], \quad (2.33)$$

where a is the radius of the loop. This result has also been derived by Aronov and Sharvin [1987]. Hence the magnetoconductance of a single metal loop should show oscillations of period $\Phi_0 = hc/e$ with amplitude $\sim (\ell_T/a)(\ell_\phi/a)^{1/2} \exp(-\pi a/\ell_\phi)$. ℓ_ϕ in Eq. (2.33) has a magnetic field dependence given by Eq. (2.11) (with H replaced by $\Delta H/2$), so the oscillations of $F(\Delta\Phi)$ do not persist to high values of $\Delta\Phi$, but decay on a field scale of H_c. The amplitude of $F(\Delta\Phi)$ is about two orders of magnitude larger than the value $(e^2/h)^2$. Because of the exponential, the amplitude of the oscillations is strongly dependent on ℓ_ϕ. They can only be observed in samples in which $\ell_\phi \sim \pi a$. Note that in the limit $\pi a >> \ell_\phi$, we are left with the result for a wire, Eq. (2.32).

The calculation in Appendix II is for a single loop with no measurement probes. We expect that the presence of measurement probes will reduce the amplitude of the conductance fluctuations. The correlation function for a single loop with leads has been calculated by Isawa *et al.* [1986] and DiVincenzo and Kane [1988]. They find that the presence of leads does indeed reduce the amplitude of the oscillations in the limit $\ell_\phi \geq \pi a$.

The hc/e Aharonov-Bohm oscillations are a special case of conductance fluctuations, and thus all of the characteristics that distinguish conductance fluctuations are also relevant for the hc/e oscillations. Like conductance fluctuations, hc/e oscillations persist to very high magnetic fields. In this, they may be contrasted to the AAS hc/2e oscillations, which are found only at low magnetic fields. The hc/e oscillations may also be asymmetric in the magnetic field [DiVincenzo and Kane, 1988], whereas the AAS hc/2e oscillations are symmetric. Given our belief that the underlying physics of both effects is the same, however, one should be able to

observe both hc/e and AAS hc/2e oscillations in a single loop. As we shall see in the next section, with the inclusion of spin-orbit scattering and scattering by magnetic impurities, the relevant phase breaking lengths for the hc/e and the hc/2e Aharonov-Bohm effects are no longer the same, so that oscillations of both periods may not always be observable in a single loop.

2.5 Electron Dephasing Mechanisms

In our discussion of quantum interference so far, we have stressed the importance of ℓ_ϕ, the electron phase breaking length, which was introduced phenomenologically, without justifying its introduction or discussing the processes which contribute to a finite value of ℓ_ϕ. In this section, we will outline some of the electron scattering mechanisms which contribute to the electron phase breaking rate τ_ϕ^{-1}, which is related to ℓ_ϕ by $\tau_\phi^{-1}=\ell_\phi^2/D$. There are a large number of scattering mechanisms which can contribute to the dephasing rate, but we shall only discuss those which are important for the samples studied in this work. These include electron-electron scattering, electron-phonon scattering, spin-orbit scattering, and scattering by magnetic impurities.

2.5.1 Electron-Electron Scattering

The Coulomb interaction between electrons leads to a finite decay rate for electrons in a particular energy state. For a metal without any disorder, the inelastic electron-electron scattering rate can be derived from simple phase space arguments, and is found to be proportional to T^2 [Ziman, 1960]. Quantitatively, $\tau_{ee}^{-1} \sim 10^5$-10^6 T^2 sec^{-1} for most metals. In the presence of impurities, the interaction between

electrons is modified due to the diffusive motion of the electrons. The diffusive motion increases the interaction time between electrons, increasing the scattering rate, which now goes as $\tau_{ee}^{-1} \sim T^{d/2}$. The dimension d of the interaction is determined by the thermal diffusion length ℓ_T, in the same way as the dimension of weak localisation effects is determined by ℓ_ϕ.

Predictions of τ_{ee}^{-1} for electrons in disordered metals have been made by many authors. Schmid [1974] and Altshuler and Aronov [1978, 1979] derived the $T^{d/2}$ dependence using a transport equation approach. Using impurity averaged perturbation theory, Altshuler and Aronov [1981] obtained the scattering rate

$$\frac{1}{\tau_{ee}} = \frac{1}{4} \frac{R_\square}{(\pi\hbar/e^2)} \frac{k_B T}{\hbar} , \tag{2.34}$$

for d=2, and for d=1,

$$\frac{1}{\tau_{ee}} = \frac{1}{\pi^2} \frac{R_\square}{(\pi\hbar/e^2)} \frac{D}{W} \left[\frac{k_B T}{2\hbar D}\right]^{1/2} . \tag{2.35}$$

Abrahams *et al.* [1981] obtained a similar result for d=2, but with a logarithmic temperature dependent factor

$$\frac{1}{\tau_{ee}} = \frac{1}{2} \frac{R_\square}{(\pi\hbar/e^2)} \frac{k_B T}{\hbar} \ln(T_1/T) , \tag{2.36}$$

where $k_B T_1 = (k_f \ell)^2 \hbar D \kappa^2$ and $\kappa = 2me^2/\hbar^2$ is the inverse screening length. Later, Lopes dos Santos [1983] recalculated τ_{ee}^{-1} self consistently and obtained

$$\frac{1}{\tau_{ee}} = \frac{1}{4} \frac{R_\square}{(\pi\hbar/e^2)} \frac{k_B T}{\hbar} \ln(T_2/T) \tag{2.37}$$

where $T_2 = 4T_1$. For Al, $T_1 \sim 9 \times 10^5 \, (k_F \ell)^2$ K. Note that the predictions Eqs. (2.36) and

(2.37) for the quasiparticle scattering rate in 2D are considerably different from Eq. (2.34). For $k_f\ell \sim 50$, the logarithmic term in Eq. (2.37) enhances the rate by a factor of ~20 over the prediction of Eq. (2.34) at T=2 K.

Eqs. (2.33)-(2.37) give the decay rate for quasi-particles due to the Coulomb interaction between them. For quantum interference effects such as weak localisation and conductance fluctuations, we are interested in τ_ϕ^{-1}, the electron phase breaking rate. In the absence of any other phase breaking mechanisms, how is this rate related to τ_{ee}^{-1}?

τ_ϕ^{-1} due to electron-electron interactions can be calculated directly from the particle-hole and particle-particle ladders by introducing interaction lines in the ladders in all possible ways. In doing this, we must keep in mind an important difference between the impurity ladders in diagrams for weak localisation and conductance fluctuations [Lee *et al.*, 1986]. In the calculation for conductance fluctuations, the impurity ladders connect conductivity loops that refer to two different measurements of the conductivity. Only interactions which remain constant between the two measurements are allowed to connect the two loops. For example, for the particle-hole ladder (or Diffuson), the diagrams shown in Fig. 2.11a are allowed, but diagrams in which the interaction lines connect the two propagators (e.g., Fig. 2.11b) are not allowed. The same holds true for the particle-particle ladder, or Cooperon. In the diagrams for weak localisation, however, the two propagators the ladders connect correspond to the same measurement, and hence diagrams like Fig. 2.11b must also be included. In this case, we need consider only the Cooperon; diagrams with interactions for the Cooperon are shown in Figs. 2.11c and 2.11d.

We first discuss τ_ϕ^{-1} for weak localisation. Fukuyama and Abrahams (FA) [1983]

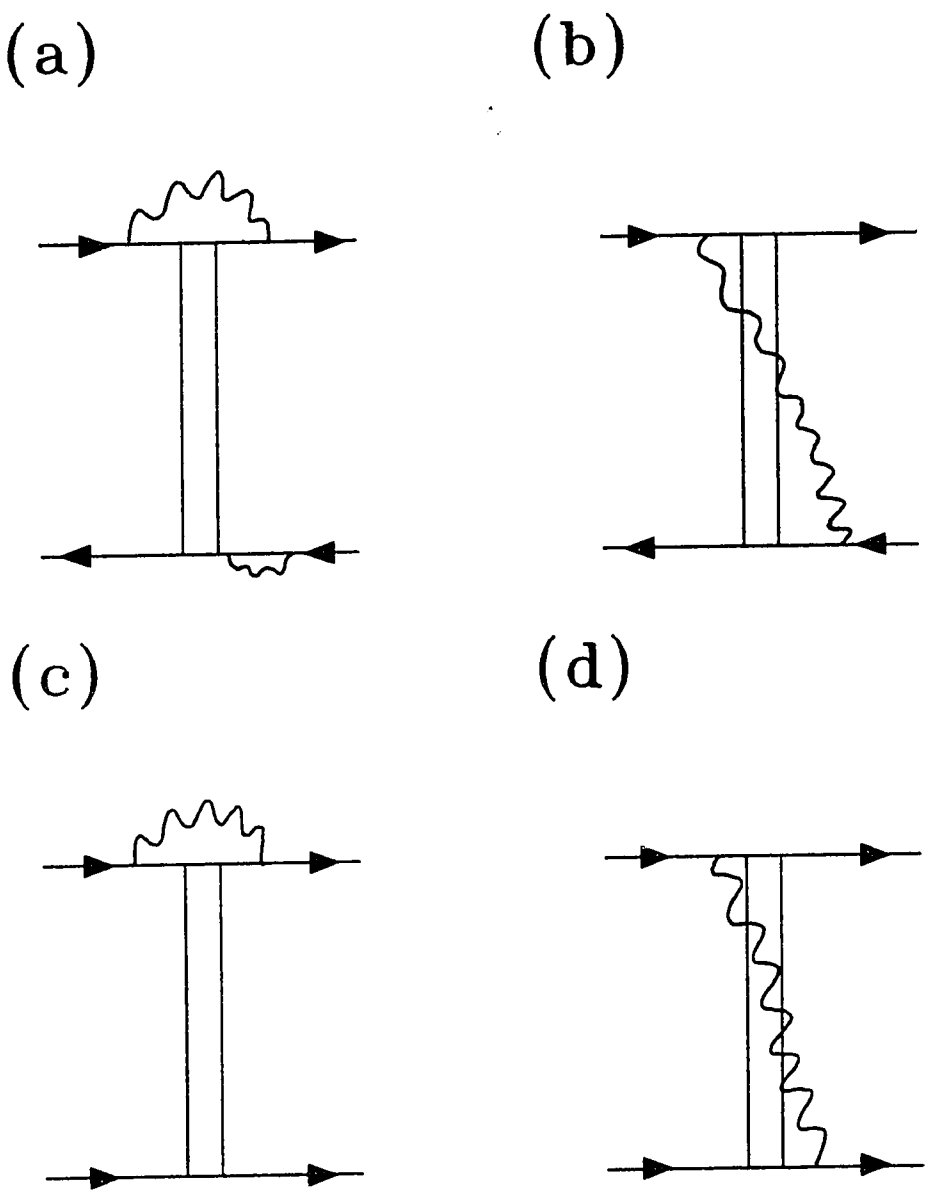

Figure 2.11. Impurity ladders with Coulomb interactions. (a),(b). Particle hole ladder. (c)-(d). Particle particle ladder. The bars denote impurity interactions and the wavy lines the Coulomb interaction.

have explicitly calculated the decay rate of the Cooperon in the presence of Coulomb interactions. In their calculations, contributions from diagrams like Figs. 2.11c are included, but contributions from diagrams like Fig. 2.11d are ignored as being less singular. The result they obtain for the decay rate of the Cooperon in 2D is identical to their quasiparticle rate, Eq. (2.36).

A different approach for calculating the Cooperon decay rate was adopted by Altshuler, Aronov and Khmelnitskii (AAK) [1982]. Their starting point is the diffusion equation for the Cooperon, Eq. (2.4), in the presence of random electromagnetic field fluctuations. These fluctuations arise from the motion of the electrons themselves, and have a spectrum given by the fluctuation dissipation theorem [Callen and Welton, 1951]. Other electrons are scattered by these fluctuations, giving rise to an effective electron-electron interaction. Their result for a 2D film is

$$\frac{1}{\tau_N} = \frac{1}{2}\,\frac{R_\square}{(\pi\hbar/e^2)}\,\frac{k_B T}{\hbar}\,\ln\left[\frac{(\pi\hbar/e^2)}{R_\square}\right] = A_1 T\ , \tag{2.38}$$

and for a 1D wire,

$$\frac{1}{\tau_N} = \left[\frac{R_\square}{\hbar/e^2}\,\frac{k_B}{\hbar}\,(D/2)^{1/2}\,\frac{T}{W}\right]^{2/3} = A_{2/3}T^{2/3}, \tag{2.39}$$

where W is the width of the wire.

Equation (2.38) is different from the prediction of FA, Eq. (2.36). For a typical $R_\square$ of 2 ohms, the temperature independent logarithm in Eq. (2.38) contributes a factor ~9, while, as we have seen, the logarithm in Eq. (2.36) gives a factor ~20 at T=2 K, and is divergent as T→0. The discrepancy was resolved by Aronov [1984] and Eiler [1984]. They pointed out that including a contribution from a process similar in form to the one in Fig. 2.11d (which was neglected by FA) reduces the rate from Eq.

(2.38) to Eq. (2.34). Experiments on 2D films and 1D wires [Santhanam *et al.*, 1987] have confirmed that τ_N^{-1} is the contribution to the weak localisation dephasing rate from electron-electron interactions, and that ℓ_T is the length that determines the dimensionality of the scattering rate. Thus, the phase decay rate for weak localisation is not the same as the quasiparticle decay rate.

To determine the dephasing rate for conductance fluctuations, we need to determine the decay rate of the Cooperon and the Diffuson in the absence of any interactions connecting the two propagator lines. The decay rate for the Cooperon under these conditions is the result of FA, Eq. (2.36). The decay rate of the Diffuson has been calculated by Castellani *et al.* [1986], using the same approximation as FA. In 2D, they find the quasi-particle rate, Eq. (2.36). In 1D, one might expect that the dephasing rate for conductance fluctuations should be given by the quasiparticle decay rate, Eq. (2.35), if only electron-electron interactions are taken into account. Experimentally, this does not seem to be the case. Eq. (2.35) predicts a rate which, for our sample parameters, is about three orders of magnitude smaller than that predicted by Eq. (2.39). This implies that in 1D, the phase coherence length for conductance fluctuations should be a factor of ~30 larger than the phase coherence length for weak localisation. This difference is not seen. As shown by Aronov [1984] and Eiler [1984] for two dimensions, the rate predicted by FA is larger than that predicted by AAK because they did not consider certain scattering processes which reduce the rate. The same situation should apply in 1D, so that the appropriate rate for conductance fluctuations in 1D should be larger than that predicted by Eq. (2.39) for weak localisation. To date, the calculation in 1D has not been done explicitly.

2.5.2 Electron-Phonon Scattering

At temperatures higher than a few degrees, the dominant contribution to electron dephasing comes not from electron-electron interactions, but from the inelastic scattering of electrons by phonons. The electron phonon scattering rate can be written in the form [Keck and Schmid, 1976]

$$\frac{1}{\tau_{ep}} \sim \int d\omega \, \frac{\alpha^2 F(\omega)}{\mathrm{sh}(\hbar\omega/k_B T)} \, ,$$

where $\alpha^2F(\omega)$ is the Eliashberg function, which contains details of the electron-phonon interaction. Rammer and Schmid [1986] showed that this is also the dephasing rate for weak localisation. For a clean metal in the Debye approximation, $\alpha^2F(\omega)\sim\omega^2$, giving a rate $\tau_{ep}^{-1}\sim T^3$ for $k_BT << \hbar\omega_D$, where ω_D is the Debye frequency. Quantitatively, $\tau_{ep}^{-1}\sim 10^7\ T^3\ \mathrm{sec}^{-1}$ [Kaplan *et al.*, 1976]. More rigorous calculations taking into account Fermi surface effects give essentially the same results. For example, for Al, Lawrence and Meador [1978] obtain $\tau_{ep}^{-1}=0.91\times10^7\ T^3\ \mathrm{sec}^{-1}$.

The T^3 dependence of τ_{ep}^{-1} is valid for a clean metal for which $q_p\ell >> 1$, where $q_p=4k_BT/\hbar v_s$ is the most probable phonon wavevector, and v_s the velocity of sound. In the presence of a large number of impurities, the interaction between electrons and phonons is modified. While there is general agreement on the T^3 dependence of the rate in clean metals, there is yet no consensus on the temperature dependence in the dirty limit. Keck and Schmid [1976] obtained $\tau_{ep}^{-1}\sim R_\square T^4$, while Bergmann [1971] and Takayama [1973] found $\tau_{ep}^{-1}\sim R_\square T^2$. More recently, Belitz and Das Sarma [1987] derived a temperature dependence which is not strictly a power law, but mimics T^2 for T=4-20 K. For the samples in this thesis, $q_p^{-1}\sim$50-100 Å, whereas $\ell\sim$150 Å, so that we are nominally in the clean limit.

We have not yet considered the dimensionality of the electron-phonon

interaction. The dimensionality of the electron-phonon interaction is determined by the most probable phonon wavelength $\lambda_p=2\pi/q_p$. In the presence of impurities, the appropriate length scale is more likely ℓ, since phonons with a wavelength larger than this are less effective in scattering electrons [Pippard, 1955; Ziman, 1960]. In either case, for our samples in the temperature range where electron-phonon scattering is dominant, λ_p is smaller than any sample dimension. In addition, the samples are mounted on a substrate with which there is good thermal contact, so that the electron-phonon rate is given by the three dimensional result. The total phase breaking rate for quantum interference effects is then

$$\tau_\phi^{-1} = \tau_{ee}^{-1} + \tau_{ep}^{-1} = \tau_{ee}^{-1} + A_3T^3, \qquad (2.40)$$

where τ_{ee}^{-1} is the dephasing rate due to electron-electron interactions.

2.5.3 Spin-dependent Scattering

One of the remarkable features of electron quantum interference effects has been their sensitivity to scattering mechanisms which depend on the spin of the electrons. In this section, we shall first discuss the effect of spin-dependent scattering of electrons on weak localisation and conductance fluctuations. We shall then discuss the mechanisms which give rise to spin dependent scattering in our samples.

Let τ_{so} be the mean time between spin-orbit scattering events and τ_s be the corresponding time for scattering off magnetic impurities. These times are related to the appropriate diffusion lengths by $\ell_{so}^2=D\tau_{so}$ and $\ell_s^2=D\tau_s$. In the presence of spin dependent interactions, the spin-singlet and spin-triplet parts of the Cooperon and the Diffuson are no longer degenerate [Hikami *et al.*, 1980]. For weak localisation, the

Cooperon splits into two components [see, for example, Altshuler *et al.*, 1982b],

$$C = (3/2)C^1(\ell_2) - (1/2)C^0(\ell_1),$$

where $C^{1,0}(\ell_\phi)$ satisfies Eq. (2.6) and

$$\ell_1^{-2} = \ell_\phi^{-2} + 2\ell_s^{-2}, \tag{2.41a}$$

$$\ell_2^{-2} = \ell_\phi^{-2} + (2/3)\ell_s^{-2} + (4/3)\ell_{so}^{-2}. \tag{2.41b}$$

The fractional resistance change will then have two terms [Santhanam *et al.*, 1984]

$$\frac{\Delta R}{R} = \frac{3}{2}\frac{\Delta R}{R}(\ell_2,H) - \frac{1}{2}\frac{\Delta R}{R}(\ell_1,H), \tag{2.42}$$

where $\Delta R/R$ is given by Eq. (2.27) for a 2D film, and Eq. (2.22) for a 1D wire. When $\ell_{so} << \ell_\phi, \ell_s$, the sign of the weak localisation correction is changed. Instead of negative MR, one sees positive MR at low magnetic fields. The samples studied in this thesis all have moderately strong spin-orbit scattering, and thus show positive MR at low fields.

For moderate spin-orbit scattering and scattering by paramagnetic impurities, it is shown in Appendix III that the conductance fluctuation correlation function $F(H,\ell_\phi)$ splits into a singlet part and a triplet part

$$F(H) = (3/4)F(H,\ell_4) + (1/4)F(H,\ell_3), \tag{2.43}$$

where

$$\ell_3^{-2} = \ell_\phi^{-2} + \ell_s^{-2}, \tag{2.44a}$$

and

$$\ell_4^{-2} = \ell_\phi^{-2} + \ell_s^{-2} + (4/3)\ell_{so}^{-2}. \tag{2.44b}$$

Note the difference in the coefficients of the terms between Eqs. (2.41) and (2.44). In the limit of strong spin orbit scattering, the rms amplitude of the fluctuations is reduced to half [Lee *et al.*, 1986]. With strong magnetic impurity scattering, the amplitude of the fluctuations goes to zero. The presence of spin dependent

scattering changes the temperature dependence of the conductance fluctuations. The temperature dependence is no longer given by a simple power law, but depends on the relative values of ℓ_ϕ, ℓ_s and ℓ_{so}, and their respective temperature dependences.

Spin-orbit Scattering

The interaction between an electron and the relativistically transformed electric field of an atom can be written in the form $\mathbf{L}\cdot\mathbf{s}$, where $\mathbf{L}$ is the orbital angular momentum of the electron and $\mathbf{s}$ is the spin angular momentum. If the atom is an impurity, it is convenient to think of this interaction as causing scattering between different conduction electron states. The spin-orbit interaction energy can be written in the form [Landau and Lifshitz, 1977]

$$H_{so} = iU_{so}(\hat{k}x\hat{k}')\cdot\sigma_{ss'},$$

where $\hat{k}$ is the unit vector in the direction of the k vector of the incoming electron, $\hat{k}'$ is the unit vector in the direction of the scattered electron, s and s' are their respective spin orientations, and $\sigma_{ss'}$ is the Pauli spin matrix. The scattering rate in the first Born approximation is then just

$$\tau_{so}^{-1} = U_{so}^2\Sigma|(\hat{k}x\hat{k}')_i|^2 , \qquad (2.45)$$

where the sum is over the directions i. This rate is independent of temperature. Now if the only elastic scattering is due to impurities which also cause the spin orbit scattering, then we should expect some constant ratio between the elastic scattering time τ and the spin orbit scattering time τ_{so}. In fact, Abrikosov and Gorkov [1962] predict

$$(\tau/\tau_{so}) \sim Z^4, \qquad (2.46)$$

where Z is the atomic number of the nucleus. If, on the other hand, the majority of

the elastic scattering is due to scattering off grain boundaries in the polycrystalline films, this relationship will not hold. Santhanam [1985] found that in films similar to the ones studied in this thesis, τ_{so} was proportional to τ, but the constant of proportionality was not the one predicted by Abrikosov and Gorkov. For our purposes, it is sufficient to note that τ_{so} for similarly prepared films has been found to be independent of temperature, and the spin-orbit scattering rates we obtain are in good agreement with previous studies on thin metal films studied by weak localisation [Santhanam, 1985; Wind, 1987] and superconducting tunnelling [Alexander *et al.*, 1986].

Scattering by Magnetic Impurities

The interaction of a conduction electron with a local moment is described by the exchange Hamiltonian $H_S \sim JS \cdot \sigma_{SS'}$, where J is the exchange integral which we shall consider a constant independent of temperature, S the spin of the local impurity moment and $\sigma_{SS'}$ the Pauli spin matrix of the conduction electron. Treating this as a scattering potential in the first Born approximation, one obtains the scattering rate [Yosida, 1957; Kondo, 1969]

$$\tau_s^{-1} \sim U_s^2 S(S+1). \qquad (2.47)$$

in zero external magnetic field, independent of temperature. This term includes both events in which the spin of the conduction electron is flipped, and events in which the electron is scattered without changing its spin. As we shall see later, only those events in which the spin of the electron is flipped destroy the phase of the electron. In the presence of a large external magnetic field H, the spin of the impurity is frozen, so that only events without spin flip are allowed. In this limit, the spin scattering rate reduces to $\tau_s^{-1} \sim U_s^2 S^2$ [Kondo, 1969], the contribution of non spin flip

scattering events alone. At low magnetic fields, the spin scattering rate decreases as the square of the average magnetisation of the impurity, which is proportional to H^2 [Kondo, 1969]

$$\tau_s^{-1} = U_s^2 S(S+1)[1 - (4/27)(2\mu_B H/k_B T)^2], \qquad (2.48)$$

where μ_B is the Bohr magneton. The magnetic field dependence of the magnetic impurity scattering time is not important for weak localisation, because weak localisation effects are present only at low magnetic fields. Conductance fluctuations, however, persist to high magnetic fields. If fluctuation effects are suppressed by scattering off paramagnetic impurities, the application of a magnetic field will reduce the spin flip scattering rate and increase the amplitude of the conductance fluctuations.

There is a contribution to τ_s^{-1} in the second Born approximation which gives a logarithmic temperature dependence to the spin scattering rate [Kondo, 1964]. The contribution to the rate can be as large or larger than the first order contribution [Heeger, 1969]. We shall use the Hamann-Bloomfield-Nagaoka result for the scattering rate due to magnetic impurities [Hamann, 1967; Bloomfield and Hamann, 1967]

$$\frac{1}{\tau_s} = \frac{N_m}{\pi\hbar N(0)}\left[1 - \frac{\ln(T/T_K)}{[\pi^2 S(S+1) + \ln^2(T/T_K)]^{1/2}}\right]. \qquad (2.49)$$

where N_m is the magnetic impurity concentration, N(0) is the electron density of states at the Fermi energy and $T_K \sim \exp[-1/JN(0)]$ is the Kondo temperature. The first term in the brackets is the contribution from non spin-flip events, and the second from spin-flip scattering events. When $T/T_K >> 1$, we regain the logarithmic temperature dependence of the Kondo effect [Kondo, 1964]. For $T << T_K$, the impurity spin is compensated and the spin-flip contribution goes to zero. Equation (2.49) is

found to provide a good description of the experimental data to almost a decade below T_K [Heeger, 1969].

The first experiments to measure the magnetic scattering rate using weak localisation found a temperature independent scattering rate [Bergmann, 1982], consistent with Eq. (2.47). It now appears that these experiments were in the regime $T>>T_K$, where the logarithmic variation of τ_s^{-1} over the temperature range studied was small enough for τ_s^{-1} to appear a constant. More recent investigations infer a temperature dependent rate consistent with only the spin-flip part of Eq. (2.49) [Bergmann, 1986, 1987; Bergmann *et al.*, 1987; Van Haesondonck *et al.*, 1987]. Thus, not only do these experiments confirm that magnetic impurity scattering affects weak localisation, but also that only the spin-flip contribution is important. In consequence, when we write τ_s^{-1} in what follows, we shall be referring to only the spin-flip component.

The field dependence of the magnetic scattering rate is now a little more complicated. For $T>>T_K$, we essentially have free spins, so that the rate should decrease again as H^2 [Kondo, 1969]. In the vicinity of T_K, however, the field dependence is slower; τ_s^{-1} decreases as ln(H) [Daybell, 1973].

The results on magnetic scattering that we have discussed so far have assumed that the concentration of impurities is low enough that each impurity spin can be considered essentially independent. In reality, however, even at the lowest concentrations, local moments interact with each other via the RKKY interaction [Ziman, 1964]

$$H_{RKKY} \sim J^2 S_i \cdot S_j \cos(2k_F r_{ij})/r_{ij}^3$$

where S_i is the spin on the ith impurity and r_{ij} is the distance between the ith and

the jth impurities. The sign of the interaction depends on r_{ij}, which is a random quantity. At sufficiently high concentrations and sufficiently low temperatures, the impurity spins are frozen in random directions, and a spin glass phase is formed. The temperature T_g at which this freezing starts to occur is proportional to the strength of the RKKY interaction, which goes as r_{ij}^{-3}. Since $r_{ij}^{-3} \sim N_m$, the impurity concentration, the spin glass temperature $T_g \sim N_m$. Now when $T < T_g$, spin-flip scattering is suppressed since the impurity spins are frozen, and so if $T_g > T_K$, the Kondo effect will be not be observed. Since T_K is essentially independent of the impurity concentration, we require a low concentration of impurities to observe the Kondo effect. The competition between the spin glass phase and the Kondo effect has been the subject of recent experimental work [Van Haesendonck *et al.*, 1987].

There is another mechanism by which magnetic impurities can cause dephasing of electrons, a mechanism which distinguishes between weak localisation and conductance fluctuations. In the spin glass phase, large random internal magnetic fields are present in the metal. For weak localisation, the effect of these internal fields is exactly the same as the effect of a large external field: the weak localisation correction is suppressed. One does not therefore expect to see weak localisation in a spin glass. Conductance fluctuations, however, are not suppressed by large magnetic fields. Since there is little spin-flip scattering in the spin glass phase, conductance fluctuations will essentially remain unaffected by the magnetic impurities. This conclusion, of course, neglects the dynamics of the spin glass state. In practice, we should expect to see some dephasing caused by the relaxation of spins as a function of temperature and magnetic field.

2.6 Additional Contributions to the Magnetoresistance

In addition to weak localisation and conductance fluctuations, there are other contributions to the MR of thin metal films. The most familiar of these is the classical MR. Further contributions arise due to the effects of superconducting fluctuations and electron-electron interactions.

A discussion of the classical MR of the samples used in this work can be found in Ashcroft and Mermin [1976] and Santhanam [1985]. Since the temperature independent elastic scattering time is the shortest relaxation time in our samples, the classical MR is independent of temperature. The weak localisation contribution is appreciable only in classically weak magnetic fields, where the classical MR is small. For conductance fluctuations and the hc/e Aharonov Bohm effect, we are interested in deviations from the background signal or oscillations with a particular period. In either case, separating the contributions of interest from the classical MR is not a problem. Likewise, the contribution of electron-electron interactions to the MR is typically much smaller than the contribution of weak localisation and conductance fluctuations [see Santhanam, 1985], and can be neglected. Superconducting fluctuations, on the other hand, give an appreciable temperature-dependent contribution to the MR in the magnetic field range of interest, and must therefore be taken into account.

Just above the superconducting transition temperature T_c, the average Cooper pair density is zero, but fluctuations involving small superconducting "islands" do occur. These islands, the Azlamazov-Larkin (AL) fluctuations, increase the conductivity of the metal [Aslamazov and Larkin, 1968]. The increase in the conductivity, however, is appreciable only very close to T_c. The samples in this

thesis were measured at temperatures where the AL fluctuations are negligible, so we shall not consider them in our analysis.

An additional contribution to the conductivity, the Maki-Thompson (MT) contribution, arises from the strong correlation due to the electron-phonon interaction between a pair of electrons having nearly equal and opposite momenta [Maki, 1968; Thompson, 1970]. This correlation is similar to the correlation between particles of nearly opposite momenta that leads to weak localisation. In the case of weak localisation, the correlation is induced by the impurity interaction; for the MT contribution, the interaction is mediated by phonons. This interaction leads to superconductivity below T_c. Above T_c, it leads to an increase in the conductivity, even at relatively high temperatures [Larkin, 1980]. The change in the conductivity is again proportional to $C(\mathbf{r},\mathbf{r})$, $\Delta\sigma_{MT}\sim\beta(T/T_c)C(\mathbf{r},\mathbf{r})$, where β is a function introduced and tabulated by Larkin which depends only on the reduced temperature T/T_c, and diverges as $T\to T_c$. In the presence of MT fluctuations, Eq. (2.42) for the fractional resistance change is modified to [Santhanam *et al.*, 1984]

$$\frac{\Delta R}{R} = \frac{3}{2}\frac{\Delta R}{R}(\ell_2,H) - [\beta+(1/2)]\frac{\Delta R}{R}(\ell_1,H). \qquad (2.50)$$

This expression is only valid for small magnetic fields $H<<(ck_BT/4De)\ln(T/T_c)$ and at temperatures where $\tau_\phi^{-1}<<\hbar k_BT[\ln(T/T_c)]$ [Lopes dos Santos and Abrahams, 1985]. The values of β used in this thesis were calculated from a polynomial fit to the tabulated theoretical values of Larkin [1980], as described in Appendix G of Santhanam [1985].

The MT fluctuations enhance the singlet contribution of weak localisation and the AAS Aharonov-Bohm effect. This enhancement can be quite large even at relatively high temperatures: at T=6 K, for example, for T_c= 1.25 K, $\beta\sim0.5$, i.e., equal

to the singlet localisation contribution. MT fluctuations should not contribute to conductance fluctuations and the hc/e Aharonov-Bohm effect. This is because calculations for the conductivity due to MT fluctuations involve energy exchange between the particle lines, which is not allowed in calculations for conduction fluctuations.

3. Experimental Techniques

3.1 Sample Fabrication

The samples studied in this thesis were made by thermal evaporation of thin films of Al, Ag or Au onto oxidised silicon substrates, and were measured at liquid He^4 temperatures, ~1.2-20 K. At these temperatures, ℓ_ϕ, which sets the length scale for quantum interference effects, is on the order of 1 μm; ℓ_T, which determines the dimensionality of electron-electron interactions, is smaller still (~0.15 μm). These two length scales set the requirements on the physical dimensions of the samples: In order to observe quantum transport in these samples, their size must be less than or comparable to ℓ_ϕ and, for conductance fluctuations, ℓ_T.

With ingenuity, one can make long narrow wires with widths of few tens of nanometres with optical techniques [Prober *et al.*, 1980; Feuer and Prober, 1981]. Making samples with more complicated geometries, however, is not simple. For such structures, electron beam lithography is preferred. Electron beam lithography not only provides the ability to make complex geometries, it also provides the flexibility of making modifications to these geometries with relative ease. This flexibility has proved important in our studies on the effect of measurement probes on short wires.

The fabrication process can be divided into three basic steps: Substrate patterning using electron beam lithography, deposition of the metal by thermal evaporation, and final "development" of the desired pattern by means of liftoff.

3.1.1 Substrate Patterning Using Electron-Beam Lithography

Appendix IV lists the important steps in the patterning of the small devices used in this thesis. The substrates are patterned using a bilayer resist technique [Mackie and Beaumont, 1985]. With this technique, features as small as 30 nm have been fabricated at Yale [Rooks *et al.*, 1987; Rooks, 1987]. The electron beam lithography facility used to fabricate the samples in this thesis was developed by Michael Rooks at Yale, who also fabricated some of the samples studied in this thesis. Details of the electron beam writing system, as well as the merits and demerits of different lithography processes, can be found in his Ph.D. thesis [Rooks, 1987].

The various steps in the fabrication process after the electron beam resist is spun on the wafer are shown schematically in Fig. 3.1. Contact pads are exposed through a chrome-on-quartz mask using a deep-ultraviolet (DUV) source, giving approximately 50 individual sample dies per wafer. Each 2.5 mm x 2.5 mm die (Fig. 3.2) has four 1 mm x 1 mm pads to which external measurement wires are to be connected. The pads terminate in a small 40 μm x 40 μm region in the centre of the die into which the device of interest is written by electron beam lithography. By these means, one avoids defining the large pad regions, where fine resolution is not required, with the time-consuming process of electron beam lithography.

Even on an exposure field of 40 μm x 40 μm defined by 1024 x 1024 pixels, each pixel is ~40 nm. In order to write finer features, the exposure field needs to be reduced. This is done by first writing an interim mask which extends the four pads of the DUV mask down to a field of 15 μm x 15 μm. The final sample is then defined in this field, where each pixel corresponds to ~15 nm. Writing two electron beam masks has also proved useful for making narrow wires with large 2D probes. In this

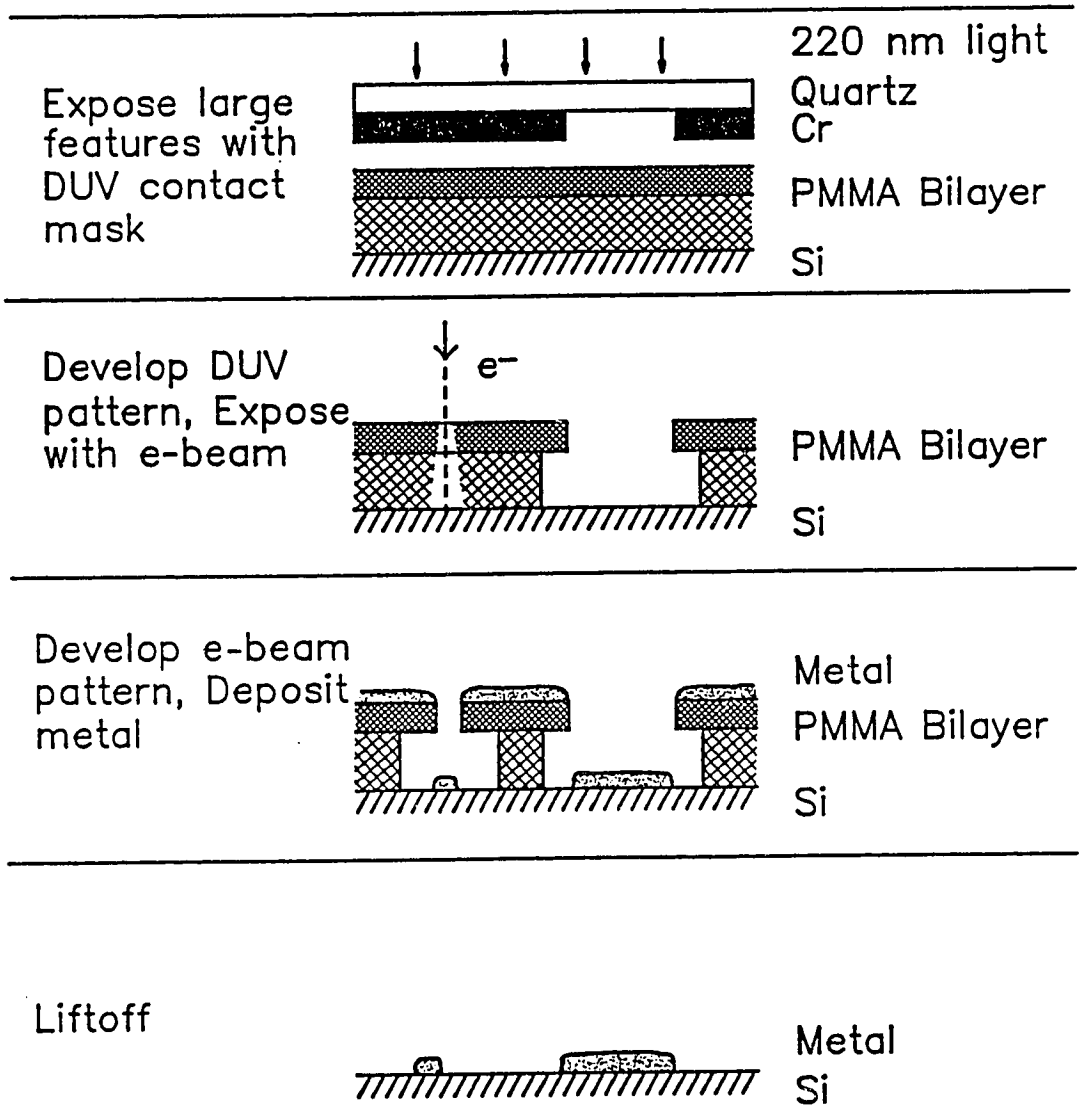

Figure 3.1. Fabrication steps in the hybrid DUV-electron beam process (From Rooks [1987]).

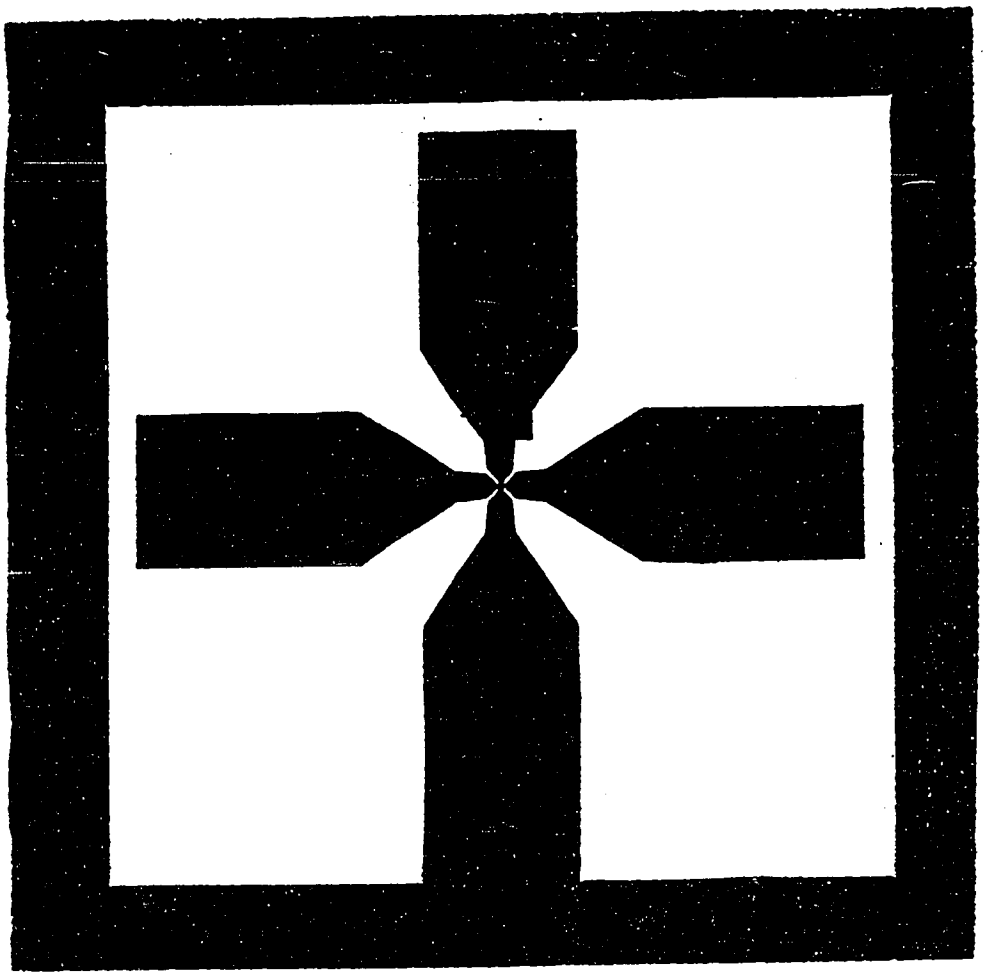

Figure 3.2. Mask used for DUV exposure of contact pads. Final area of the die is 2.5 mm x 2.5 mm. Note that three of the pads are shorted together to prevent blowout from electrostatic discharge. (From Rooks [1987].)

case, the entire sample except the narrow wire itself is written onto the 40 μm x 40 μm field; the narrow wire is then stitched in on a 15 μm x 15 μm field. One is thus able to achieve narrow linewidths for the wires. Figures 3.3 and 3.4 show scanning electron microscope (SEM) pictures of some samples that were actually measured.

3.1.2 Metal Deposition

Prior to deposition, the substrate is first cleaned in the vacuum chamber by an oxygen glow discharge. For the Al and Au evaporations, pure (99.999%) metal wire[1] is wound onto a tungsten filament and evaporated at a rate of 0.1-0.15 nm/sec in a Varian 3118 vacuum evaporator.[2] The Ag films are evaporated from 1-3 mm Ag shot in a Ta boat. The evaporations are initiated and terminated by a manually operated shutter, and the thickness of the film is determined using a quartz-crystal monitor from R.D. Mathis.[3] The material properties of the Al films are sensitive to the rate of evaporation and the chamber pressure during evaporation. Cleaner films, with lower $R_{\square}$, are obtained by evaporating at higher rates and lower chamber pressures. Material properties of the Ag and Au films are not as sensitive to evaporation parameters. To monitor the material properties of the metal wires and loops, a wide 2D film is always co-deposited along with the samples.

For the magnetic impurity studies, a very small amount (~0.01 atomic layers) of Co is evaporated on the surface of Ag films immediately after deposition of the Ag. Co was chosen because it is relatively resistant to oxidation. The Co source is in the

---

[1]from Alfa Products, Danvers, Massachusetts

[2]Varian Assoc., Palo Alto, California.

[3]R.D. Mathis Co., Long Beach, California.

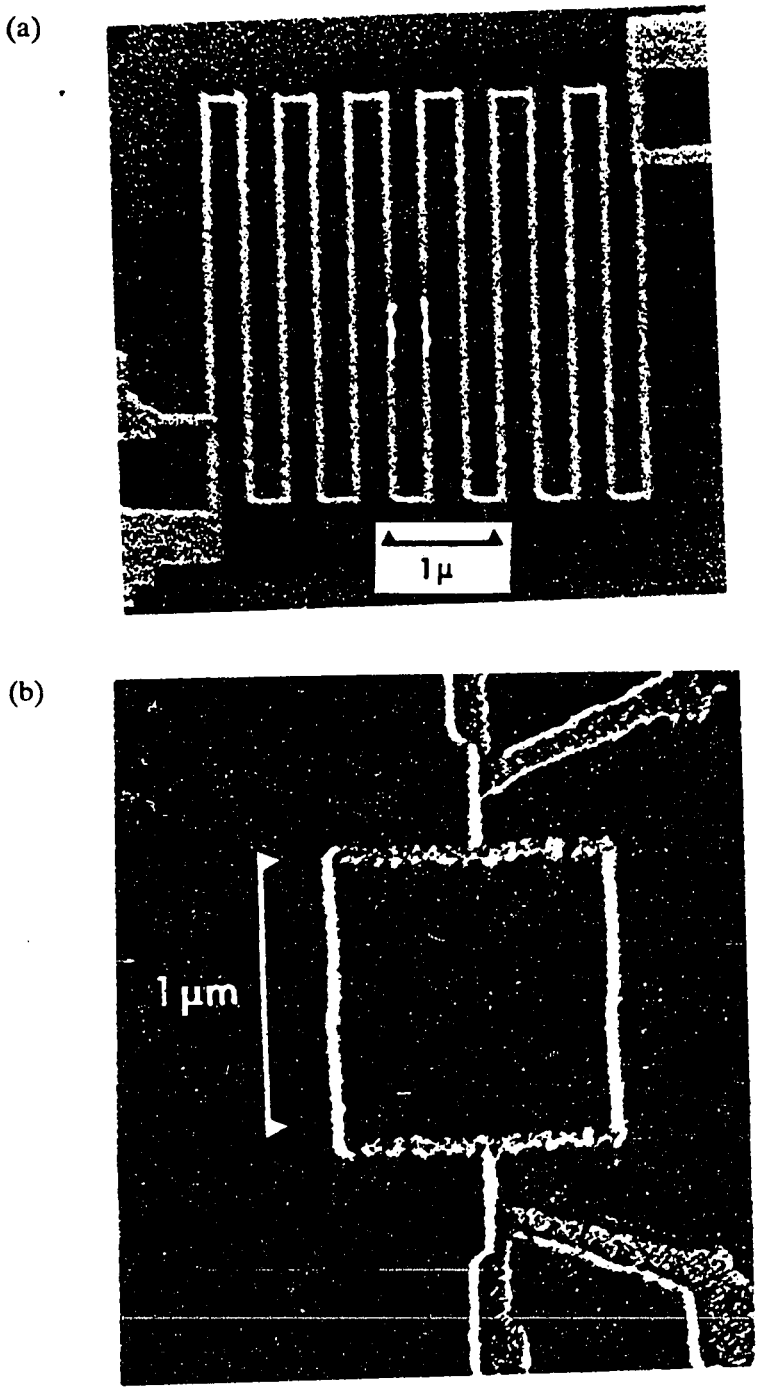

Figure 3.3. SEM micrographs of Ag samples (a). ~50 μm long wire. (b). ~ 1 μm square loop.

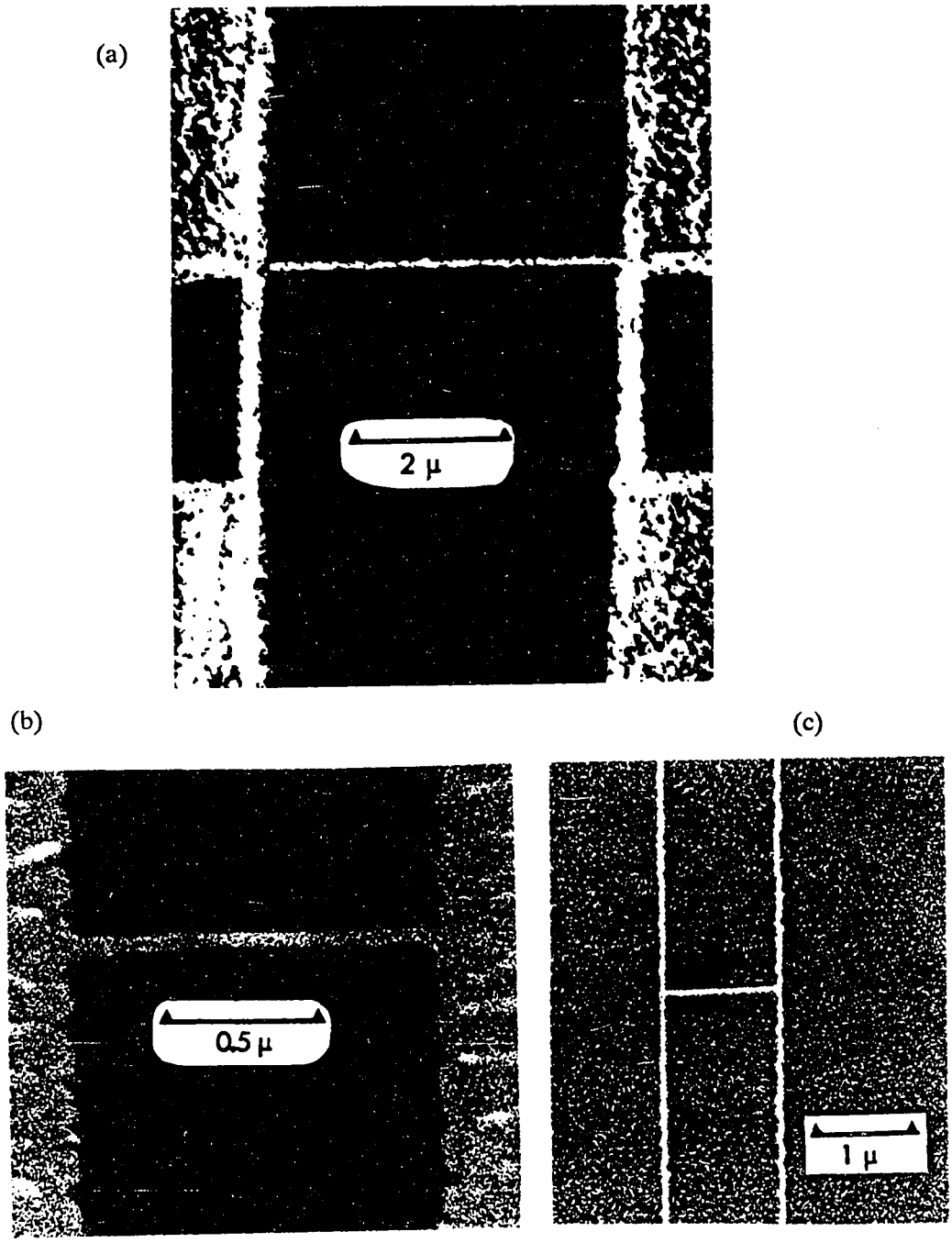

Figure 3.4. SEM micrographs of short wires with different measurement configurations. Small letters correspond to the caption of Fig. 2.6.

form of wire tightly wound on a tungsten filament. To evaporate such a small quantity of Co, the heater power to the tungsten filament is adjusted to give a steady rate of about 0.5-1.0 nm of Co in 15-20 minutes with the evaporation shutter closed. The shutter is then opened and Co evaporated onto the Ag films for 5-10 sec. In order to compare properties of samples with and without magnetic impurities, half the samples are covered by a second shutter during this last step.

3.1.3 Liftoff

After deposition, the unwanted metal is lifted off by dissolving the unexposed PMMA in acetone. For the wide 2D films, liftoff does not pose a problem. These films can be placed in acetone in an ultrasonic agitator, where the unwanted metal is removed in a matter of seconds. This procedure cannot be used for the 1D devices, as it removes parts of the device as well. Initially soaking the 1D devices in acetone for about 1 hour greatly facilitates removal of the unwanted metal. After the soak, acetone is squirted at the device with a wash bottle, or in especially tough cases, with a syringe. It should be noted that each of the metals used above has its own particular problems with regard to liftoff. Al has the tendency to "creep" over the resist edges, making liftoff difficult. Au does not stick well to the substrate, consequently, on soaking in acetone, the entire pattern will occasionally come off. The trick of putting down a thin layer of Cr to improve the adhesion of Au to the substrate cannot be employed, since it will likely modify the properties of the Au film. Adhesion for Au is improved by increasing the time the substrate is cleaned by oxygen glow discharge prior to deposition. Lastly, Ag films appear to be affected by acetone: Soaking in acetone for a few hours results in films which are pitted and

have high $R_{\square}$'s. After liftoff, all samples are stored at 77 K unless they are to be measured immediately. This is especially important for the Ag films, which degrade in air within a day.

Table 4.1 lists the relevant parameters of the short Ag wires, and Tables 5.1 and 5.2 list the relevant parameters of the Al, Ag and Au loops. Table 5.3 lists the additional samples that were measured, but which are not discussed in Chapters 4 and 5.

3.2 Sample Measurement

The samples were measured in a cryostat constructed by Bruce Dalrymple, which is described in detail in his thesis [Dalrymple, 1983]. The sample end of this cryostat consists of a short copper bar on which the sample, a calibrated germanium resistance thermometer[4] and a heater are mounted. The copper bar is in a vacuum can which is thermally isolated from the liquid helium bath into which the cryostat is dipped, except for 12 #36 copper wires for electrical connections to the sample, thermometer and heater. The weak thermal link provided by the copper wires results in the temperature of the copper sample block being a little higher than that of the helium bath: for example, if the bath is at 4.2 K, the temperature of the block is ~4.5 K. The weak thermal link allows one to vary the temperature of the copper block above the temperature of the bath. By pumping on the helium bath, temperatures in the range 2-20 K can be accessed. For lower temperatures, a small amount of helium transfer gas is introduced into the vacuum can to improve thermal contact between the copper block and the bath. In this way, temperatures as low as 1.2 K can be reached. The cryostat fits into the bore of an 80 kG NbTi superconducting magnet so

---

[4]Cryocal CR-1000, SN 6218, TRI Research, St. Paul, Minnesota.

that the magnetic field is perpendicular to the plane of the sample film. For the samples studied in this thesis, magnetic fields of up to 25 kG were used. This magnet may have a small remanent field on the order of a few tens of gauss (depending on the energisation history of the magnet) due to the trapping of flux in the magnet coils, so that there may be a finite magnetic field through the bore with no current flowing through the coils.

In the following paragraphs, we describe in detail the sample mounting procedure and the electronic apparatus used to measure the magnetoresistance.

3.2.1 Sample Mounting

The small devices, by virtue of their size, are extremely susceptible to blowout by atmospheric electrostatic discharge. In order to prevent their being destroyed by such a discharge, the four measurement pads connected to the samples are shorted at all times that the sample is not being measured. For some of the first samples, this was done immediately after fabrication by shorting all the pads with silver paint. Later samples were designed so that three of their pads were shorted on fabrication (Fig. 3.2). These connections are later scratched out with a sharp tool after the sample has been mounted on the cryostat. After mounting on the cryostat, the sample is kept shorted at all times (except during measurement) by means of a "shorting box" which shorts the four leads connected to the sample at the room temperature end of the cryostat. In addition, a humidifier is occasionally used during the dry winter months, when the samples are most susceptible to atmospheric electrostatic discharge. Other precautions, such as electrically grounding the person mounting the sample, are also employed. In spite of all these precautions, quite a few

samples were destroyed during mounting or measurement.

After scribing the wafer into individual dies, small amounts of indium are placed near the four contact pads of the die to be mounted, using a battery operated soldering iron. In the case of the Al samples, the indium can be placed directly on the contacts themselves. For Ag and Au samples, the indium tends to diffuse into the sample itself, as evidenced by the presence of a sharp rise in the resistance of the sample near the superconducting critical temperature or critical field of indium; thus, for these samples, the indium is placed on the oxidised substrate next to the pads. In most cases, the indium sticks well to the substrate. In the few cases it does not, the problem can be remedied by cleaning the area around the contacts with a small cotton-tipped swab dipped in isopropanol, and, in the case of Al, by scratching the surface of the contact pad lightly with the tip of the soldering iron. The sample is then mounted on the copper block with vacuum grease, and four #40 copper measurement leads from the cryostat are soldered to the indium on the substrate. Final contact to the pads for the Ag and Au samples is made by connecting the indium to the contact pads with fast drying silver paint. After the silver paint has dried, the contacts are tested by measuring their resistance. If they are found to be satisfactory, the shorts between the contact pads are carefully scratched out, and the sample can be measured.

3.2.2 Magnetoresistance Measurements

A schematic of the measurement apparatus is shown in Fig. 3.5. The electronic setup consists of a four-point ac resistance bridge, power supplies to energise the superconducting magnet, and a negative feedback temperature control unit. The

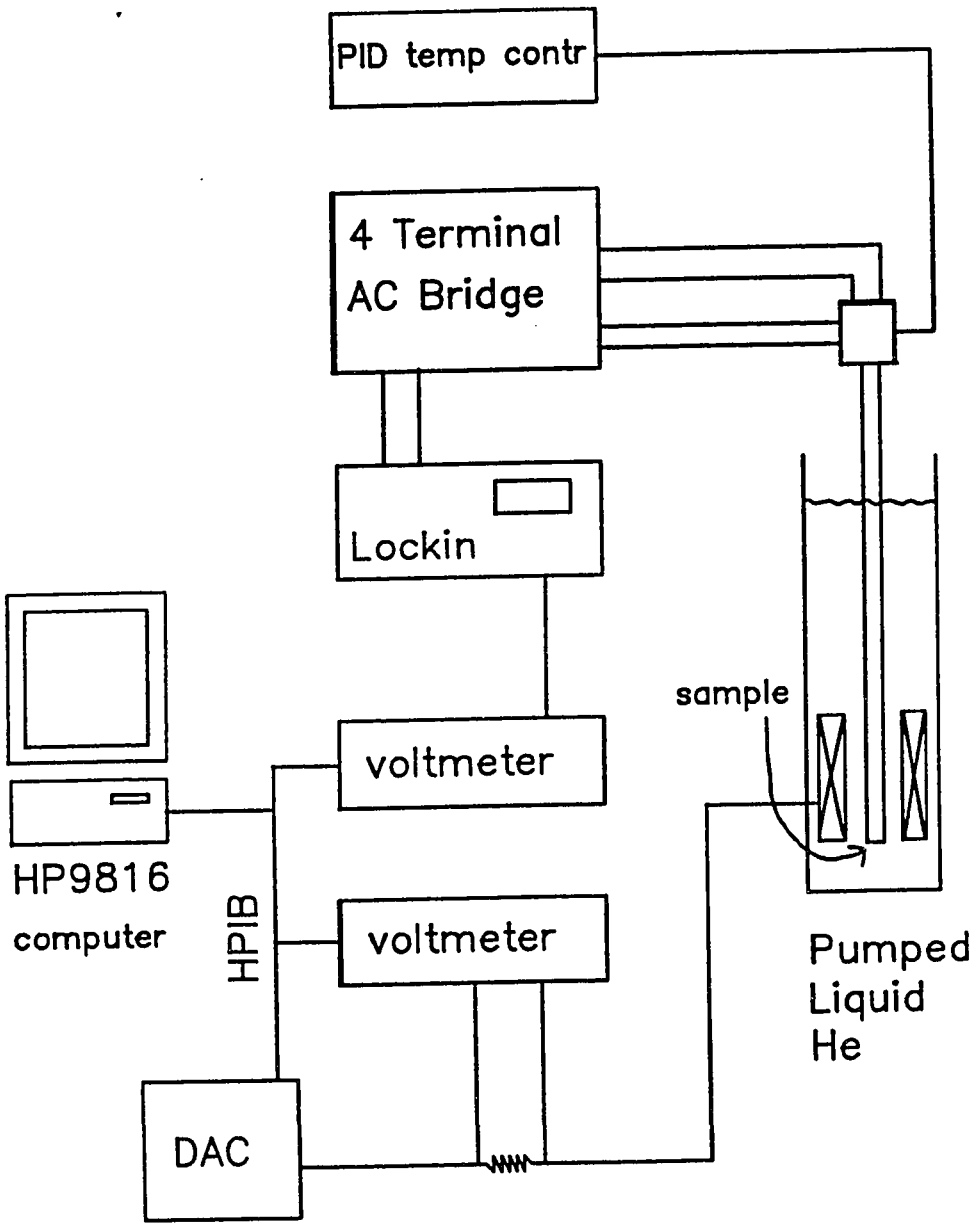

Figure 3.5. Schematic of the apparatus used for magnetoresistance measurements. (From Rooks [1987].)

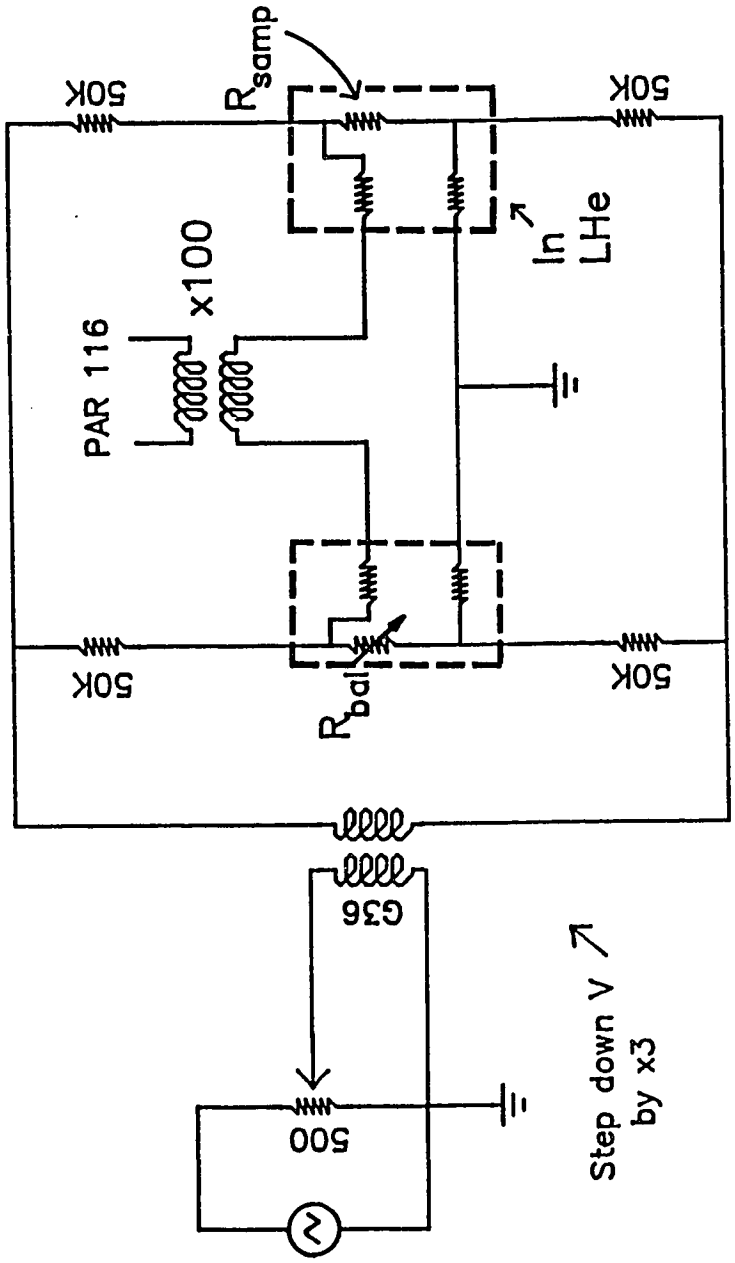

Figure 3.6. Schematic of the four-point bridge (from Rooks [1987]).

magnetic field is controlled by a computer, which also reads the output of the lock-in amplifier and the voltage across the magnet shunt resistor.

Four-Point AC Resistance Bridge

The circuit diagram of the four-point resistance bridge is shown in Fig. 3.6. This bridge was constructed at Yale by the author, and is a simplified version of the ac bridge designed by Adler and Jackson [1966] for measurements on tunnel junctions. The four arms of the bridge contain extremely stable 50 kΩ resistors[5] mounted together on a copper block which act as current sourcing resistors for the sample and the balance resistor.[6] For small bridge excitation voltages, the internal oscillator of the lock-in amplifier[7] is used. When larger excitation potentials are required, an external oscillator[8] is employed. The lock-in amplifier measures the potential difference between the V^+ probes of the sample and balance resistor. The V^- probes are connected together so that the lock-in amplifier sees only the difference in potential across the balance resistor and the sample. This also ensures that noise resistance seen by the lock-in is determined only by the sample, the balance resistor, and the leads connecting them. Since the sample is in liquid helium and the balance resistor at room temperature, the major contribution to the Johnson noise comes from the balance resistor. (The lead resistance is small.) The input impedance of the preamplifier[9] of the lock-in is 100 MΩ. To provide better impedance matching when

---

[5]Vishay Resistive Systems Group, Malvern, Pennsylvania.

[6]GenRad 1432-W Decade Resistor, General Radio Co., Concord, Massachusetts.

[7]PAR 126, Princeton Applied Research, Princeton, New Jersey.

[8]HP209A or HP239A, Hewlett Packard, Cupertino, California.

[9]PAR 116, Princeton Applied Research, Princeton, New Jersey.

measuring samples of small (~50 Ω) resistance, the internal transformer of the preamplifier is used. The optimum gain of this transformer for such input impedances is at a frequency of ~500 Hz; this frequency was used in all the experiments.

This simple ac bridge has proved to be remarkably reliable and easy to use. The sensitivity of the bridge is determined by the source Johnson noise and the noise of the lock-in amplifier. For a sample of resistance 50 Ω, with the lock-in output time constant at 1 sec and 12 dB/oct, the noise referred to the input of the lock-in is ~0.4 nV rms. With a typical current of 0.5 μA, changes in the resistance of 2 mΩ or a few parts in 10^5 can be measured. Sensitivities of a few parts in 10^6 can be achieved with higher currents or longer time constants. Joule heating of the sample, however, provides an upper limit to the current that can be used. In samples without magnetic scattering, the temperature of the electron gas can be measured by using the weak localisation correction as an electron gas thermometer [Santhanam, 1985].

If magnetic impurities are present, the weak localisation signal may not be large, or may not be strongly temperature dependent. In this case, other methods have to be employed. One method is to measure the off-null signal from the bridge at the most sensitive setting as the current through the sample is increased. If the sample is not being heated, by Ohm's law, a plot of the off-null voltage as a function of current throught the sample should be a straight line; at higher currents, the resistance of the sample changes as the electron gas is heated, and the relationship is no longer linear. The measuring current should therefore be chosen to be well within the linear region. This method will not work if the temperature dependence of the sample resistance is flat. In this case, one can rely on prior experience with similar samples without magnetic impurities. If all else fails, the current can be estimated by

calculation using known sample parameters. For long 1D wires, heating of the electron gas is determined by energy loss to phonons, while for shorter wires, heat conduction through the leads is most important. A simple energy in - energy out calculation will then indicate the appropriate measuring current to avoid self-heating [Wisnieff, 1987]. Note that at any current, some heating will always occur. How much heating is acceptable is determined by the sample being measured.

Temperature Control

Two different means of monitoring and controlling the temperature are employed. For quick measurements when controlling the temperature is not of importance, a dc current source built by Dalrymple [1983] is used. The current source box also provides power to the heater which can be controlled by means of a ten turn potentiometer. For more accurate temperature control, a home-made proportional-integral-differential (PID) feedback control unit is used to control power to the heater. The circuit diagram for this PID is shown in Fig. 3.7. The error signal input for the PID is provided by a four terminal ac bridge, similar in design to the bridge described above, operated at 27.5 Hz. At temperatures above 4.5 K, the PID alone is used to control the temperature. Below 4.5 K, the temperature of the bath is controlled to just below the desired temperature using a standard Walker pressure regulator, and the PID used for fine temperature control. One thus avoids using large amounts of heater power, resulting in lower helium loss and better temperature control in the presence of transfer gas. With the PID, the temperature can be controlled to better than 0.5 mK at the lowest temperatures.

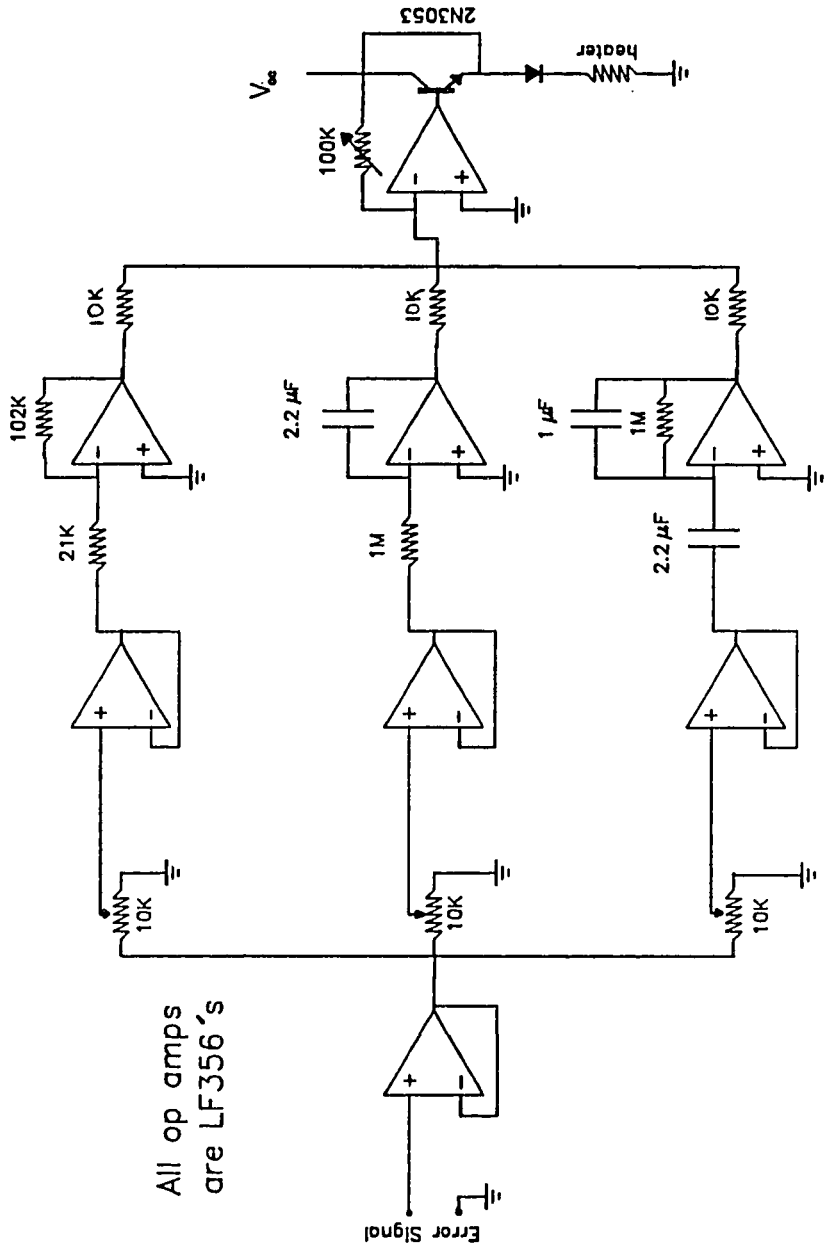

Figure 3.7. Schematic of the Proportional-Integral-Differential (PID) temperature control unit.

Magnet Control

The magnet protection and control circuitry is almost identical to the one used by Dalrymple [1983]. The magnetic field is proportional to the current flowing through the magnet (2.525 G/mA); the current is measured by measuring the voltage across a shunt resistor. Depending on the magnetic field range desired, shunt resistances of 0.5 Ω to 100 Ω are used. The current is provided by a power supply[10] under computer[11] control. The computer ramps the current through the magnet in steps, ensuring that the rate is low enough so that the charging voltage of the magnet is less than 1 volt.

The output of the lock-in and the magnet current are monitored by the computer through two voltmeters.[12] For magnetoresistance measurements, the computer steps the field through the field range specified by the operator; the output of the lock-in is converted into fractional resistance change and plotted in real time against the magnetic field. The computer also monitors the resistance of the thermometer. If the PID is being used, the computer monitors the error signal of the thermometer bridge; data taking is terminated and the magnet de-energised if the error signal becomes too large. This prevents damage to the magnet in the event of the helium level dropping below the magnet before the data run is complete.

3.3 Characterisation of Samples

For a meaningful comparison to theory, certain sample parameters need to be

---

[10]Hewlett Packard Model 6632A, 6282A or 6823A.

[11]Hewlett Packard Model 9816 or 9836.

[12]Hewlett Packard Model 3478A.

known. In this section, we describe these sample parameters and how they are determined.

Film Resistivity

The resistivity of the sample can be determined from a measurement of the sample resistance and a knowledge of the sample dimensions. The sample resistance is measured by the bridge described above. The sample film thickness is known to within 5% from the readings of the calibrated thickness monitor during deposition. For the large 2D films, the lateral dimensions are determined using a calibrated optical microscope. Usually, it is sufficient to measure the lateral dimensions once for a particular 2D mask. For 1D structures, a SEM is required. The 1D samples in this thesis were examined in a SEM after electrical measurements were completed. SEM micrographs give the lateral dimensions to ~10%. In addition, electrical measurements on the 1D samples provided a further check on sample dimensions. For the loops, the area of the loops can be accurately obtained from the period of oscillation of the Aharonov-Bohm effect. The width of the long wires can be obtained by fitting to the weak localisation magnetoresistance at the lowest temperature, where the spin-orbit scattering length is irrelevant. For both the loops and the wires, the dimensions obtained from such electrical measurements are in agreement with the SEM micrographs, and are usually more precise. This is particularly true for the Al samples, for which contrast in the SEM micrographs is poor.

The theoretical predictions of the preceding chapter are usually given in terms of the sheet resistance $R_{\square}$; this is related to the measured resistance R, sample length L and sample width W through the equation $R_{\square}=R(W/L)$. Ideally, one expects samples

that are co-deposited to have the same $R_\square$. In practice, it is found that the $R_\square$'s of co-deposited 2D films can differ by up to 50%. The largest difference in these studies was found in the Ag samples, where the 2D films routinely had lower $R_\square$'s than their co-deposited 1D wires. This may be the result of the effect of acetone on the Ag films: Since liftoff for the 2D films was much quicker, the 2D films were soaked in acetone for a much shorter period of time than their co-deposited 1D structures. For co-deposited 1D structures, the $R_\square$'s are the same to within 15%. Typical $R_\square$'s for the samples studied in this thesis were 1-5 Ω, corresponding to resistivities of ~5 μΩ-cm.

Diffusion Constant D

The diffusion constant D is determined by the elastic mean free path ℓ, $D=v_F\ell/d$, where d is the dimension of the sample with respect to ℓ. For most of the samples in this thesis, ℓ is shorter than the thickness of the film, so that d=3. (ℓ is always shorter than the width of the 1D wires.) In an ideal metal, ℓ is inversely proportional to the resistivity ρ; the product $\rho\ell$ is a constant. Thus, ℓ can be calculated from a knowledge of the $\rho\ell$ product and the measured resistivity of the sample ($\rho=R_\square t$, where t is the thickness of the film). For Ag, we use the value $\rho\ell=5.36\times10^{-12}$ Ω-cm^2 [Gershenzon *et al.*, 1982], while for Au we use the textbook value $\rho\ell=8.45\times10^{-12}$ Ω-cm^2 [Ashcroft and Mermin, 1976]. The $\rho\ell$ product for the Al films can be determined independently from the critical field slope dH_{c2}/dT, as described in Appendix F of Santhanam [1985]. We shall describe below the technique used to measure dH_{c2}/dT.

Superconducting Critical Temperature and Critical Field Slope

For the Al samples, the superconducting critical temperature T_c is an important parameter that determines the contribution of the Maki-Thompson fluctuations to the

conductivity above T_c through the Larkin parameter $\beta(T/T_c)$. We choose T_c to be the temperature at which the resistance of the sample is half its resistance in the normal state. To determine the critical field slope, the four point ac bridge is used in conjunction with the PID feedback control. The balance resistor is set at half the normal state resistance, and the off-null voltage of the bridge is fed into the error signal input of the PID. As the magnetic field through the sample is swept, the PID adjusts the temperature of the sample to maintain it at the midpoint of the superconducting transition. By reading the resistance of the thermometer, a plot of $T_c(H)$ vs. H can be obtained. Fitting Eq. (F.4) of Santhanam [1985] to this using a Simplex least squares routine [Caeci and Cacheris, 1984], one determines D, and from it, ℓ.

Analysis of Magnetoresistance Data

The quantum interference effects in our samples can be divided into two categories- sample-specific effects such as conductance fluctuations and the hc/e Aharonov-Bohm effect, and ensemble-averaged effects such as weak localisation and the AAS Aharonov-Bohm effect. Experimentally, this division is clearcut only in the case of the large 2D films and the long 1D wires, where the only significant contribution is weak localisation. For these samples, the low field MR data is fit to the appropriate weak localisation formula using a Simplex least squares routine [Caeci and Cacheris, 1984]. The fitting procedure for the long 1D wires is as follows. To precisely determine the width W, the MR data at the lowest temperature (usually 1.25 K) is first fit using ℓ_ϕ, ℓ_{so} and the width W as free parameters. Using this value of W and the measured values of the length and resistance (and T_c for the Al wires), the MR data is then fit with the two free parameters ℓ_ϕ and ℓ_{so} over the

temperature range where $\ell_\phi \sim \ell_{SO}$, usually 4-12 K. In this temperature region, the fit is most sensitive to both ℓ_ϕ and ℓ_{SO}. The average value of ℓ_{SO} over this temperature range is taken to be the spin-orbit length. With this value of ℓ_{SO}, the data is then re-fit over the entire temperature range with ℓ_ϕ as the only free parameter, obtaining ℓ_ϕ as a function of T. The procedure for the 2D films is similar.

In short wires and loops, both weak localisation and conductance fluctuations are present at low magnetic fields. The weak localisation component must then be separated from other contributions to the low field MR before it can be analysed. To do this, we use the fact that the weak localisation contribution to the MR is smooth and symmetric in the magnetic field, and the random conductance fluctuations are superposed on this smooth background. We therefore fit the appropriate weak localisation prediction to only the symmetric component of the low field MR using the same basic procedure for the long wires described above.

The predictions for conductance fluctuations and the hc/e Aharonov-Bohm effect are given in terms of field autocorrelation functions. Experimentally, autocorrelation functions can easily be computed from MR data. This correlation function is statistically meaningful only if the field range over which it is computed is large compared to the correlation field H_c defined in Chapter 2. The rms amplitude of the hc/e Aharonov-Bohm oscillations in a loop can also be determined from the field correlation function. An alternate method is to use the Fourier power spectrum of the MR data. The Fourier transform of the MR data will show a peak at a frequency 1/H, where H is the magnetic field corresponding to one flux quantum through the area of the loop. Since the arms of the loop have finite linewidth W, this peak is not a δ function, but has a width determined by W. Integrating the power spectrum

over this width gives the rms amplitude of the hc/e oscillations.

For both conductance fluctuations and the hc/e Aharonov-Bohm effect, checking the reproducibility of the data is important. Simple measurement noise is not reproducible; thus, taking data at the same temperature with the magnetic field swept in the opposite direction enables one to distinguish between features in the MR due to conductance fluctuations and features due to system noise. This has been done wherever possible in our experiments. However, samples may on occasion "switch," i.e., their resistance may jump in an irreproducible time-dependent manner. Such switching is thought to be due to the movement of impurities within the sample [Feng *et al.*, 1986]. The MR after such a switching event will usually not reproduce data taken before the event, even if the voltage offset of the lock-in amplifier is employed to bring the voltage back to the value it had before the switching event. The frequency of such switching events for the samples in this thesis varied from once every $\sim$15 minutes to less than once every few hours.

4. Experimental Results: Effect of Measurement Probes on Quantum Interference in Short Wires

In this chapter, we shall describe the experimental investigations into the effect of measurement probes on quantum interference in short wires. Thanks to electron-beam lithography, we can fabricate samples with a variety of measurement probe configurations, enabling us to test directly the theoretical predictions of Chapter 2. Our goal is to not only obtain a good qualitative understanding of the effects of measurement probes, but also a detailed *quantitative* agreement of experiment with theory. To do this, we need to be able to accurately determine ℓ_ϕ and ℓ_{so} for our samples. These parameters can be obtained by measuring the weak localisation correction in co-deposited long wires. Previous studies [Wind *et al.*, 1986] on long 1D metal wires have shown that the values of ℓ_ϕ inferred from fits to the weak localisation MR of long wires agree remarkably well with theoretical predictions. We shall briefly review these studies in the latter half of the next section.

The samples in this study were made of Ag and were fabricated in the measurement configurations depicted schematically in Fig. 4.1. To test the dependence on the length of the sample, samples of two different lengths (~1.3 μm and ~4.9 μm) were measured in each of the two configurations. Table 4.1 lists the material parameters of the short wires we measured, along with data for the co-deposited long wires and 2D films. In order to keep the material parameters for all samples the same, we attempted to fabricate all the samples in a single deposition. However, we were unable to measure the ~4.9 μm wire with wide leads (Fig. 4.1b) of this batch;

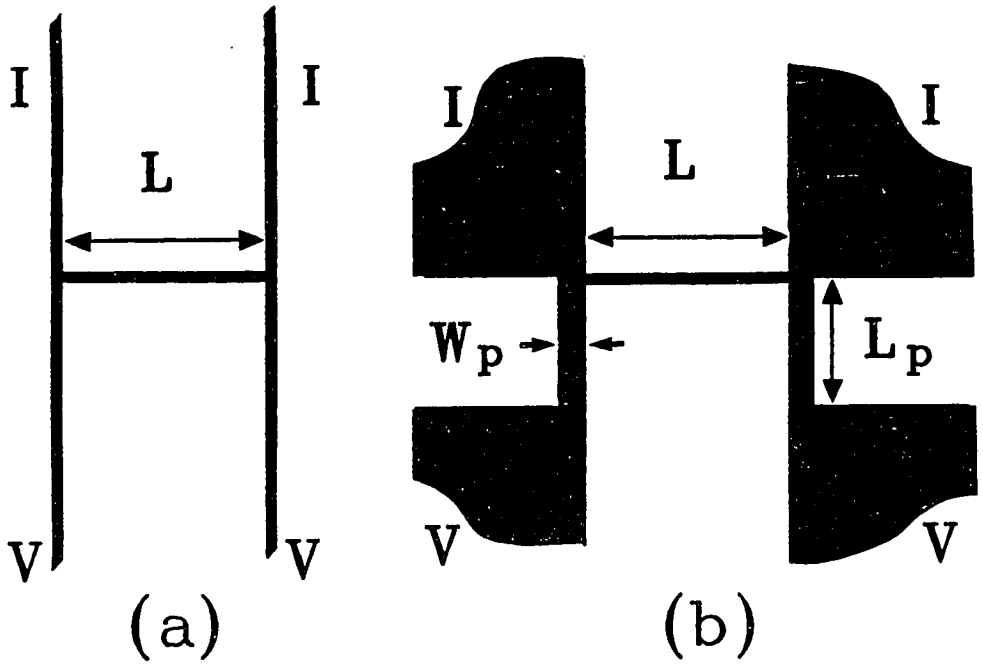

Figure 4.1. Schematic of probe geometry of short wires: (a). Short wire, length L, with narrow probes. (b) Short wire with wide probes; L_p~3μm, W_p~0.3 μm.

Sample	$R_\square$ (Ω)	L (μm)	W (nm)	ℓ (nm)	D (cm^2/sec)	ℓ_{so} (μm)
RX1	1.41	1.36	42	19	88	0.41
RX5	1.41	1.30	31	19	88	0.43
RX22	2.23	4.94	30	12	56	0.30
RX3	1.40	52.0	35	19	89	0.39
RX2D	0.90	---2D film---		30	139	0.58
RX28	1.14	4.76	60	23	105	0.65
RX27	1.21	53.7	54	22	102	0.51
RU20	1.31	2.55	30	20	95	0.44
RU26	1.32	1.25	40	20	94	0.56
RU21	1.35	53.4	40	20	92	0.49
RU2D	1.00	---2D film---		27	125	0.56

Co-deposited samples are grouped together.

Film thickness is 20 nm for all samples.

Table 4.1. Sample parameters for narrow Ag wires.

this sample was fabricated in a separate run. Two wires measured earlier are also included in Table 4.1. One (Sample RU20) is actually an Ag loop with one of the arms of the loop broken. The other is ~1 μm wire fabricated in the configuration of Fig. 2.6b, i.e., a wire with only 2D probes. In each of the fabrication runs, a long 1D wire was co-deposited as a control sample. All wires were measured in a four-terminal arrangement, i.e., the measuring current was introduced through two measurement probes and the corresponding voltage measured across the remaining two probes. This ensured that the voltage drop across the measurement probes themselves was not directly measured; thus, any influence of the measurement probes was only through their effect on the section of the sample between the two voltage probes.

We shall begin our description of the experiments by a look at the weak localisation data for the co-deposited long 1D wires and 2D films, and the determination of ℓ_ϕ from the weak localisation MR of the long wires. As pointed out in Chapter 2, data for these systems are not complicated by the effects of measurement probes, and will therefore serve to illustrate some of the general points about weak localisation made in that chapter. They will also serve as an appropriate reference point with which to compare the MR of short wires with measurement probes.

4.1 Weak Localisation in Long 1D Wires and 2D Films

4.1.1 Magnetoresistance

Figure 4.2a shows the magnetoresistance $\delta R/R$ (defined by Eq. (2.25)) of Sample RX3, a long Ag wire, at 2.0 K, along with a theoretical fit to the weak localisation theory. The MR is positive in sign, indicating the presence of spin-orbit scattering.

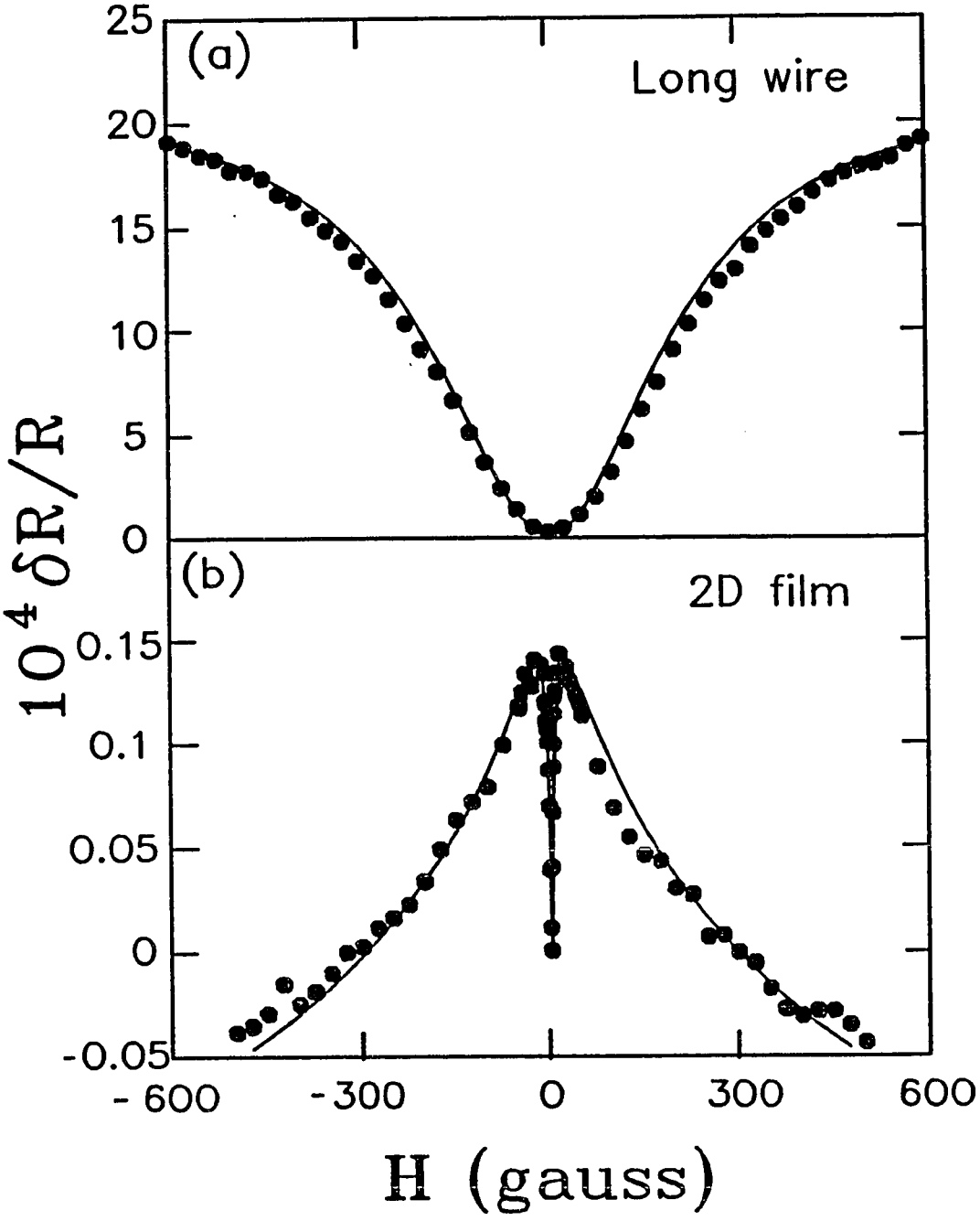

Figure 4.2. Weak localisation magnetoresistance of a long 1D wire and 2D film at 2.0 K. Circles, data; solid lines, fit to weak localisation theory. (a). Long 1D wire, Sample RX3; $\ell_\phi = 1.9$ μm, $\ell_{so} = 0.39$ μm. (b). 2D film, Sample RX2D; $\ell_{\phi 2D} = 3.61$ μm, $\ell_{so} = 0.58$ μm.

Accordingly, we have fit the data to the full theory including spin-orbit scattering, Eq. (2.42), with $\Delta R/R$ given by the long wire formula, Eq. (2.14). The magnitude of the weak localisation correction increases with ℓ_ϕ as the temperature is decreased. For a wire of finite length in the absence of magnetic scattering, we should expect the magnitude to continue increasing as the temperature is reduced until ℓ_ϕ is comparable to the sample size, ~50 μm. For a real sample, however, it is more likely that the presence of magnetic impurities will limit the phase breaking length, leading to a saturation in the amplitude of the MR as the temperature is lowered. In the long Ag wires described in this chapter, we do not see a saturation in the MR to the lowest temperature measured, 1.25 K, leading us to conclude that the magnetic scattering length ℓ_s is much longer than ℓ_ϕ at this temperature, ~3 μm. We therefore do not consider scattering by magnetic impurities for the samples in this chapter.

With an eye to some of the data for short wires with 2D measurement probes to be discussed later, we show, in Figure 4.2b, the MR at 2.0 K for an Ag 2D film co-deposited with the long wire discussed above, along with a fit to the 2D weak localisation formula, Eq. (2.27). Again, spin-orbit scattering leads to a positive MR at low fields, but the shape of the MR curves for the 2D film is distinctly different from the shape of the 1D MR curves. Note in particular the extremely sharp rise near zero magnetic field, which is absent in the MR of the 1D wire. We shall see later in this chapter that a similar sharp rise in the MR of small 1D wires signifies the presence of 2D measurement probes. Note also that the MR for the 2D film at the lowest temperatures is about two orders of magnitude smaller than the MR for a 1D wire. We shall return to this point when we discuss the MR of short wires with large 2D probes.

4.1.2 Electron Phase Breaking Lengths

The theory fits for both the long wire and the 2D film in Fig. 4.2 are excellent, indicating that the corresponding formulae provide a good description of weak localisation in these samples. (The fitting procedure has been described in detail in the last section of the Chapter 3.) The fits enable us to infer ℓ_ϕ as a function of temperature. Since ℓ_ϕ is an important parameter in the theory of weak localisation, we briefly review earlier work on similar long Ag and Al 1D wires [Wind *et al.*, 1986]. The long wires in this earlier study were prepared using the same electron-beam mask and fabrication procedure described in Chapter 3, so we can expect them to have properties similar to the wires in the present study.

The theoretical predictions for electron dephasing in Chapter 2 are given in terms of the dephasing rate τ_ϕ^{-1}, which is related to ℓ_ϕ through the equation $\tau_\phi^{-1} = D/\ell_\phi^2$. This rate is a sum of the electron-electron scattering rate and the electron-phonon scattering rate (Eq. (2.40)). The electron-phonon scattering rate in our samples goes as T^3 [see Chapter 2]. The temperature dependence of the electron-electron rate is determined by the effective dimensionality of the wire. This is set by the thermal diffusion length $\ell_T=(\hbar D/k_B T)^{1/2}$. When $\ell_T<W$, the electron-electron scattering rate is two-dimensional, whereas when $\ell_T>W$, the scattering rate is one-dimensional. As discussed in Chapter 2, there are two different predictions in 1D for the dephasing rate; one is the quasiparticle rate, given by Eq. (2.35), and the other is the AAK prediction for the Nyquist rate, Eq. (2.39). Wind *et al.* [1986] set out to determine which of these two rates was the relevant one for weak localisation. Figure 4.3 shows the phase breaking rate they obtained as a function of T for a number of different Al and Ag wires with different widths. The solid lines are least

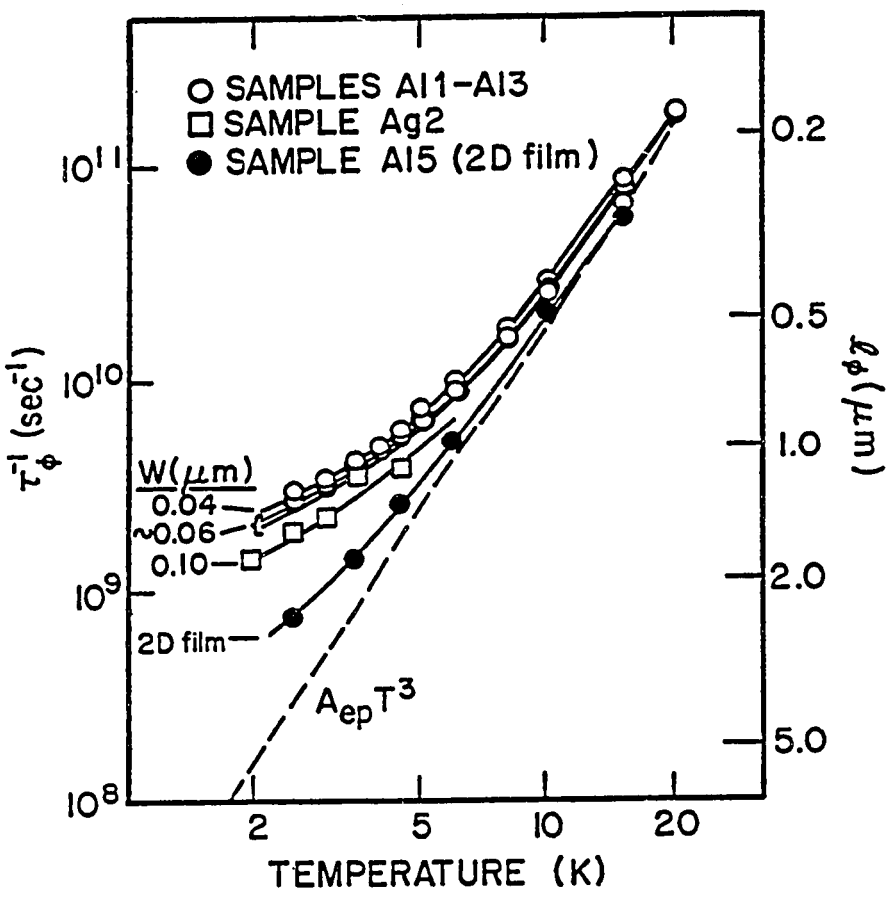

Figure 4.3. Phase breaking rate τ_ϕ^{-1} as a function of temperature for long Ag and Al wires. Solid lines are fits to the form $A_{2/3}T^{2/3} + A_3T^3$. From Wind *et al.* [1986].

squares fits to the equation

$$\tau_\phi^{-1} = \tau_N^{-1} + \tau_{ep}^{-1} = A_{2/3}T^{2/3} + A_3T^3, \qquad (5.1)$$

where $A_{2/3}$ is defined in Eq. (2.39). The fits are excellent, and the values of $A_{2/3}$ they obtained from these fits are within 15% of the values predicted by Eq. (2.39). Fits to a temperature dependence of $T^{1/2}$ for the electron-electron rate are also good, but the coefficient of the temperature dependent term obtained from these fits is more than two orders of magnitude larger than that predicted by Eq. (2.35). This shows conclusively that the relevant rate for weak localisation in 1D metals is the Nyquist rate given by Eq. (2.39). Details of these experiments on long wires can be found in the thesis of Wind [1987].

For the wires in our study, $\ell_T \sim 0.2\ \mu m/T^{1/2}$, making them 1D with respect to electron-electron scattering up to ~8 K. Fits to Eq. (5.1) of the rate inferred from the weak localisation MR of our long wires yield values of $A_{2/3}$ which are within 10% of the theoretical values. We are therefore confident that the values of ℓ_ϕ we infer from the long wires are reliable. ℓ_ϕ's for the 2D films are obtained in the same manner, and are consistent with previous studies [Santhanam, 1985].

4.2 Magnetoresistance of Mesoscopic Samples: General Features

Having seen MR curves for long 1D wires and 2D films, we shall now point out some particular characteristics of the MR of mesoscopic samples. In the hopes of making the following discussion clearer to the reader, we have organised in Table 4.2 the samples listed in Table 4.1 according to their measurement probe configuration. We shall refer to short wires with the measurement probe configuration of Fig. 4.1a as wires with "narrow probes," and short wires with the

Sample	Probe configuration	L (μm)	ℓ_ϕ at 1.25 K (μm)
RX5	Narrow probes	1.30	2.34
RX22	Narrow probes	4.94	2.34
RU20	Narrow probes*	2.55	2.36
RX1	Wide probes	1.36	2.34
RX28	Wide probes	4.76	2.93
RU26	2D probes only	1.25	2.36
RU21	Long wire	53.4	2.36
RX3	Long wire	52.0	2.34
RX27	Long wire	53.7	2.93

*Single loop with one arm not continuous.

Narrow probe configuration corresponds to Fig. 4.1a, wide probe configuration to Fig. 4.1b. Sample RU26 was fabricated in the probe configuration of Fig. 2.6b.

Values of ℓ_ϕ are for the co-deposited long wires.

Table 4.2. Probe geometry of narrow Ag wires.

measurement configuration of Fig. 4.1b as wires with "wide probes." Figure 4.4 shows the MR at 4.6 K of Sample RU20, a sample with narrow probes, over the field range 0-25 kG. From 0-2.5 kG, the MR is smooth, and corresponds to the weak localisation correction. Above 2.5 kG, however, the MR is random in the magnetic field. This is the contribution of the aperiodic conductance fluctuations, which are ubiquitous in samples of this size. These data from this sample are unusual; for most samples, the demarcation between weak localisation MR and conductance fluctuation MR is not so clearcut.

We found that the reproducibility of the fluctuation MR varied with a number of parameters. If some of the measuring parameters such as temperature or measuring current were changed between measurements, the data obtained in a second measurement could not be guaranteed to reproduce the data in the first measurement, even if all measurement parameters in both measurements were the same. In addition, the MR data was usually not reproducible if the resistance of the sample suddenly "switched." Figure 4.5 shows two such switching events in the low field MR of Sample RX5, the $\sim$1.3 μm wire with narrow probes; in this case, one event raises the resistance and the other reduces it by the same amount. These switching events are believed to be caused by the movement of impurity atoms in the sample [Feng *et al.*, 1986]. The two switching events in Fig. 4.5 are presumably due to an impurity moving from one position to another, and then back again. The time between the two switching events in Fig. 4.5 was approximately 15 minutes. We have found this time to be dependent on the temperature and measurement parameters, as well as the specific sample being measured. Some of the small samples we have studied switched quite frequently; others did not switch over measurement times of hours. The

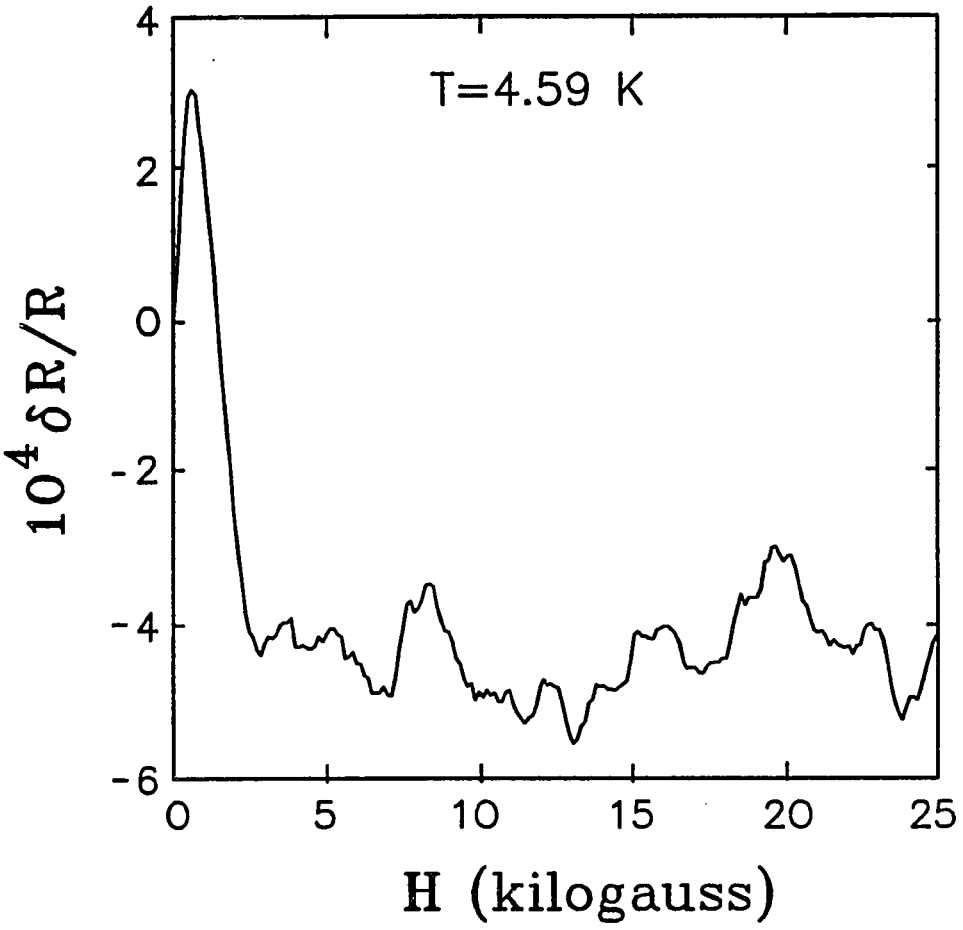

Figure 4.4. Magnetoresistance of Sample RU20, ~2.55 μm wire with narrow probes, at 4.6 K. The smooth weak localisation contribution changes to the aperiodic conductance fluctuations at ~2500 G.

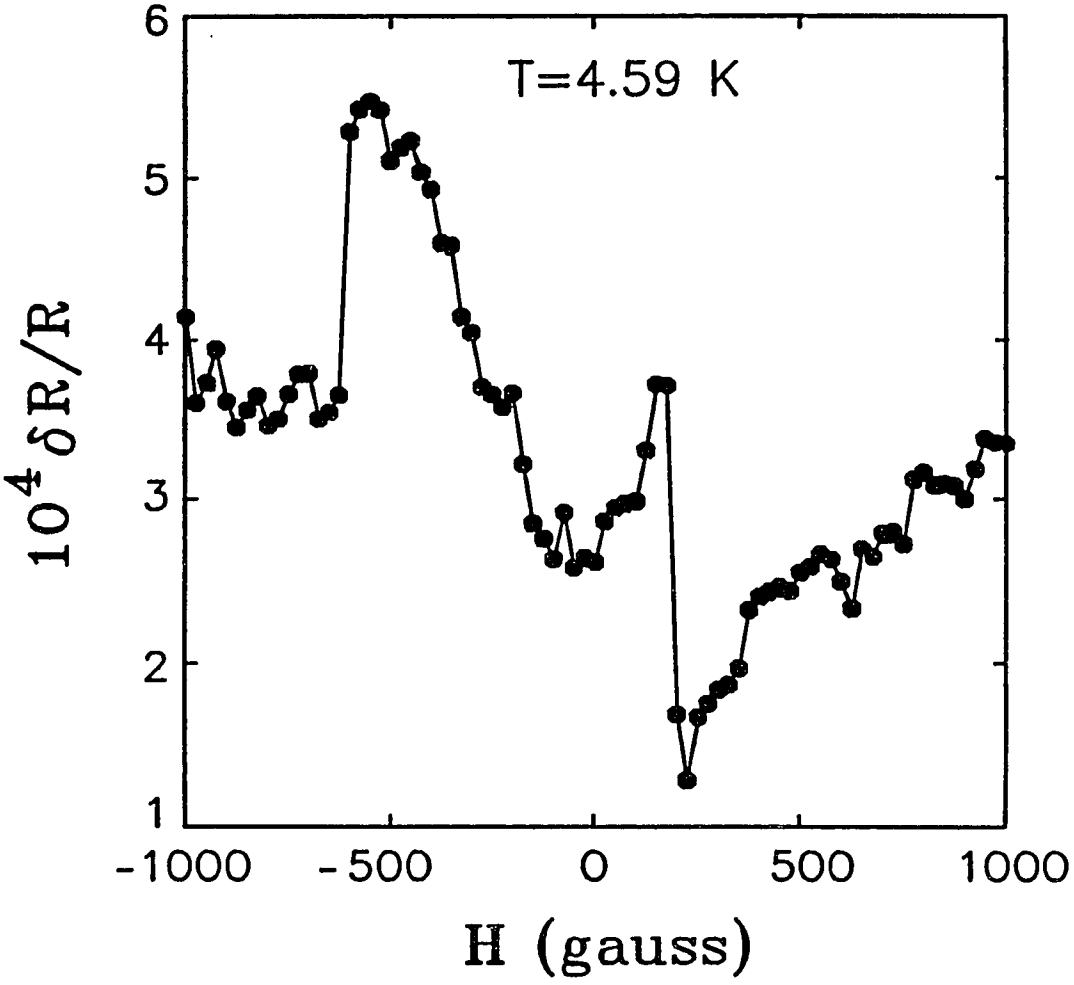

Figure 4.5. Magnetoresistance of Sample RX5, 1.3 μm wire with narrow probes, showing two switching events. One event occurs at ~-600 G, the other at ~200 G.

switching phenomenon was restricted to samples of dimension comparable to ℓ_ϕ; we did not see it in long 1D wires or 2D films.

Figure 4.6, which shows the low field MR at 4.0 K of Sample RX5, a ~1.3 μm wire with narrow probes, demonstrates another interesting property of the MR of mesoscopic samples. The sign of the MR of Sample RX5, like the sign of the MR of its co-deposited long wire, Sample RX3, is positive at low fields due to the presence of spin-orbit scattering. Unlike the MR for the long wire, however, the MR in Fig. 4.6 is distinctly asymmetric with respect to the magnetic field. This asymmetry is due neither to a weak localisation contribution, which must be symmetric, nor to an antisymmetric Hall contribution- it can be seen that subtraction of a component linear in the magnetic field will not lead to a symmetric MR. It is due instead to conductance fluctuations, which contribute a random component to the antisymmetric part of the MR.

For analysing the weak localisation contribution of short wires, we need to isolate the symmetric contribution. Accordingly, we fit the weak localisation theory to only the symmetric component of the MR. This component still contains contributions from conductance fluctuations which introduce some uncertainty in our analysis of weak localisation. These conductance fluctuations appear as a random signal superposed on the smooth weak localisation background. We wish to fit the theory to only the weak localisation contribution. This is best done by fitting to the average low field background MR of the sample.

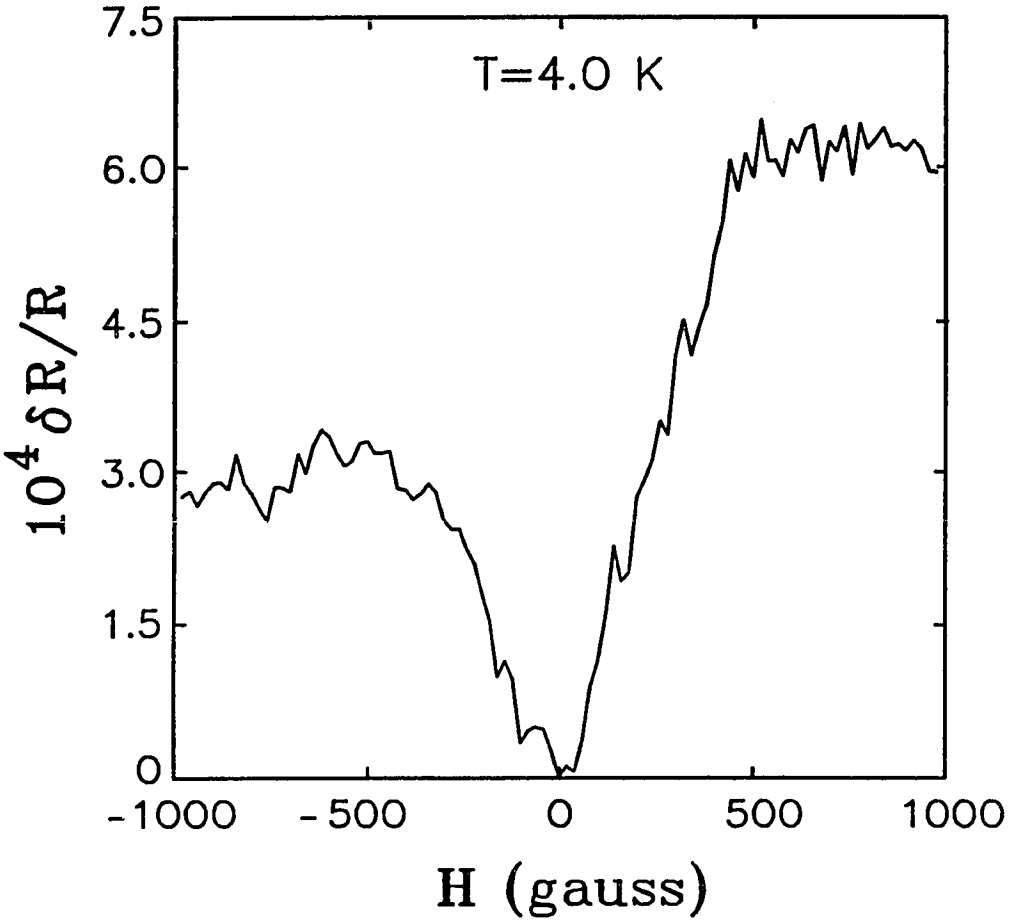

Figure 4.6. Asymmetric low field magnetoresistance of Sample RX5, a 1.30 μm wire with narrow probes, at 4.0 K.

4.3 Weak Localisation in Short Wires: Effect of Measurement Probes

4.3.1 Low Field Magnetoresistance

Now that we have taken a look at some of the general features of the MR of long and short metal wires, we are ready to examine the effect of different measurement probe configurations on the MR of short wires. In order to compare the short and long wires, we rewrite the long wire formula, Eq. (2.14) as

$$\frac{\Delta R(H)}{R} = \frac{R_\square}{(\pi\hbar/e^2)}\,\frac{1}{\alpha(H)}. \qquad (5.2)$$

The short wire limit ($L<<\ell_\phi$) of Eq. (2.22) can be written as

$$\frac{\Delta R(H)}{R} = \frac{R_\square}{(\pi\hbar/e^2)}\,\frac{1}{\eta(H)}. \qquad (5.3)$$

Here α and η have been written as functions of H to emphasise the possibility of a different functional dependence on H; $\alpha = W/\ell_\phi$ is a characteristic of the wire itself, and η is dependent on the probes alone.

Figure 4.7 shows the MR of the $L = \sim 1.3$ μm wires, Samples RX5 (narrow probes) and RX1 (wide probes), and their co-deposited long wire, RX3. At 1.25 K, ℓ_ϕ determined from the MR of the long wire is 2.39 μm, so that we are in the limit $L<\ell_\phi$ for the short wires. The magnitude of the MR of both short wires is reduced compared to that of the long wire; the MR of the short wire with narrow probes is about half that of the long wire, and the MR of the short wire with wide probes is less than a tenth that of the long wire.

From Eqs. (5.2) and (5.3), we expect the MR of a short wire to be reduced in comparison to that of the corresponding long wire if $\eta>\alpha$, as is the case for all our short wires. For the short wire with two narrow probes of width W on either end,

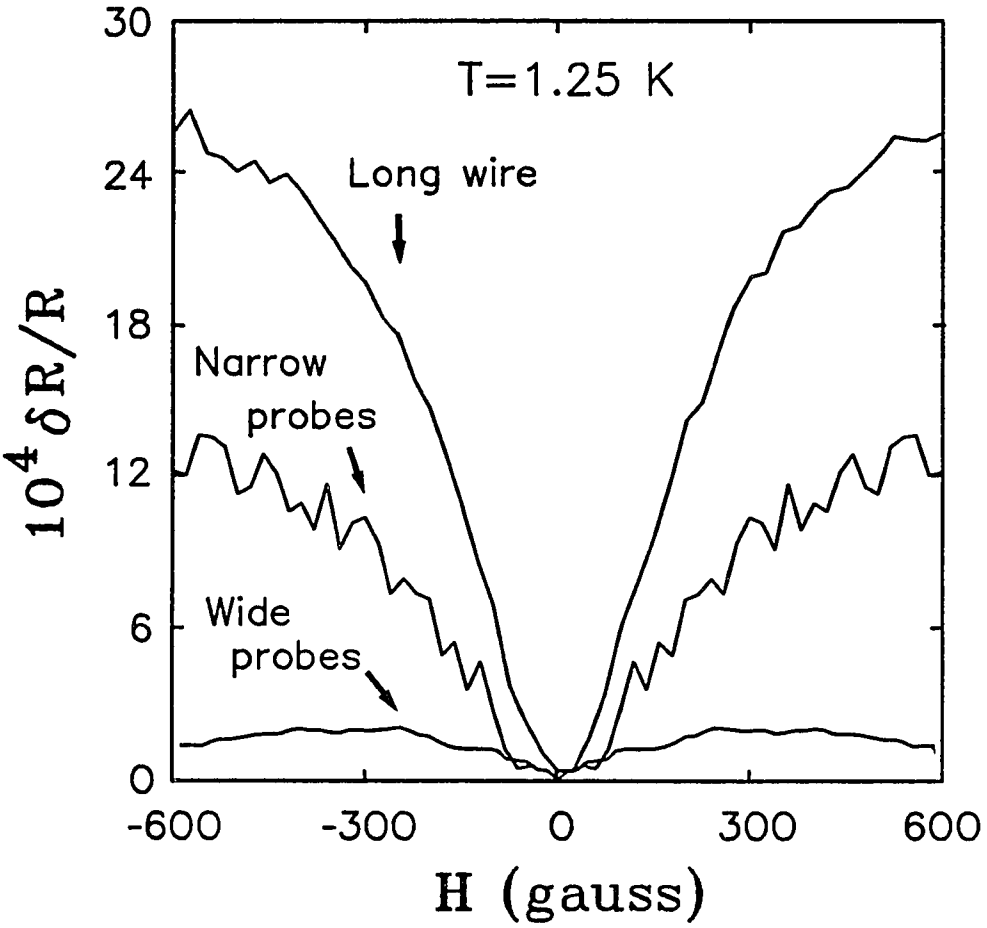

Figure 4.7. Symmetric component of the magnetoresistance of the L~1.3 μm wires at 1.25 K, Samples RX1 and RX5, along with data for their co-deposited long wire, Sample RX3. Long wire, RX3; short wire with narrow probes, RX5; short wire with wide probes, RX1.

$\eta=2\alpha$, so that the MR should be reduced by a factor of $\eta/\alpha=2$. This is precisely what is seen in Fig. 4.7. For the short wire with wide probes, η has contributions from both the 2D probes and the 1D probes of Fig. 4.1, $\eta=\eta_1+\eta_2$, where $\eta_1=(\pi/2)/\ln(2\ell_{\phi 2D}/\ell)$ is the contribution of the 2D probes, and $\eta_2=W_p/\ell_\phi$ is the contribution of the 1D probes. With W=42 nm, W_p=0.33 μm, ℓ=20 nm and $\ell_{\phi 2D}$= ~4.5 μm for RX1, η_1/α=14.5 and η_2/α=7.9, corresponding to an expected reduction by a factor of ~22. Given that experimentally we are not strictly in the limit $L<<\ell_\phi$, and that we have not taken the strong field dependence of η_1 into account, this is in fairly good agreement with experiment.

At higher temperatures, where $L>>\ell_\phi$, we expect the magnitude of the MR of all three wires to be approximately the same. Figure 4.8 shows data for the same three wires at 15 K, where ℓ_ϕ=0.29 μm. All three curves are of the same magnitude.

We now turn to another striking effect of the probes on weak localisation in short wires. Figure 4.9 shows the symmetrised low field MR of Sample RX1, the ~1.3 μm short wire with wide probes at 3.5 K. The phase-breaking length at this temperature, as determined from the co-deposited long wire, is 1.32 μm, so that $L/\ell_\phi\sim1$. Note the sharp rise in the MR near zero field. We also show a fit to the weak localisation formula appropriate to the geometry of RX1, Eq. (2.22), with η_1 given by Eq. (2.26). This fit accounts nicely for the sharp rise in the MR. We have seen a similar sharp rise earlier in the MR of a 2D Ag film (Fig. 4.2b). Indeed, this feature in the MR of the short wire is due to the influence of the 2D probes. For comparison, we show the best fit to Eq. (2.24), the formula appropriate for a short wire with four narrow leads. By adjusting the value of ℓ_ϕ in this formula, we can account for the reduced magnitude of the MR of RX1, but we cannot fit the

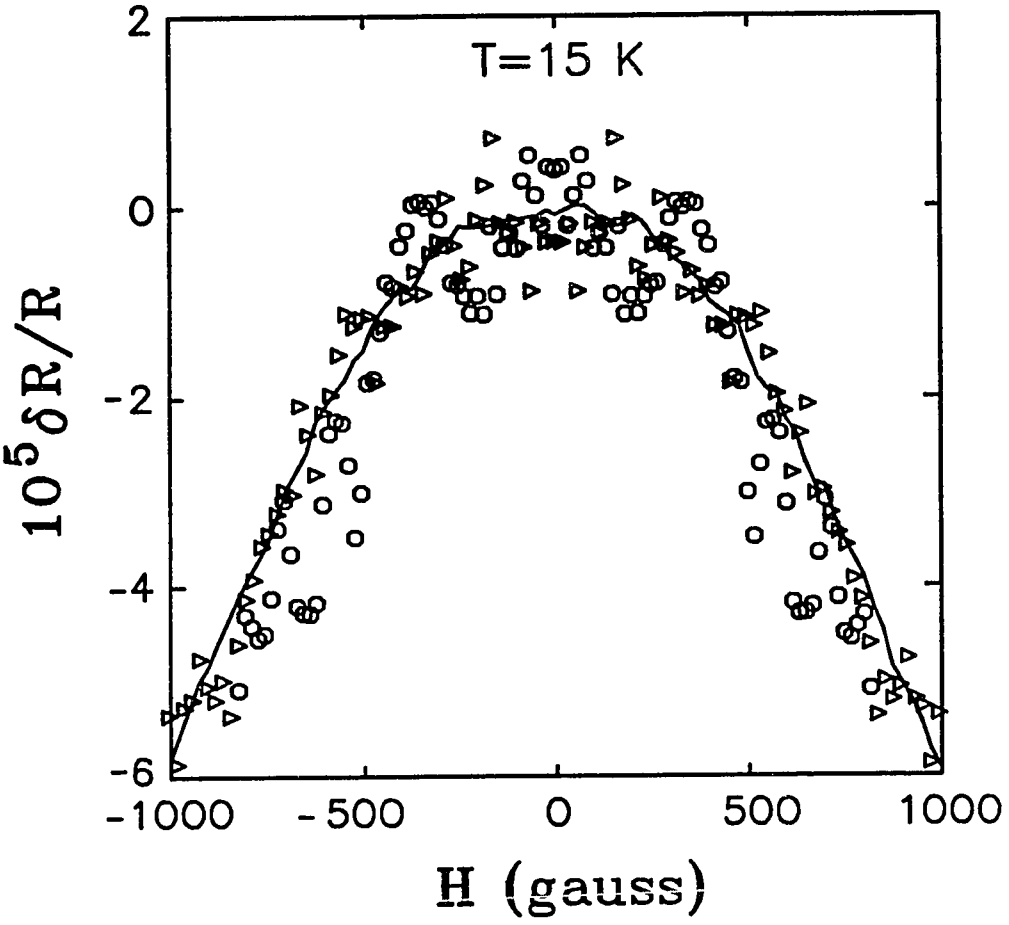

Figure 4.8. Magnetoresistance of the same three wires in Fig. 4.7 at 15 K. Solid line, long wire, RX3; triangles, short wire with narrow probes, RX5; circles, short wire with wide probes, RX1.

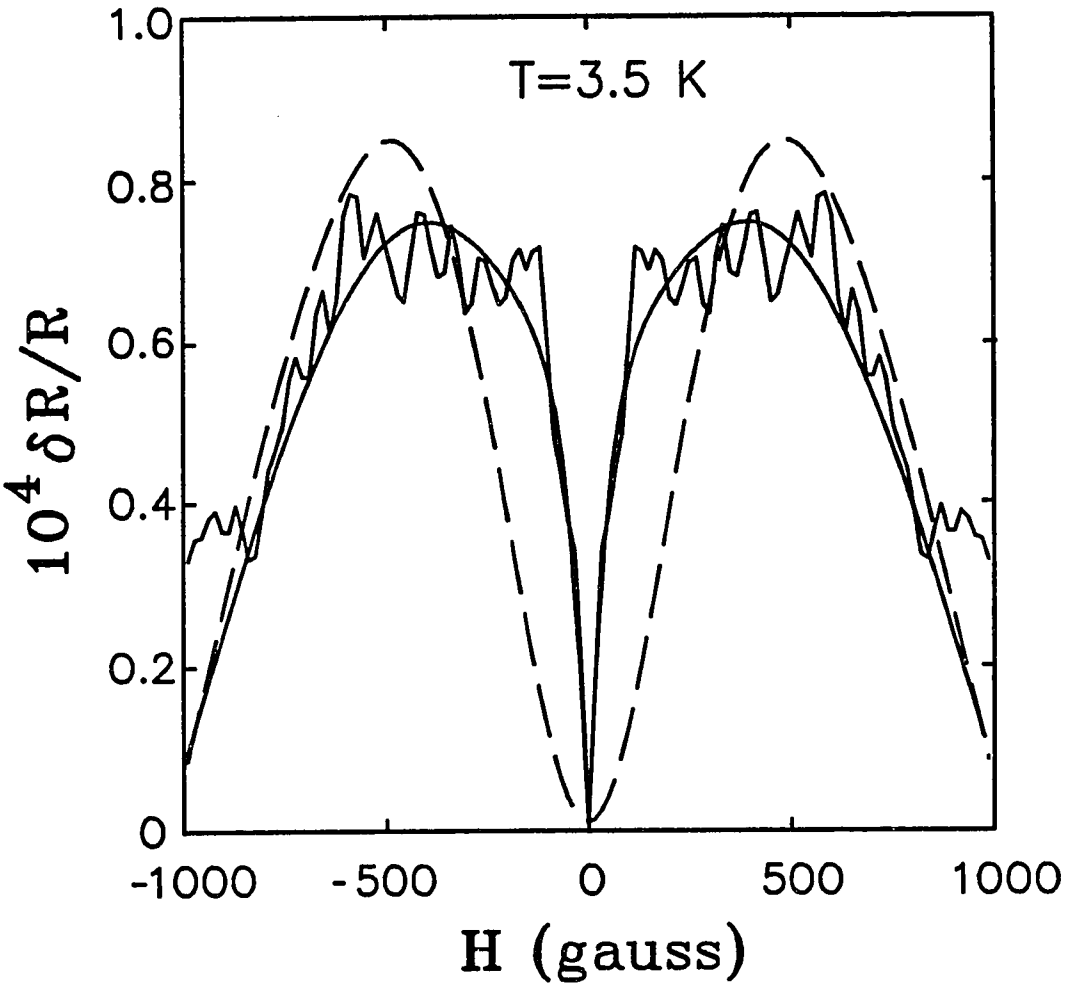

Figure 4.9. Symmetric component of the low field magnetoresistance of Sample RX1, a 1.36 μm wire with wide probes. Solid line, fit to the full theory, Eq. (2.22), with $\ell_\phi = 1.3$ μm, $\ell_{so} = 0.43$ μm; dashed line, fit to the formula appropriate for a short wire with narrow probes, Eq. (2.24), with $\ell_\phi = 0.7$ μm, $\ell_{so} = 0.46$ μm.

characteristic 2D rise in the MR at low fields.

The 2D nature of the MR in Fig. 4.9 is not due to an inadvertent inclusion of the 2D probes in the measured sample, because the four-terminal nature of the measurement ensures that we measure only the short wire between the probes. We have verified this by attempting to fit data for the short wires with wide probes to a sum of a pure 1D and pure 2D magnetoresistances. We find that to explain the general form of the MR, we would have to assume that 90% of the total measured resistance of the sample is due to the 2D measurement probes; even then, the fit is not good. Since it is safe to assume that the majority of the measured resistance of the sample is due to the short wire itself, due to the four-point nature of the measurement, this possibility can be discounted.

For samples with only narrow probes, the effect of the measurement probes on the shape of the MR is a bit more subtle. When all the measurement probes are of the same width as the wire itself, the shape of the MR is identical to that of the corresponding long wire, although the magnitude of the MR may be reduced by a factor equal to the number of probes on one end of the wire. This is because the field dependence of η in Eq. (5.3) is the same as the field dependence of α in Eq. (5.2); the field dependence of both parameters comes through the field dependence of $\ell_\phi(H)$, which is given by Eq. (2.11) with the same value of W for both wire and probes. When the width of the probes W_p is different from the width of the wire W, the field dependence of η and α are no longer identical. Unfortunately, we do not have data from a short wire with wider 1D probes to experimentally illustrate this point. We shall come back to it in the next chapter when we discuss the MR of loops with wider 1D measurement probes.

Physically, these results can be understood if we realise that, in some sense, regardless of the lithographic size of the wire being measured, the actual size of the "sample" is always of length ℓ_ϕ. If ℓ_ϕ is much larger than the lithographic length L, then the "sample" also includes the probes. As a corollary, parts of the probes greater than a distance ℓ_ϕ from the wire do not affect quantum interference effects in the wire. Consider, for example, the short wire with wide probes. The experimental configuration is shown in Fig. 4.1b, whereas the corresponding theoretical formula was derived for Fig. 2.6a. These two configurations are different; specifically, the 1D probes in Fig. 4.1b are of finite length L_p, terminating in additional 2D pads, while the 1D probes of Fig. 2.6b are assumed to extend to infinity. The difference is irrelevant because L_p for our samples is longer than ℓ_ϕ even at the lowest temperature measured. To confirm this, we have fit the data for RX1 to a formula appropriate for Fig. 4.1b. Deriving this formula involves solving the network equations for five nodes (the two additional nodes are at the ends of the 1D probes) instead of three, and only changes the parameter η. For our particular sample parameters, we find no difference between the fits obtained with this five-node formula and the three-node formula. Obviously, at lower temperatures, where $\ell_\phi > L_p$, the difference will become important. A similar situation holds for the short wire with narrow probes. The narrow probes terminate in larger probes away from the ends of the wire, but again the length of the probes L_p for these samples is $\sim 5\ \mu$m, much larger than ℓ_ϕ, so that the boundary conditions at the other end of the probes are irrelevant.

4.3.2 Electron Phase Breaking Lengths in Short Wires

We have seen that measurement probes affect both the magnitude and the shape of the low field MR of short wires, and that with the formulae we derived in Chapter 2, we are able to fit the MR data quite well. The free parameter in these fits is ℓ_ϕ, and a further check on the theory is to compare the values of ℓ_ϕ obtained to those inferred from long wires. This is important because in some cases one may be able to fit the MR data for a short wire with the long wire formula, but with a different value of ℓ_ϕ. For example, for the short wire with four narrow measurement probes in the limit $L << \ell_\phi$, the long wire formula with half the "correct" value of ℓ_ϕ will give a reasonable fit.

Figure 4.10 shows ℓ_ϕ inferred using Eq. (2.24) for the short wires with narrow measurement probes, Samples RX5 and RX22, as a function of temperature. ℓ_ϕ inferred for the co-deposited long wire (using the long wire formula) is also shown. The values of ℓ_ϕ for RX22 in this plot have been normalised to the $R_\square$ and W of the long wire RX3, assuming that the scattering rate at low temperatures is given by the Nyquist rate, Eq. (2.39). The values of ℓ_ϕ for the short wires agree very well with those obtained for the long wire. For comparison, we show the values of ℓ_ϕ inferred for the $L = \sim 1.3$ μm wire (RX5) using the long wire formula. At high temperatures, where ℓ_ϕ is short, these values agree with those obtained for the long wire. At the lowest temperature, these values are about two thirds those for the long wire, as expected.

Figure 4.11 shows the same data for the L=4.76 μm wire with wide probes, Sample RX28. ℓ_ϕ here was inferred using Eq. (2.22), with the appropriate value of η. Again the agreement with the values of ℓ_ϕ for the co-deposited long wire is

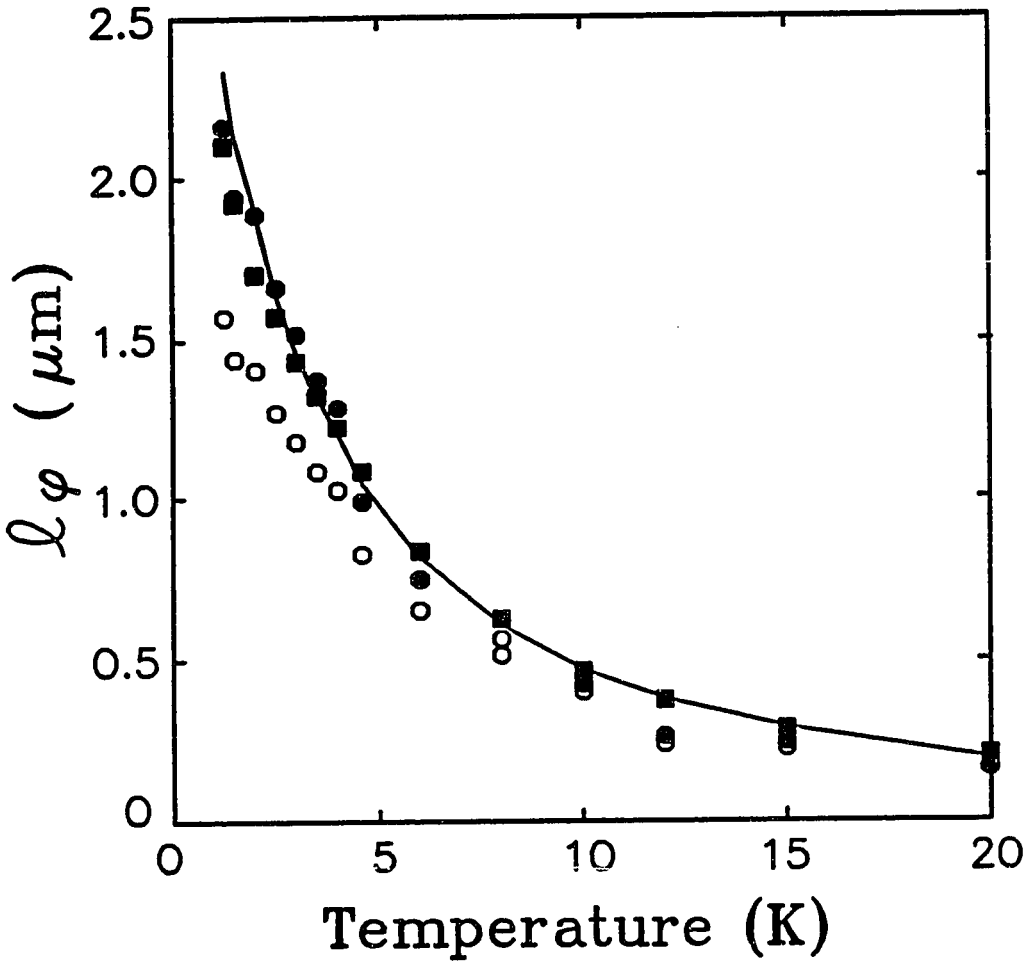

Figure 4.10. ℓ_ϕ as a function of temperature for the short wires with narrow probes, Samples RX5 and RX22, inferred using Eq. (2.24). Solid circles, 1.3 μm wire, RX5; rectangles, 4.9 μm wire, RX22. Open circles are values of ℓ_ϕ inferred for the 1.3 μm wire using the long wire formula. Solid line, values of ℓ_ϕ for the co-deposited long wire, Sample RX3. Data for Sample RX22 have been normalised to the $R_\square$ and W of Sample RX3.

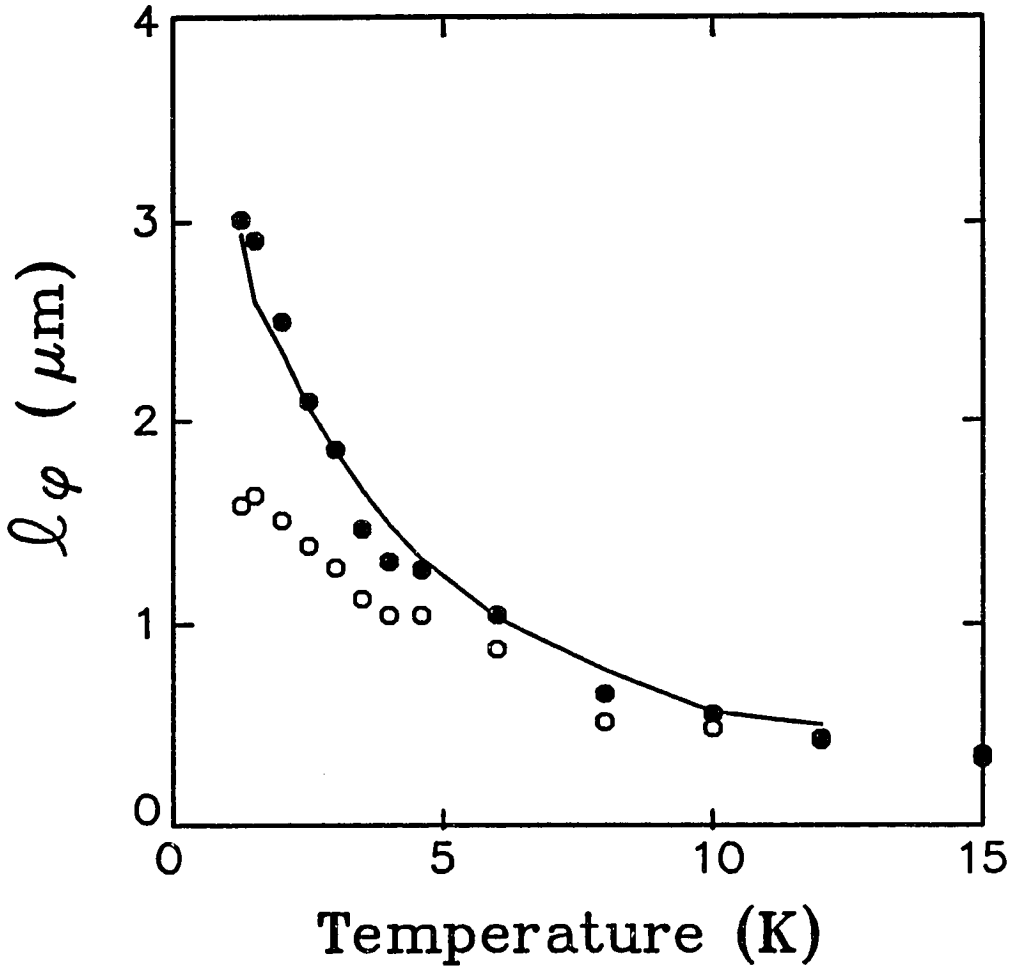

Figure 4.11. ℓ_ϕ as a function of temperature for the 4.76 μm wire with wide probes, Sample RX28. Solid circles, values inferred using Eq. (2.22); open circles, values inferred using the long wire formula, Eq. (2.14). Solid line, values of ℓ_ϕ for the co-deposited long wire, RX27.

excellent. For this wire, since $L \geq 2\ell_\phi$ at all temperatures measured, the 2D characteristic of the pads is not as prominent, and fits to the long wire formula are reasonable. We show the values of ℓ_ϕ inferred from the fits to the long wire formula. Although the fits are reasonable, the values of ℓ_ϕ inferred are almost a factor of two smaller than the true values.

Values of ℓ_ϕ for all four wires, the two wires with wide probes (Samples RX1 and RX28) and the two wires with narrow probes (RX5 and RX22) can be conveniently represented on a single plot by scaling the length of each sample with ℓ_ϕ inferred from its co-deposited long wire, which we shall denote $\ell_\phi^{\text{long wire}}$. These data are shown in Fig. 4.12 on a log-log plot. On this plot, data for the long wires are, by definition, straight lines with slope -1. Data for the two lowest temperatures for Sample RX1, the 1.4 μm wire with wide probes, could not be fit due to the presence of conductance fluctuations. As can be seen, the agreement with $\ell_\phi^{\text{long wire}}$ for all four short wires is excellent. We also show the values of ℓ_ϕ inferred for the L=4.8 μm wire with wide probes, RX28, using the long wire formula. These values are smaller than $\ell_\phi^{\text{long wire}}$ even for $L \sim 4\ell_\phi^{\text{long wire}}$.

One may ask whether the phase coherence lengths for the short wires should indeed be consistent with those for the long wire. ℓ_ϕ at low temperatures is determined by the electron-electron dephasing length. The predictions of Chapter 2 were derived for either infinitely long 1D wires or infinite 2D films; one might expect that the electron-electron dephasing rate would be affected in systems of finite size. This problem is obviously more relevant in the wires of mixed dimensionality, such as the wires with wide measurement probes, than in wires with four probes of the same width as the wire itself. Recalling that the appropriate length scale for electron

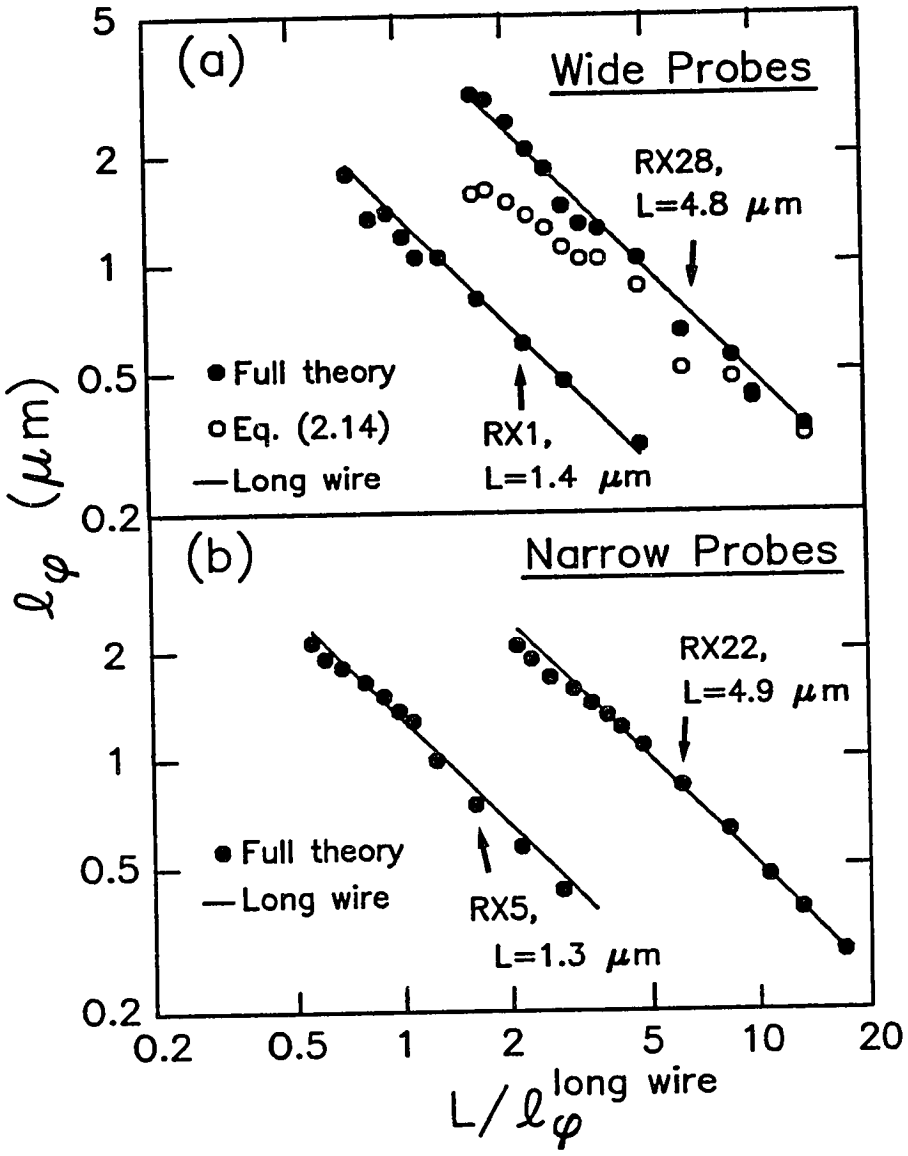

Figure 4.12. ℓ_ϕ vs. $L/\ell_\phi^{\text{long wire}}$ for T=1.25-20 K. Solid lines, with slope -1, are data for long wires, Samples RX3 and RX27. (a). Data for short wires with wide probes, Samples RX1 and RX28. Solid circles from fits to full theory, Eq. (2.22); open circles from fits to long wire formula. (b). Data for short wires with narrow probes, Samples RX5 and RX22. Solid circles from fits to Eq. (2). Data for RX22 have been normalised to the $R_\square$ and W of Sample RX3.

electron scattering is ℓ_T, however, we should expect that the dimensionality of the scattering should be indeterminate only in a region of dimension ℓ_T around the juncture of the 1D and 2D probes. Since $\ell_T << L$ in our samples, the effect on ℓ_ϕ in the major portion of the wire is small, and the values of ℓ_ϕ we obtain should be consistent with those in the long wire.

4.4 Conductance Fluctuations in Short Wires: Effect of Measurement Probes

Figure 4.13 shows the experimental rms amplitude of the conductance fluctuations for four different short wires. The data are plotted as a function of the sample length L normalised to the localisation phase coherence length ℓ_ϕ, determined from the weak localisation MR of the co-deposited long wires. The data for the two short wires with narrow probes (RX5 and RX22) are shown as triangles, the data for the two short wires with wide probes (RX1 and RX28) as circles. Although one cannot make a quantitative comparison of this plot with Fig. 2.9 since Fig. 2.9 does not include the effects of finite temperature and spin-orbit scattering, and Fig. 2.9 shows only the component Fs_a of the correlation function, we see that qualitatively the predictions of Fig. 2.9 are correct: at small L/ℓ_ϕ, the amplitude of the conductance fluctuations for the wires with narrow probes is much larger than the corresponding amplitude for the wires with wide probes, while at $L >> \ell_\phi$, where the effects of the probes are expected to be irrelevant, the amplitude of the conductance fluctuations for wires of both probe configurations is the same.

Figure 4.14 shows the field correlation function at 1.25 K for the L~1.3 μm wires with narrow probes (RX5) and wide probes (RX1). The correlation field H_c for the short wire with wide probes is somewhat larger than that for the wire with narrow

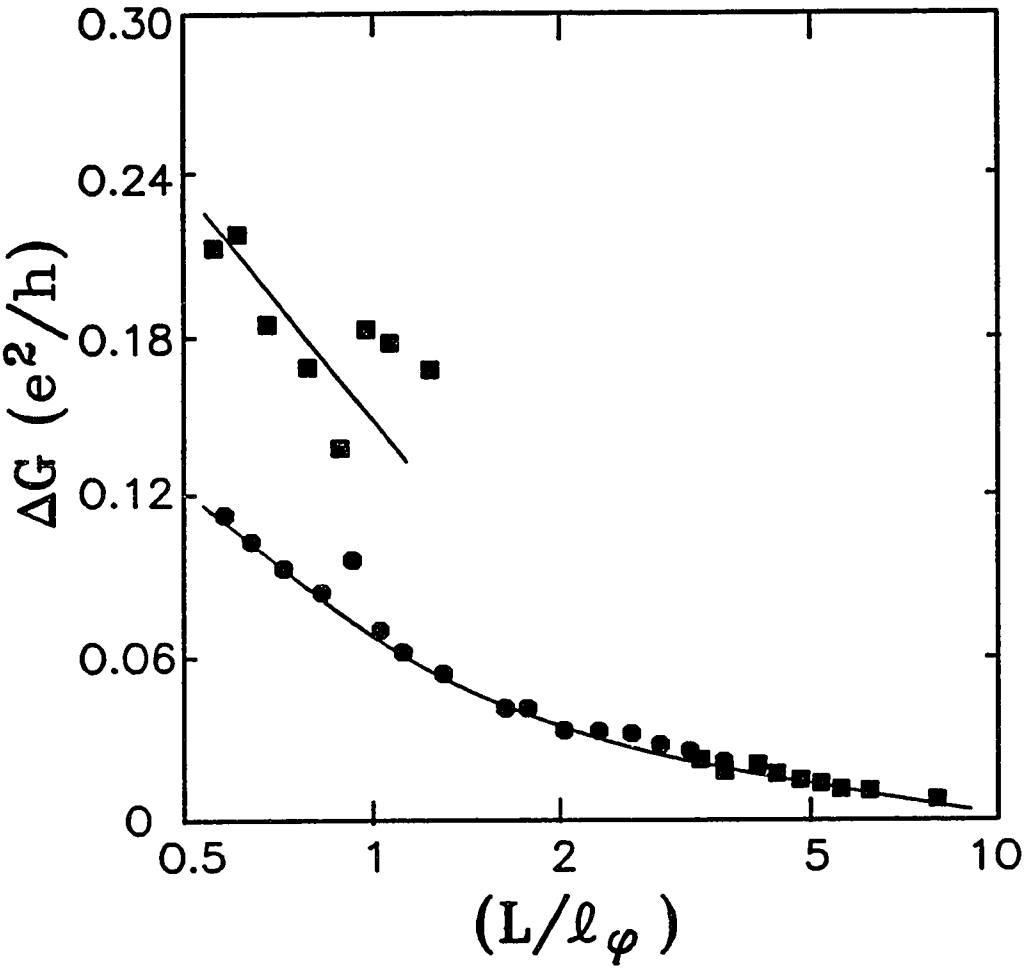

Figure 4.13. Conductance fluctuations, rms amplitude vs. $L/\ell_\phi^{\text{long wire}}$. Rectangles, data for the short wires with narrow probes, Samples RX5 and RX22; circles, data for the short wires with wide probes, Samples RX1 and RX28. The solid lines are guides to the eye.

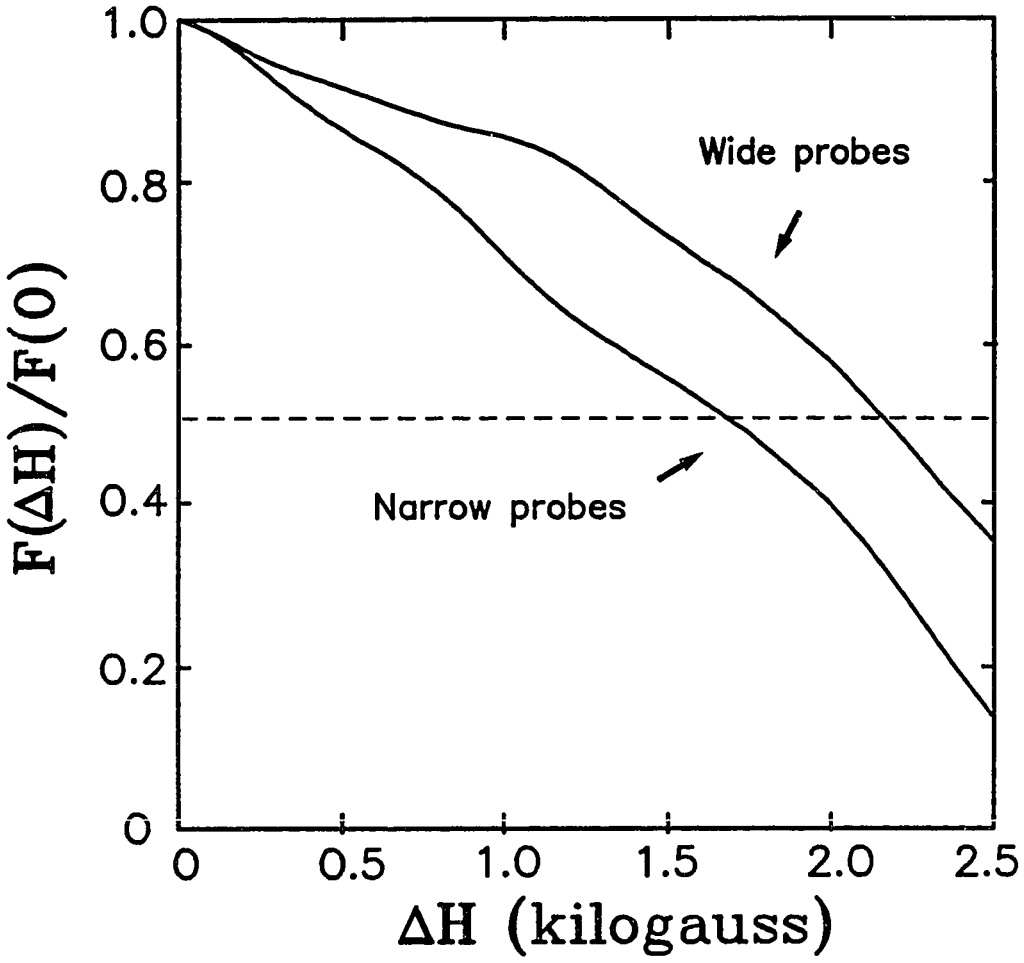

Figure 4.14. Conductance function field correlation function F(ΔH) at 1.25 K for the 1.3 μm wire with narrow probes (Sample RX5) and the 1.36 μm wire with wide probes (Sample RX1). The intersection of the dotted line with the two curves marks the field correlation length H_c.

probes, in accordance with the Fig. 2.10. Once again, however, a direct comparison to Fig. 2.10 is not valid because of the reasons stated above. Furthermore, since the field range over which the correlation function is computed is finite, there is probably some statistical error in the computed values. Nonetheless, the qualitative trend visible in the data is consistent with the theory.

5. Experimental Results: The Aharonov-Bohm Effect in Single Metal Loops

Soon after the initial prediction by Altshuler, Aronov, and Spivak (AAS) [1981] of oscillations of flux period hc/2e in the magnetoresistance of doubly connected disordered metal structures, such oscillations were observed in cylinders of Mg [Sharvin and Sharvin, 1982; Gijs *et al.*, 1984], Li [Altshuler *et al.*, 1982] and Al [Gijs *et al.*, 1984; Gordon *et al.*, 1984]. Measurements on multiply connected geometries showed the same effect [Pannetier *et al.*, 1984; Dolan *et al.*, 1986]. The first experiments on *single* Au and AuPd loops, however, showed neither oscillations of period hc/2e nor hc/e [Umbach *et al.*, 1984]. Subsequent experiments on larger loops were more successful: Oscillations of period hc/e were first observed in Au loops by Webb *et al.* [1985] and in a GaAs quantum well device by Datta *et al.* [1985]; oscillations of both periods (hc/e and hc/2e) were observed at Yale [Chandrasekhar *et al.*, 1985]. This chapter describes the results of the experiments performed at Yale.

We start this chapter with a look at some of the data on the Al, Ag, and Au loops measured at Yale. Qualitatively, except for the low field data for the Al loops, which are enhanced by the Maki-Thompson contribution, data for these different metals are essentially the same. With some exceptions which shall be discussed in detail, loops fabricated from all three metals show both hc/e and AAS hc/2e oscillations. We shall make a detailed quantitative comparison of our data with the theory of both the hc/2e and the hc/e effects, and point out some of the problems. Finally, we shall describe the results of further experiments on the effect of magnetic

impurity scattering in Ag loops, experiments performed in an effort to explain some of the anomalous results found by the IBM group in experiments on Au loops [Washburn and Webb, 1986].

All the loops used in these studies were fabricated using electron beam lithography and characterised as described in Chapter 3. The first loops were circular; later loops were mostly square (Fig. 3.3b), as this gave a narrower linewidth with the raster scan of our e-beam machine. Table 5.1 lists the relevant parameters for some of the Al loops; Table 5.2 lists the relevant parameters for some of the Ag and Au loops, as well as the Ag loops with added Co impurities. Table 5.3 lists additional samples which were measured, but which are not discussed in this thesis.

5.1 Al, Ag and Au Loops: Qualitative Features

5.1.1 Al Loops

Figure 5.1 shows the low field magnetoresistance of one of the first loops measured, a ~2 μm Al loop, Sample 74a.4. The period of the oscillations is ~5 gauss, corresponding to a flux period of hc/2e. Figure 5.1 also shows a fit to the AAS formula, Eq. (2.15), including the effects of MT superconducting fluctuations. The AAS formula can be written as a series

$$\frac{\Delta R(H)}{R} = \frac{R_{\square}}{(\pi\hbar/e^2)} \frac{\ell_{\phi}(H)}{W} \left[1 + e^{-[S/\ell_{\phi}(H)]} \cos(2\pi\phi/\phi_S) + \ldots \right] \quad (5.1)$$

The first term in this series is just the long wire result, Eq. (2.14), which gives rise to the background MR seen in Fig. 5.1. This is the contribution of the 1D wires that make up the loop. Superposed on this background are oscillations of period ϕ_S=hc/2e, whose amplitude decreases with increasing magnetic field. The field to which the

Sample	Geometry	d* (μm)	W (nm)	$R_\square$ (Ω)
68.2	Circle	1.15	350	1.2
73.2	Circle	2.26	230	1.6
73.5	Circle	2.43	220	1.1
74a.4	Circle	2.30	190	1.1
RE4	Square	0.94	78	1.8
RE7	Square	0.92	134	2.0
RE12	Square	0.93	100	1.6
RE13	Square	0.94	80	1.9
RE15	Square	0.95	80	1.8
RS3	Square	1.58	60	2.4
RS6	Square	1.00	80	2.4
RS8	Square	0.54	65	2.4
RS9	Square	0.99	85	2.5
RS16	--Long wire--		80	2.4

*d is the diameter for circular loops, and the length of one side for square loops.

Co-deposited samples are grouped together. ℓ_{so}~0.5 μm for all samples.

Table 5.1. Sample parameters for Al loops.

Sample	Metal[+]	Geometry	d[*] (μm)	W (nm)	$R_\square$ (Ω)
81C.3	Ag	Circle	1.04	140	3.8
83C.1	Ag	Circle	1.04	140	6.0
RI13	Ag	Square	0.91	49	2.3
RL8	Ag+Co	Square	0.91	65	2.7
RL21	Ag	Square	0.94	76	3.1
RO8	Ag+Co	Square	1.00	65	2.1
RR5	Ag+Co	Circle	0.99	64	3.3
RR7	Ag+Co	Circle	1.00	80	1.6
SE2	Au	Circle	0.83	107	4.2
SE6	Au	Circle	0.89	140	4.2

[+]The notation Ag+Co refers to Ag films with ~0.01 atomic layer of Co on the surface.

[*]d refers to the diameter for the circular loops, and to the length of one side for the square loops.

Co-deposited samples are grouped together. ℓ_{so}~0.5 μm for all samples.

Table 5.2. Sample parameters for the normal-metal loops.

Sample	Geometry	Metal[1]	Type of Experiment
SE4	Loop	Au	Aharonov-Bohm Effect
73.1	"	Al	"
73.3	"	"	"
73.4	"	"	"
73.6	"	"	"
RE6	"	"	"
RE9	"	"	"
RF3	"	Ag+Co	Magnetic Scattering
RF11	"	"	"
RF13	"	"	"
RG10	"	"	"
RH1	"	"	"
RR5	"	"	"
RT13	"	Au+Mn	"
RT25	Long wire	Au+Mn	Magnetic Scattering
RL9	Long wire	Au+Co	Magnetic Scattering
T2D1	2D film	Au	Magnetic Scattering
T2D2	"	Au+Mn	"
2D2Al	"	Al+Co	"
2D3Al	"	Al	"
A8	"	Ag	"
Ag12	"	Ag	"
Ag13	"	Ag+Co	"
Ag14	"	Ag+Co	"
Ag15	"	Ag	"
Ag16	"	Ag+Co	"
Ag17	"	Ag	"
Ag18	"	Ag+Co	"
Ag20	"	Ag	"
Ag29	"	Ag+Co	"

[1]The notation Ag+Co refers to Ag films with surface Co impurities, and the notation Au+Mn refers to Au films with ion-implanted Mn impurities.

Table 5.3. Additional samples measured. Table continued on next page.

Sample	Geometry	Metal[1]	Type of Experiment
2D1Ag	2D film	Ag	Magnetic Scattering
2D3Ag	"	"	"
2D4Ag	"	"	"
2D5Ag	"	"	"
2D8Ag	"	Ag+Co	"
2D9Ag	"	Ag+Co	"
2D10Ag	"	Ag	"
RK2D	"	Ag+Co	"
Co1	"	Co	"

[1]The notation refers to Ag films with surface Co impurities.

Table 5.3 continued

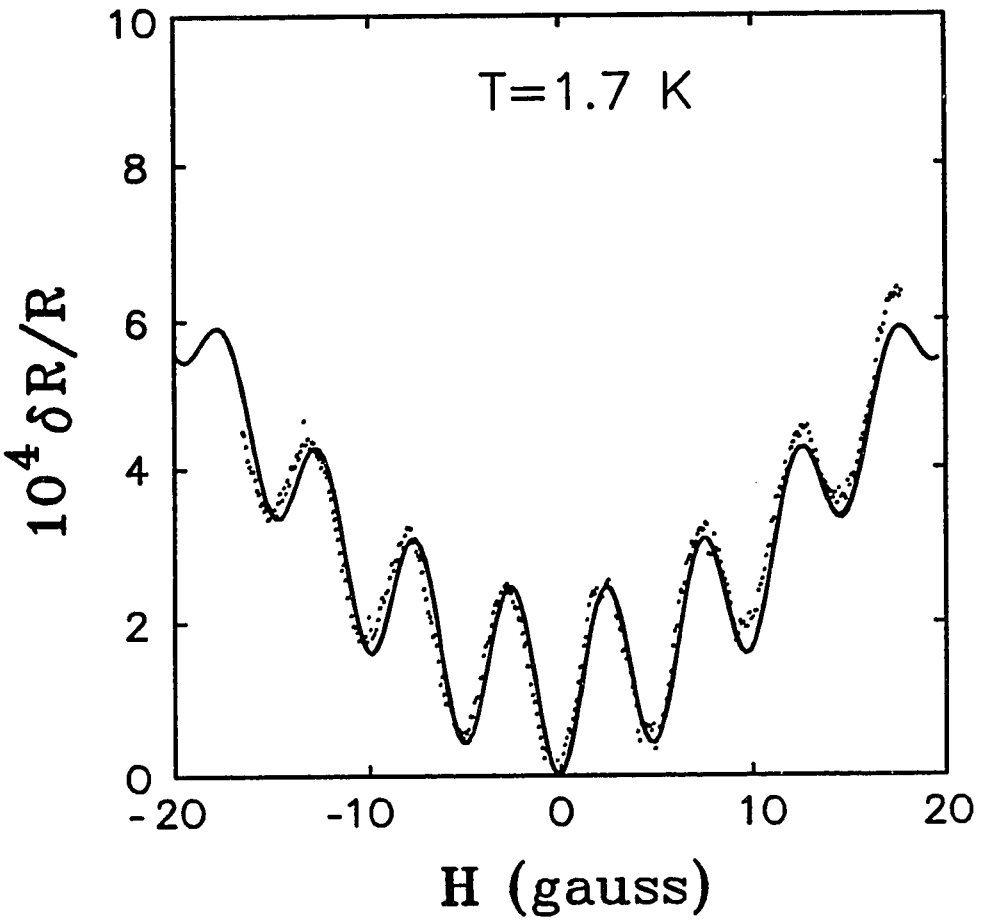

Figure 5.1. Low field magnetoresistance of a ~2 μm Al loop, Sample 74a.4, at 1.7 K. Dots are the data, solid line is a fit to the AAS formula with the parameters $\ell_\phi = 1.7$ μm and $\ell_{so} = 0.5$ μm. $\beta = 5.3$ at this temperature.

oscillations persist is dependent on the linewidth of the loop- the smaller the linewidth, the larger the field. More precisely, it is the ratio of the linewidth to the diameter of the loop, the so-called aspect ratio, that must be small if the oscillations are to be well-defined. For the loop in Fig. 5.1, the aspect ratio is (100 nm/2.32 μm)~0.04, which is quite small.

The relatively large amplitude of the oscillations in Fig. 5.1 is due to the presence of Maki-Thompson (MT) superconducting fluctuations. Recall that in the case of a superconductor with strong spin-orbit scattering, the weak localisation singlet term is multiplied by a factor (β+1/2) [Eq. 2.50], where β is the contribution of MT superconducting fluctuations and 1/2 the contribution of weak localisation. β at T=1.7 K for this sample is 5.3; thus, the major contribution to the MR in Fig. 5.1 is from MT fluctuations. The data cannot be fit, however, if the localisation contribution is ignored. This is even more evident at higher temperatures, where the contribution of the MT fluctuations is much smaller.

Figure 5.2a shows the low field MR of another Al loop, Sample RE13, a ~1 μm square loop, at 2.0 K. This plot shows more clearly the attenuation of the oscillations with increasing magnetic field. Given the presence of well-developed AAS oscillations in this sample, one might reasonably expect to see correspondingly well-developed hc/e oscillations at higher magnetic fields. Fig. 5.2b shows the MR of the same loop at 1.3 K from 2.5 to 5.0 kG, a field range at which the localisation and MT contributions are suppressed. No clear oscillations of period hc/e can be seen. None of the MR sweeps of this sample showed clear evidence of hc/e oscillations. The same null result was obtained in all of the early experiments on Al loops [Chandrasekhar *et al.*, 1985].

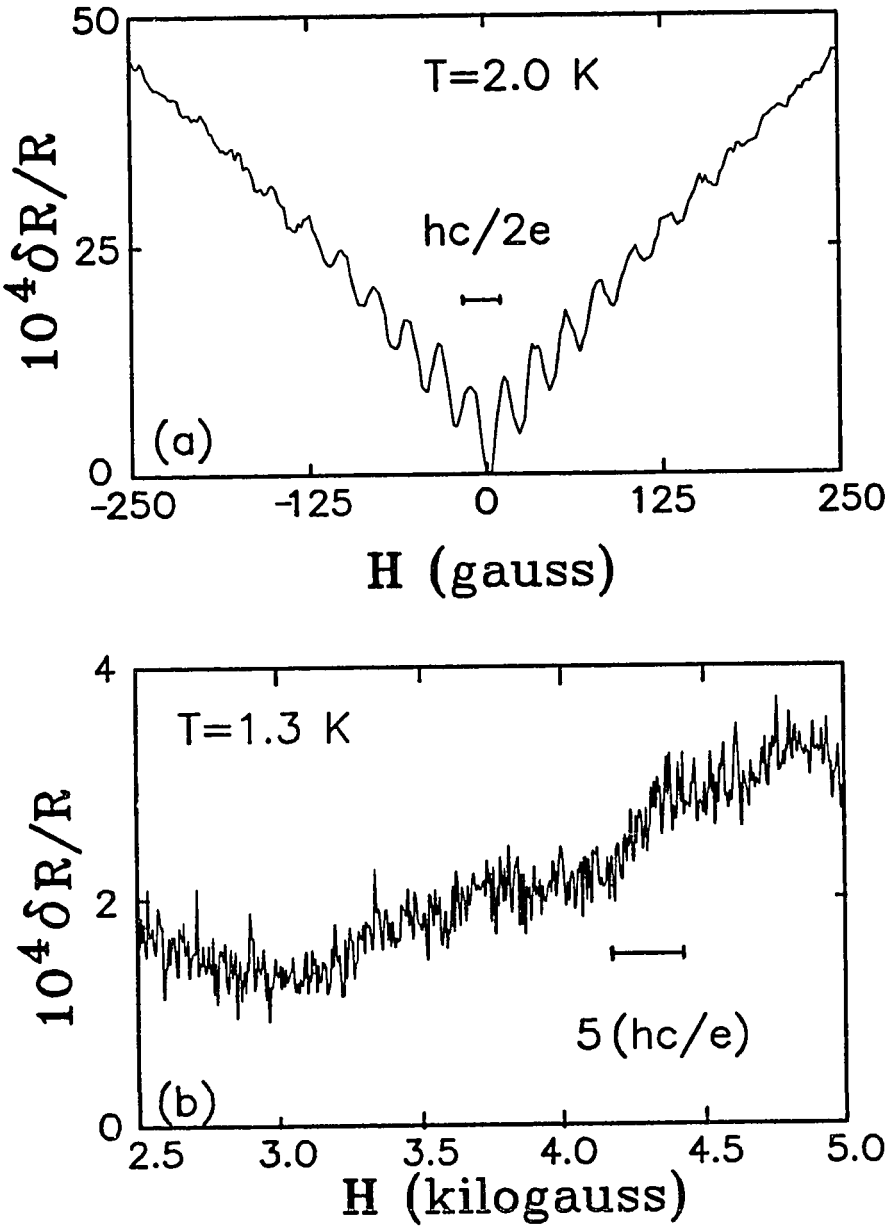

Figure 5.2. (a). Low field magnetoresistance of Sample RE13, a ~1.0 μm Al loop, at 2.0 K. (b). High field magnetoresistance of the same loop at 1.3 K. The bar marks the period expected for the hc/e oscillations.

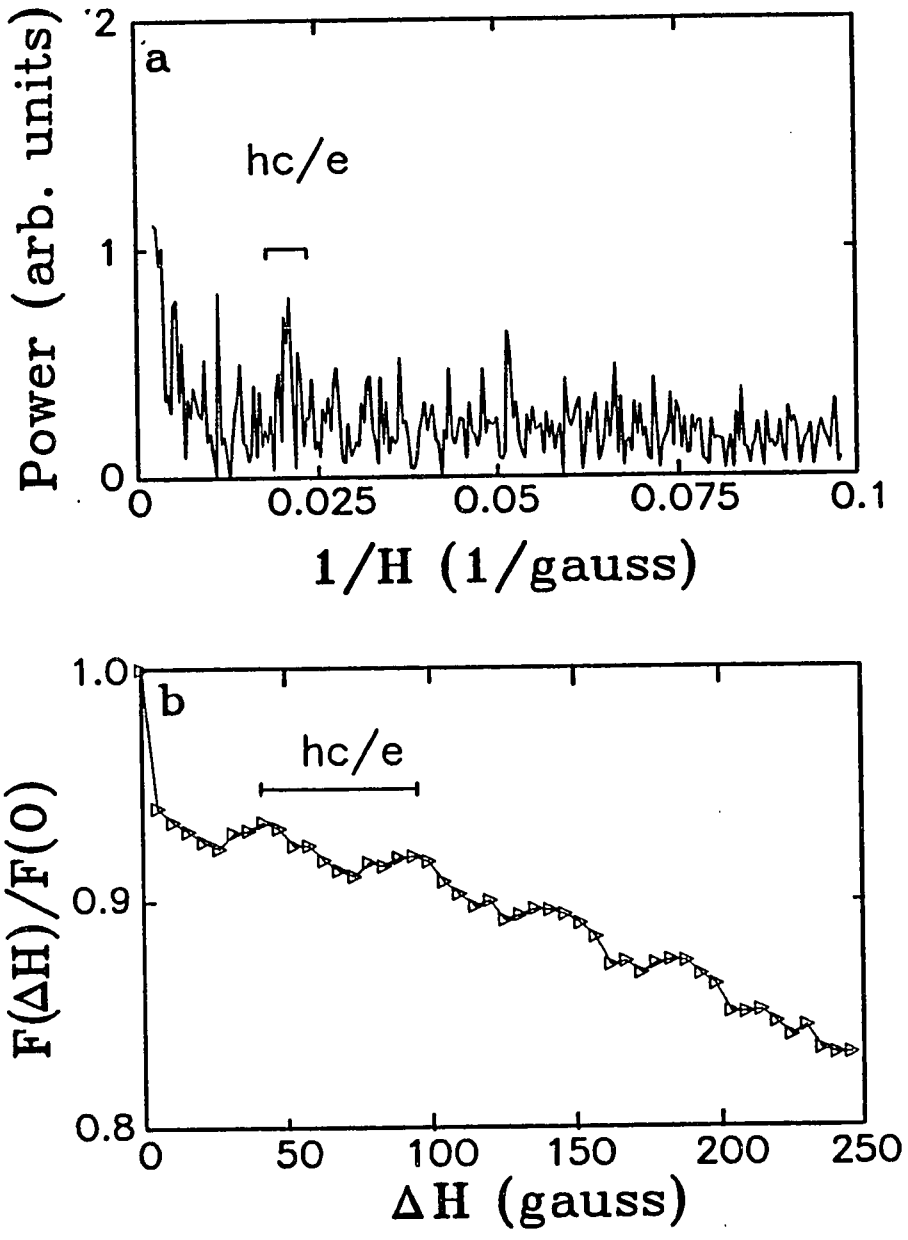

Figure 5.3. (a). Fourier transform of the data in Fig. 5.2b. The frequency range corresponding to a flux ϕ_0 through the inner and outer areas of the loop is marked. (b). Autocorrelation function of the data in Fig. 5.2b, showing oscillations of period hc/e.

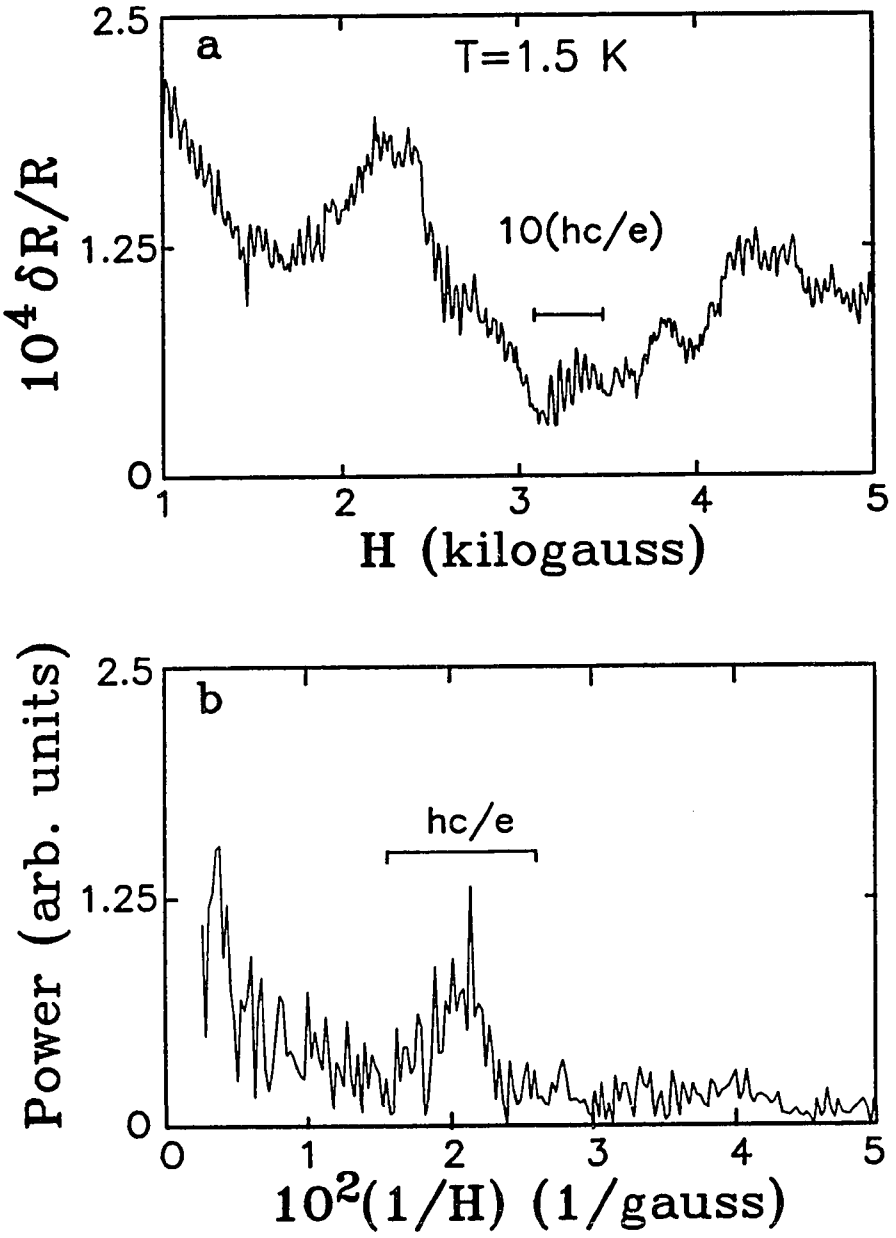

Figure 5.4. (a). High field magnetoresistance of a ~1 μm Al loop, Sample RE7, showing oscillations of period ϕ_0=hc/e. (b). Fourier transform of the data in (a).

In fact, hc/e oscillations are present in the data in Fig. 5.2b. The Fourier transform of the data in Fig. 5.2b, shown in Fig. 5.3a, shows no clear peak at the value of 1/H corresponding to hc/e oscillations. The autocorrelation function of the same data, however, shows clear oscillations of period ~46 gauss, double the period of the hc/2e oscillations seen in Fig. 5.2a. This evidence of hc/e oscillations led us to renew our search for hc/e oscillations in Al loops. Fig. 5.4a shows high field data for another ~1 μm Al loop, Sample RE7, fabricated at the same time as Sample RE13. Here, the hc/e oscillations are easily discernible, and the Fourier transform (Fig. 5.4b) shows a well-defined peak at a value of 1/H corresponding to a flux of hc/e through the loop. Subsequently, we have seen well-defined hc/e oscillations in a number of Al loops. We are not certain why hc/e oscillations were not visible in the earlier Al loops. Better measurement techniques may partly explain why we have been more successful recently, but hc/e oscillations still remain more difficult to observe in Al loops than in Ag or Au loops [S. Klepper, private communication].

The data in Fig. 5.4a illustrates some general characteristics of the hc/e oscillations. The oscillations are superposed on a randomly varying background which is the conductance fluctuation contribution of the narrow wires making up the loop. The oscillations are well developed at some values of magnetic field; at other values, they are suppressed. This "beating" phenomenon is again due to the penetration of the magnetic field into the arms of the loop, and the width in field of one of these "beats" is on the order of the field required to kill the AAS hc/e oscillations.

5.1.2 Ag Loops

One of the objections raised earlier against our observation of hc/2e oscillations

in Al loops was that the oscillations were a superconducting fluctuation effect, rather than a normal electron effect, in spite of the fact that these oscillations were observed up to ~8 K, where the superconducting fluctuation contribution is small. We therefore decided to fabricate and measure normal-metal loops. Fig. 5.5 shows the low field MR of a ~1 μm square Ag loop, Sample RI13, at 1.25 K. The AAS oscillations are clearly visible, but the Fourier transform of these data shows the presence of hc/e oscillations as well. The amplitude of the hc/e oscillations is of the same order as the *localisation* correction; they are thus not visible in the low field MR of the Al loops, where they are swamped by the MT contribution, but can be seen in the low field data of normal metal loops. Note that, due to the absence of MT fluctuations, the size of the average background MR is about one-fifth that of the Al loop shown in Fig. 5.2a. Figure 5.6 shows MR data for the same Ag loop at ~4 kG, where the localization contribution is suppressed. Not surprisingly, the hc/e oscillations are more prominent.

5.1.3 Au Loops

The data for the Au loops are very similar to the data for the Ag loops: Both hc/e and AAS hc/2e oscillations are present at low fields, and only hc/e oscillations at are present at higher fields. At the risk of boring the reader, we show in Fig. 5.7 the low field MR for a ~1 μm circular Au loop, Sample SE2; high field data are shown in Fig. 5.8. We show these data in particular because the AAS hc/2e and weak localization contributions were conspicuously absent from the low field MR of the Au loops measured by another group [Washburn and Webb, 1986]. Both these contributions are present in the Au loops we have measured. Note that the AAS

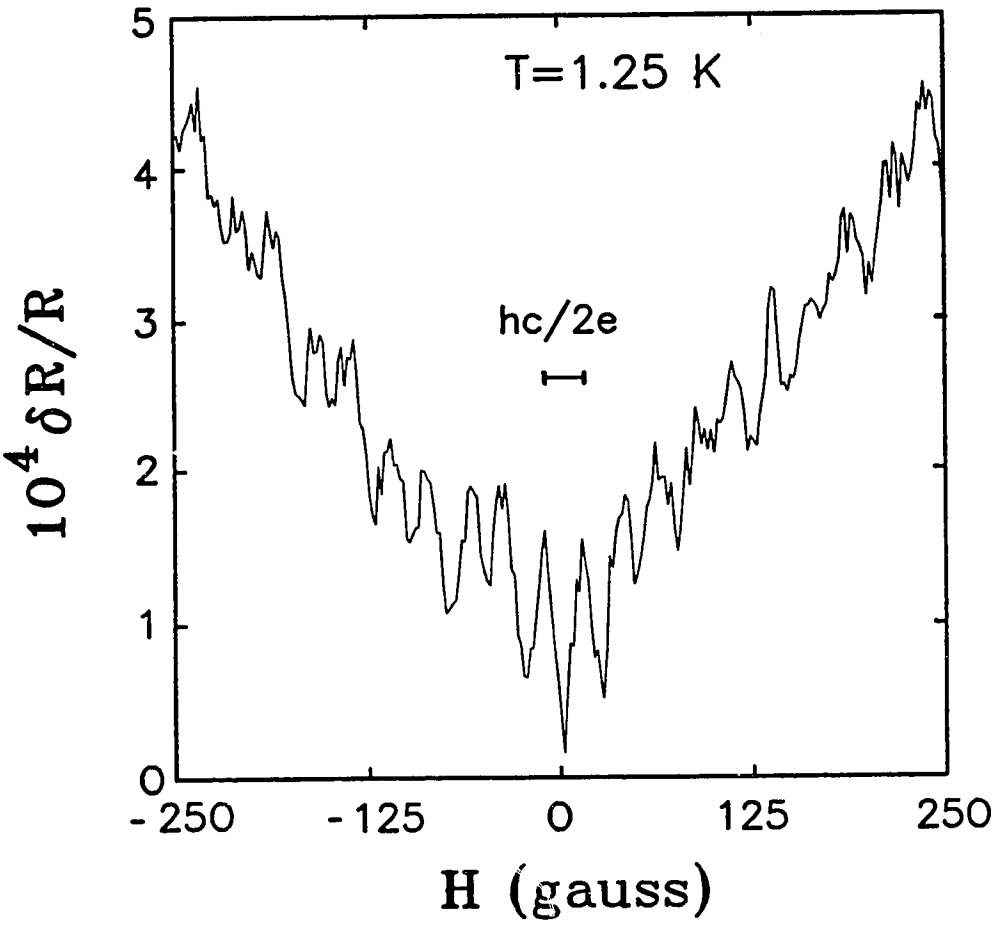

Figure 5.5. Low field magnetoresistance of a ~1 μm Ag loop, Sample RI13, at 1.25 K.

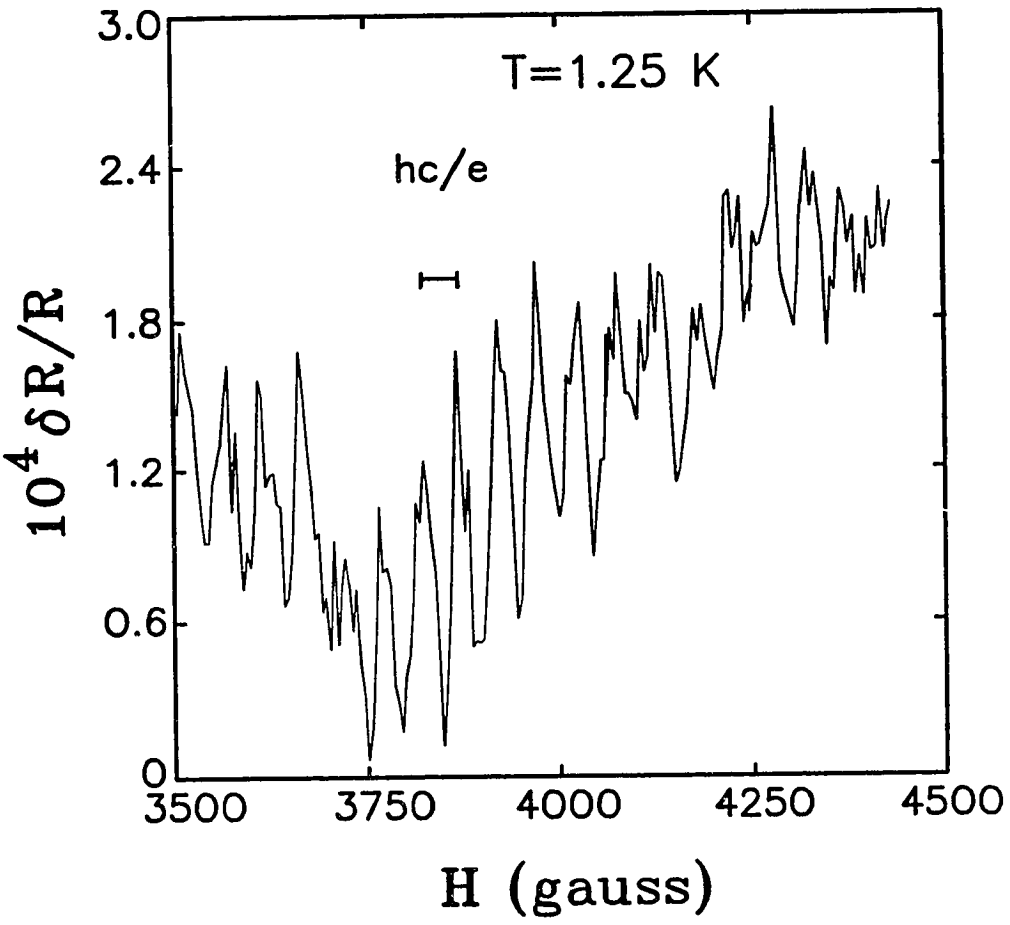

Figure 5.6. High field magnetoresistance of the loop of Fig. 5.5.

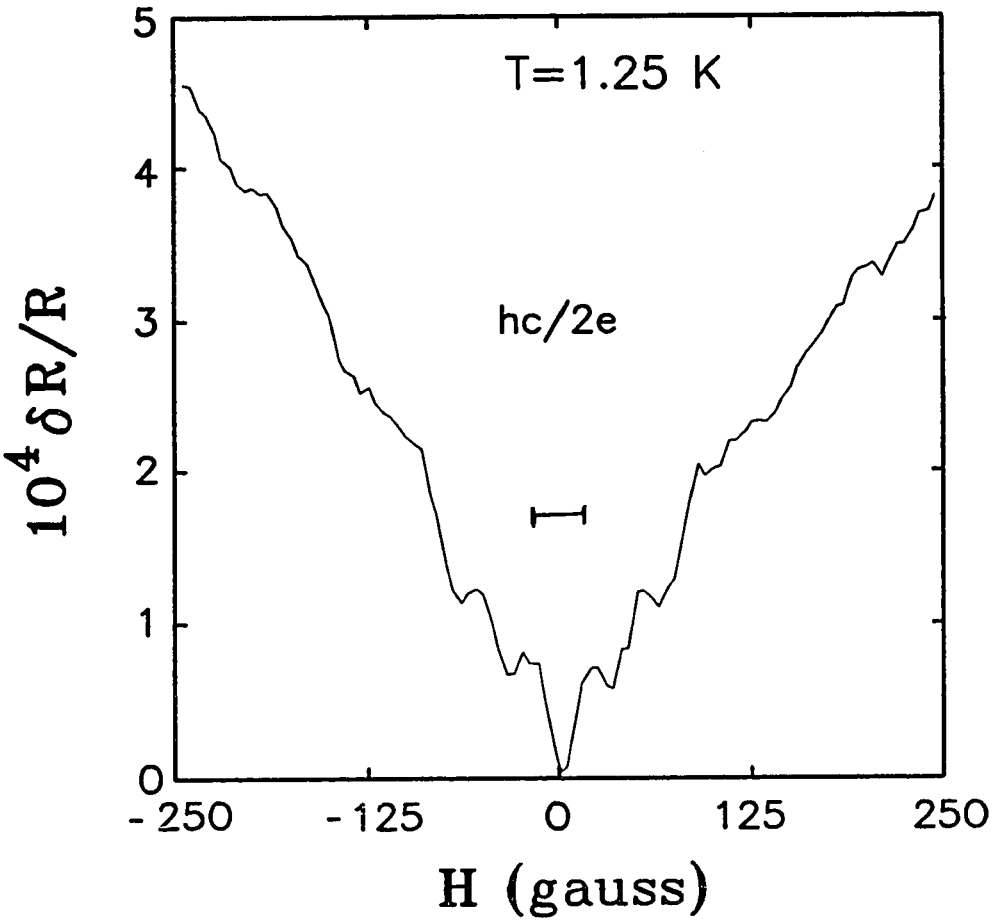

Figure 5.7. Low field magnetoresistance of a ~1 μm Au loop, Sample SE2, at 1.25 K, showing AAS oscillations of period hc/2e.

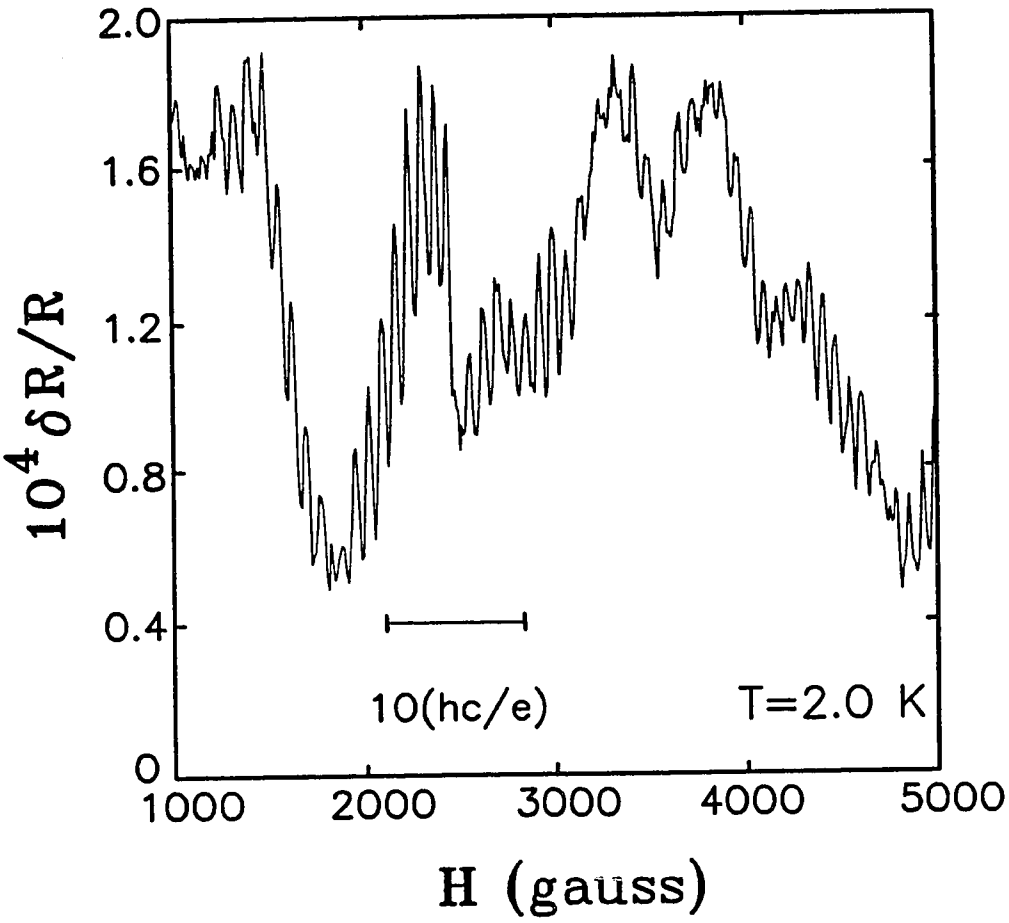

Figure 5.8. High field magnetoresistance of the loop of Fig. 5.7, showing oscillations of period hc/e.

oscillations in Fig. 5.7 are attenuated rapidly with field; this is because the aspect ratio of this sample is relatively large (~0.13).

It is useful to briefly summarise the results discussed above before we examine the detailed magnetic field and temperature dependence of the Aharonov-Bohm effect. In the first experiments on metal loops [Webb *et al.*, 1985; Chandrasekhar *et al.*, 1985], only the Ag loops studied at Yale showed both the hc/e and AAS hc/2e effects. The Al loops at Yale showed AAS oscillations but no hc/e oscillations, and the Au loops at IBM showed hc/e oscillations but no AAS oscillations. Subsequently, as we have discussed, hc/e oscillations have been observed in Al loops. In the Au loops measured at IBM, however, AAS oscillations have still not been seen [Washburn and Webb, 1986]. This is all the more puzzling since the Au loops studied at Yale do show the AAS hc/2e effect.

Based on the experiments we have performed, we can state that loops fabricated from Al, Ag and Au all show both the hc/e and the AAS hc/2e Aharonov-Bohm oscillations. The absence of AAS oscillations in the IBM loops remains a puzzle which we shall address later in this chapter. It is interesting to note that more recent data on Sb loops at IBM [Milliken *et al.*, 1987] also do not show low field hc/2e oscillations, although they exhibit what appears to be weak localisation at low fields. We shall discuss the IBM Sb data in detail in Chapter 6.

5.2 Al, Ag and Au Loops: Quantitative Analysis

5.2.1 Low Field hc/2e Oscillations

The quality of the fit for the ~2 μm Al loop shown in Fig. 5.1 might lead one to believe that the AAS formula accurately describes the weak localisation Aharonov

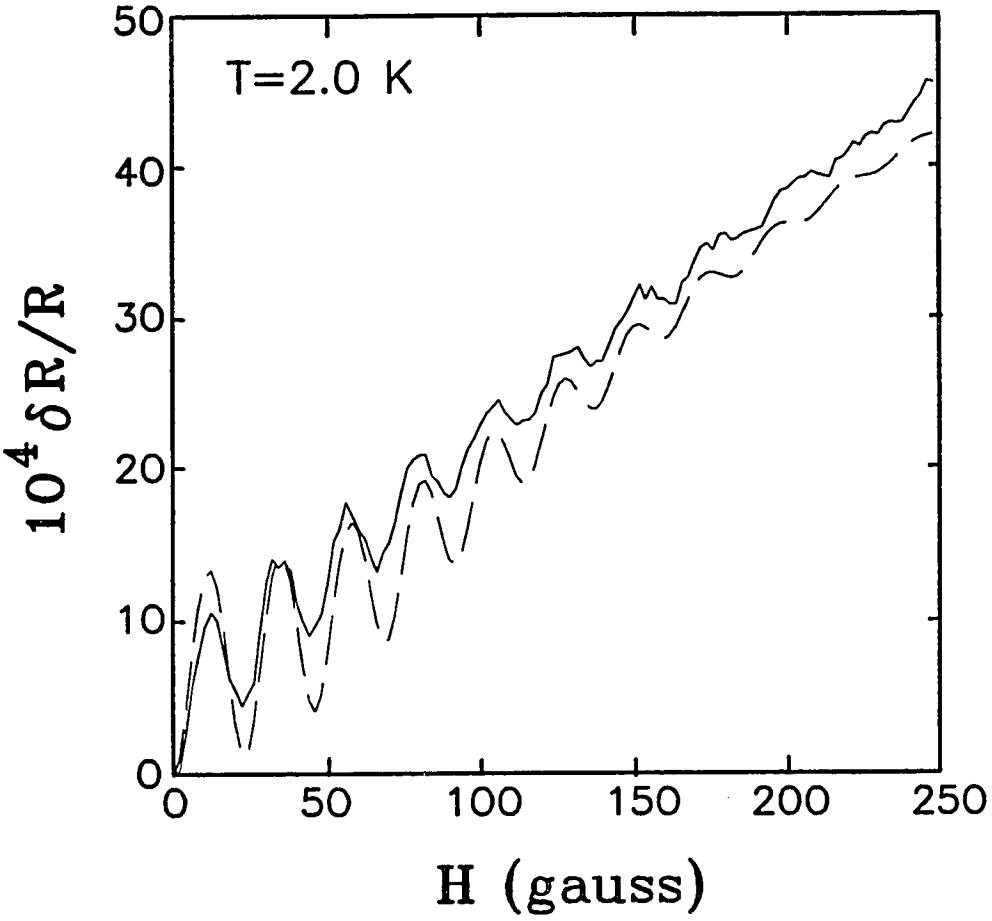

Figure 5.9. Data of Fig. 5.2a, the low field magnetoresistance of Sample RE13, a ~1 μm Al loop. Solid line is the data, dashed line is a fit to the AAS formula with the parameters $\ell_\phi = 1.2$ μm, $\ell_{SO} = 0.45$ μm.

Bohm effect. For smaller loops, this is not the case. We shall illustrate this point with low field magnetoresistance data from Al loops, which are not complicated by the presence of conductance fluctuations and the hc/e Aharonov-Bohm effect. Figure 5.9 shows similar data from the ~1 μm Al loop of Fig. 5.2a, along with a best fit to the AAS formula. These data were fit using ℓ_ϕ and ℓ_{so} as fitting parameters. The fit is actually quite insensitive to ℓ_{so} because the quantum conductivity correction at this temperature is dominated by the weak localisation singlet and MT terms (which are independent of ℓ_{so}), so that, in essence, the only free parameter in the fit is ℓ_ϕ.

There are two problems with this fit which are characteristic of all attempts to fit the AAS formula to small loops at the lowest temperatures. First, and most obvious, is that the fit is quantitatively unsatisfactory. The background MR and the oscillations cannot both be fit with the AAS formula: If one attempts to fit the background MR, as we have done in Fig. 5.9, one overestimates the amplitude of the oscillations. Second, the value of ℓ_ϕ inferred from even this fit is smaller than expected from our studies on long 1D wires. Both problems are more acute at lower temperatures, where ℓ_ϕ is comparable to or larger than the size of the sample.

From our discussion of weak localisation in short wires in the previous chapter, we can immediately identify the source of these problems: The measurement probes of the loops affect both the shape and the magnitude of the MR when ℓ_ϕ becomes comparable to the dimensions of the loop. As such, the effect of the probes should be more pronounced in smaller loops. This is what is found experimentally. Figure 5.10 shows the low field MR at 2.5 K for Sample RS8, a ~0.5 μm Al loop, along with the best fit to the AAS formula. It is obvious that the quality of the fit is much worse than that for the ~1.0 μm loop shown in Fig. 5.9. The amplitude of the first

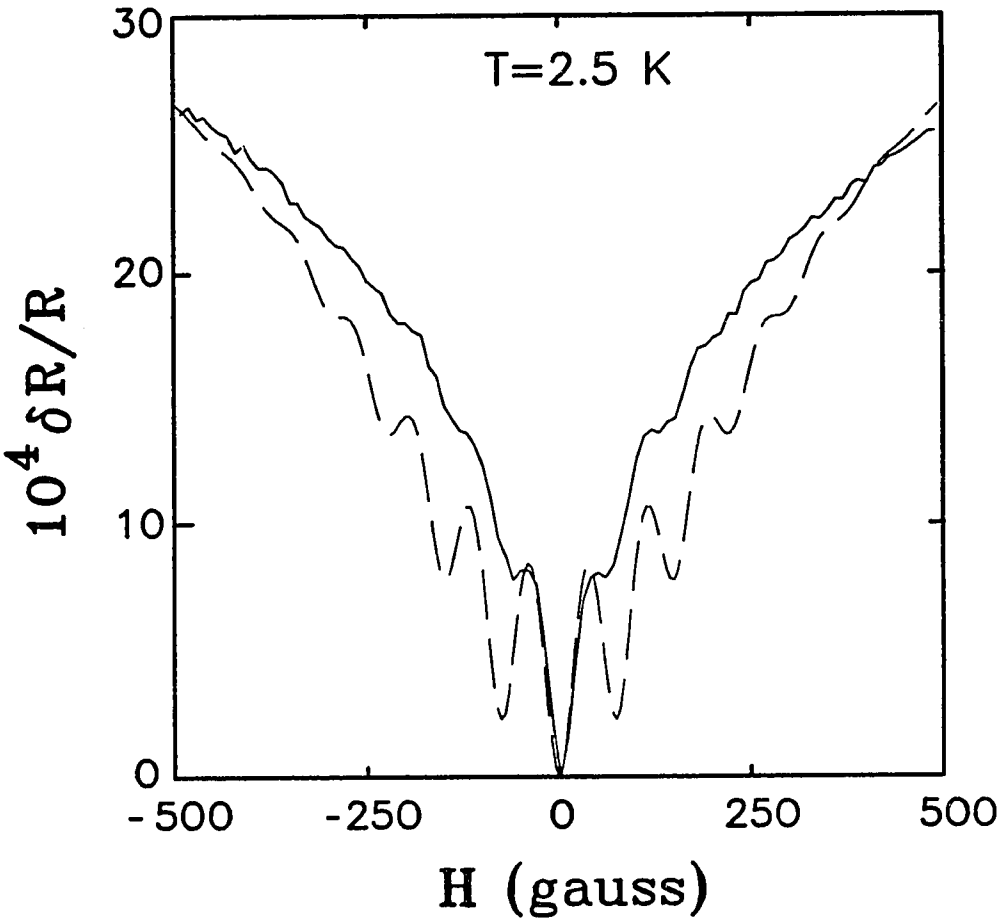

Figure 5.10. Low field magnetoresistance of a ~0.5 μm Al loop, Sample RS8, at 2.5 K. Solid line is the data, dashed line is the best fit to the AAS formula with the parameters ℓ_ϕ=0.7 μm and ℓ_{so}=0.48 μm.

oscillation is much larger than the amplitude of the second and subsequent oscillations; these data should be compared to the data from the ~2.0 μm loop shown in Fig. 5.1. Note also that the value of ℓ_ϕ=0.7 μm inferred from the fit is much smaller than the corresponding value of ℓ_ϕ=1.38 μm for the co-deposited long wire, Sample RS16.

Having identified the source of the problem, the solution seems clear: we need to take into account the effect of the measurement probes on quantum interference in loops. This is easier said than done. The experiments on the loops described in this chapter preceded the experiments on short wires described in Chapter 4, and were therefore performed before we had a good understanding of the effect of measurement probes on quantum inteference. (In fact, our data on the Aharonov-Bohm effect in loops of different sizes triggered our studies on the effect of measurement probes on quantum interference in short wires.) Thus, the design of the measurement probes of the loops we have measured was driven more by lithographic considerations than anything else, making theoretical modelling of the probe geometry extremely complicated. An example of the probe configuration of the loops is shown in Fig. 3.3b; it can be seen that the probes are neither strictly 1D nor strictly 2D, but lie somewhere in between. In addition, the lithographically defined sample consists not only of the loop itself, but also two short 1D wires which connect the loop to the probes. A single loop with simple 1D probes, by virtue of its doubly-connected structure, is already far more complicated than a single wire; these additional details only make the calculations more difficult.

Instead of attempting to use the formalism of Chapter 2 to solve for the exact geometry of the loops, a process which, though tedious, is nevertheless possible, we

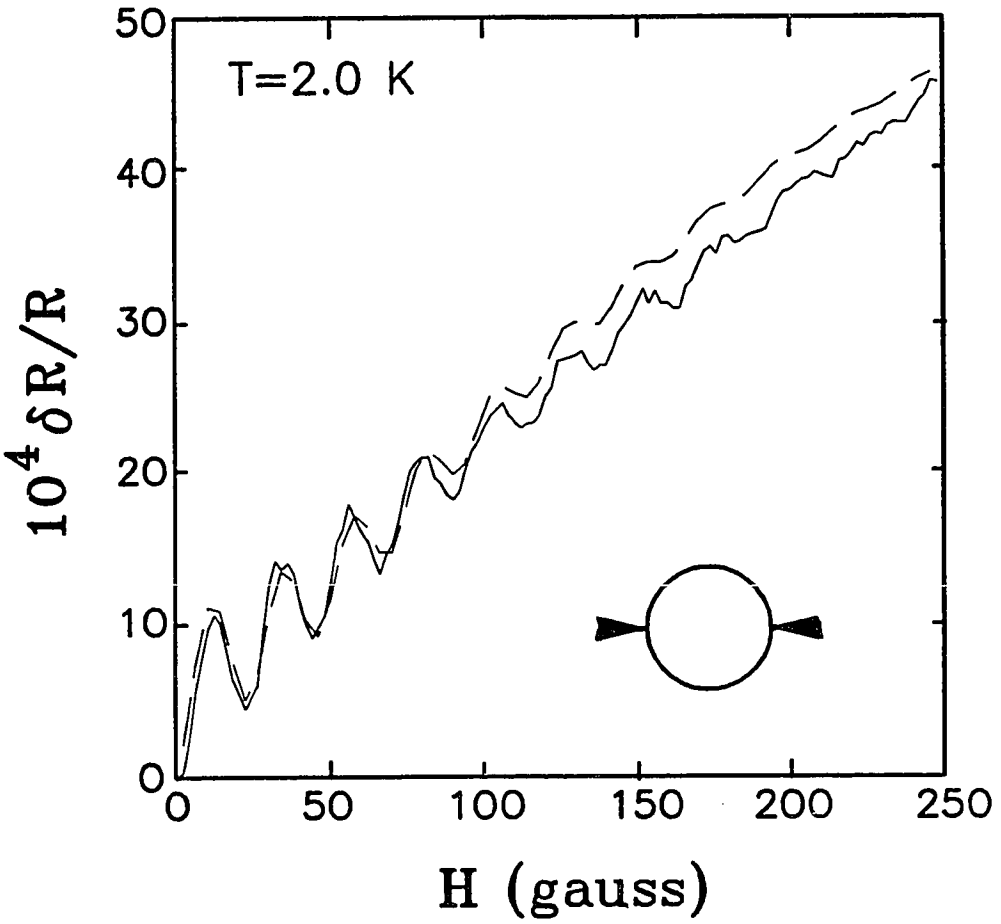

Figure 5.11. Solid line: same data as in Fig. 5.9; dashed line: fit to weak localisation correction which takes into account the effect of the measurement probes, with the parameters $\ell_\phi = 1.7$ μm, $\ell_{so} = 0.45$ μm, angle subtended by each of the 2D probes, 11°. Inset: Geometry assumed in deriving the weak localisation formula.

shall solve for the simpler geometry shown in the inset to Fig 5.11. This geometry consists of a loop with a small sliver of a 2D film attached as a probe on either side. We choose to approximate the probes by sections of 2D films rather than by 1D wires, since the probes in our samples are not of constant width (Fig. 3.3b). Although from the diagram in Fig. 5.11, it appears that the model describes a 2-probe measurement, this is not the case; the conductivity correction is calculated only for the loop itself. The calculation is similar to the calculation for the short wires with 2D probes, only a little more involved. We shall give here neither the details of the calculation nor the analytical form of the weak localisation correction obtained, but just show the resulting fit to the data from the ~1 μm loop of Fig. 5.9. This is shown in Fig. 5.11; the caption to the figure contains the relevant fitting parameters. The fit, though not perfect, is considerably better than the fit to the AAS formula in Fig. 5.9. Although the choice of some of the fitting parameters cannot be justified rigorously, the values are certainly reasonable. The value of $\ell_\phi = 1.7$ μm is somewhat larger than what we would expect for a 1D wire at this temperature (~1.54 μm at 2.0 K for Sample RS16, for example), a more realistic geometry would presumably give better agreement. In fitting these data, it was found that the amplitude of the oscillations are more sensitive to size of the probes than the background MR: Increasing the size of the probes rapidly decreased the amplitude of the oscillations; the effect on the background MR was less drastic.

Fits to data for the ~0.5 μm loop (Sample RS8) using the same formula were less successful, in the sense that the exact shape of the MR curve could not be fit, although the large size of the first oscillation (Fig. 5.10) and the rapid attenuation of the oscillations can be seen in the fits. This is expected, since the limitations of the

geometry assumed in the calculation should be more apparent in the smaller samples. For a better fit, we must take into account the exact geometry of the probes and the small sections of 1D wires that join the loop to the probes. These small wires contribute to both the background MR and the oscillations.

The discussion of the hc/2e Aharonov-Bohm effect has been restricted to Al loops because the low field MR of Al loops is not complicated by contributions from sample-specific effects such as conductance fluctutations or the hc/e Aharonov-Bohm effect. For the Ag and Au loops, these contributions are present in the low field MR, and must be filtered out before the data can be analysed. Apart from this, however, data for the Ag and Au loops show the same behaviour as data for the Al loops.

5.2.2 The hc/e Aharonov-Bohm Effect

The theory of conductance fluctuations and the hc/e Aharonov-Bohm effect predicts averages over magnetic fields. Ideally, these averages should be calculated over an infinite range in magnetic field; practically, for the hc/e Aharonov-Bohm effect, the average should be over a range large enough to include a fair number of oscillations. The hc/e amplitudes discussed below are averages over 80-100 periods, large enough to give an accurate value; quite often, they are also averages over a number of different MR sweeps taken at different times at the same temperature. The temperature range over which we can observe the hc/e effect is 1.25-6 K. The lower limit is the temperature that can be stably maintained by pumping on liquid He^4; the upper limit is determined by the point at which the signal is lost in the noise of our measuring apparatus. Over this range, the dominant temperature

dependence of the hc/e amplitude $\Delta G_{hc/e}$ is expected to come from the exponential dependence on $1/\ell_\phi$ in Eq. (2.33). If this is true, then a plot of $\log(\Delta G_{hc/e})$ as a function of L/ℓ_ϕ (where L is the length of one arm of the loop) should give a straight line with slope -1.

Figure 5.12 shows the zero to peak amplitude $\Delta G_{hc/e}$ of the hc/e oscillations for the ~0.5 μm (Sample RS8) and ~1.0 μm (Sample RS9) loops as a function of L/ℓ_ϕ. ℓ_ϕ here is inferred from the weak localisation MR of the co-deposited long wire (Sample RS16). The dependence of $\Delta G_{hc/e}$ on L/ℓ_ϕ in Fig. 5.12 appears to be exponential, but a least squares fit to the equation $\Delta G_{hc/e} \propto \exp(-\lambda L/\ell_\phi)$ gives $\lambda = 1.72$. The fall-off of $\Delta G_{hc/e}$ is thus faster than $\exp(-L/\ell_\phi)$; it appears that the other factors cannot be ignored and we must fit to the full theory.

The theoretical prediction for a single loop without measurement probes is given in Eq. (2.33). Not shown in Eq. (2.33) is a prefactor which determines the amplitude of the aperiodic conductance fluctuations and the hc/e oscillations. This prefactor was stated in Chapter 2 to be ~100 in units of $(e^2/h)^2$, much greater than the "universal" value of unity, a consequence of the periodic boundary conditions of the isolated loop. For a loop with probes, one expects this prefactor to be smaller, as the presence of the probes is to should reduce the amplitude of the oscillations.

Figure 5.13 shows the same data as Fig. 5.12 as a function of temperature. The solid lines give the values of $\Delta G_{hc/e}$ obtained by taking the square root of the correlation function

$$F_{hc/e} = C[\ell_T/L]^2[(3/4)(\ell_4/L)e^{-(2L/\ell_4)} + (1/4)(\ell_3/L)e^{-(2L/\ell_3)}] \qquad (5.2)$$

with ℓ_3 and ℓ_4 given by Eqs. (2.43) and (2.44). (Since the data are taken at magnetic fields at which the localisation contribution is suppressed, only the Diffuson

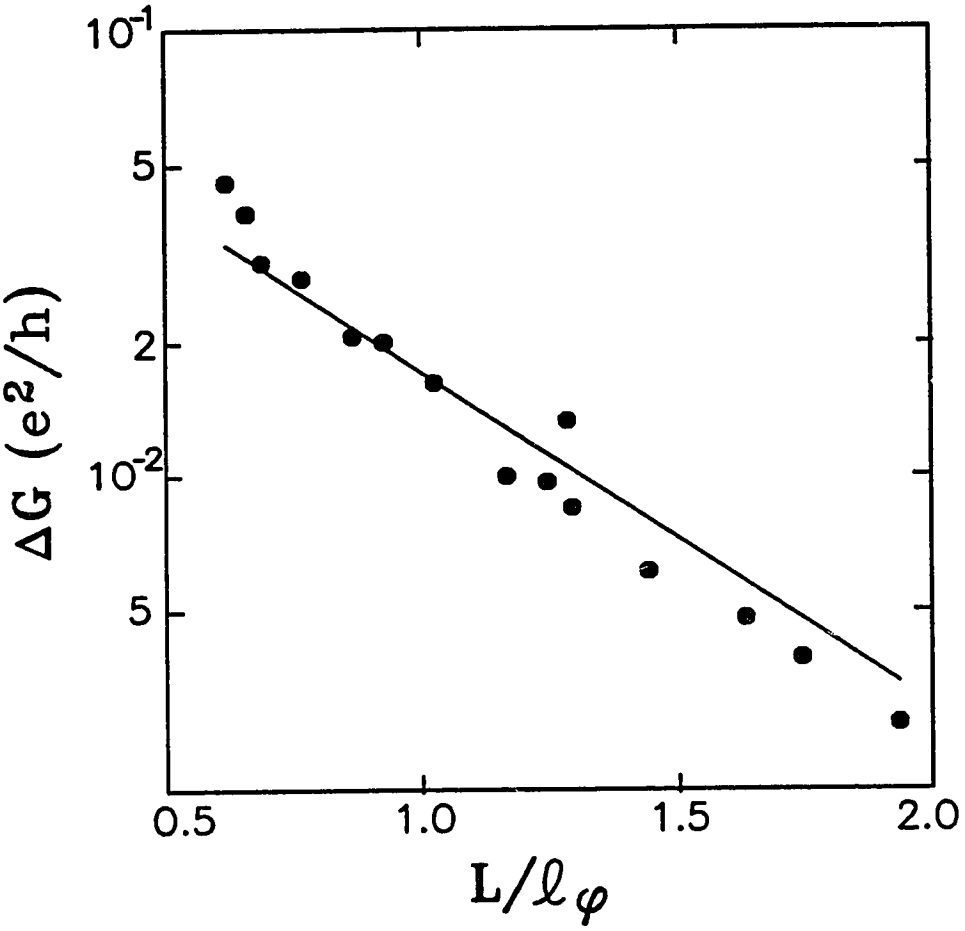

Figure 5.12. Zero to peak amplitude of the hc/e oscillations $\Delta G_{hc/e}$ for the ~0.5 μm (Sample RS8) and ~1.0 μm (Sample RS9) Al loops, as a function of L/ℓ_ϕ. Circles, data; solid line is the equation $\Delta G_{hc/e}=9.7\text{x}10^{-2}(e^2/h)\exp[-1.72(L/\ell_\phi)]$.

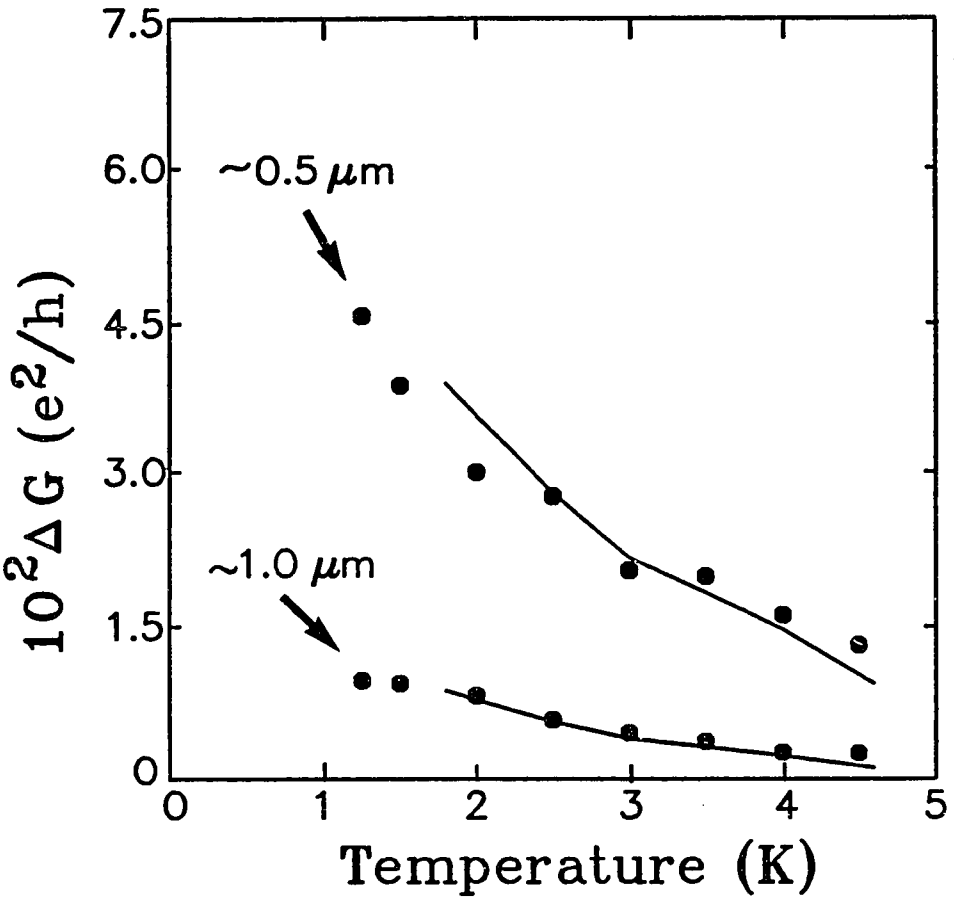

Figure 5.13. $\Delta G_{hc/e}$ for the Al loops RS8 (~0.5 μm) and RS9 (~1.0 μm) as a function of temperature. Circles, data; solid lines, fits to Eq. (5.2) with the parameters C=1.4 (for RS8) and C=1.5 (for RS9), using ℓ_ϕ inferred from the co-deposited long wire, RS16. Values of ℓ_ϕ at 1.25 and 1.5 K for the co-deposited long wire, Sample RS16, could not be obtained, since these temperatures were too close to the superconducting transition. See text for details.

contribution to the conductivity need be taken into account.) The only free parameter in these fits is C; the values of ℓ_ϕ and ℓ_{so} are determined from the co-deposited long wire, and ℓ_T is calculated from the diffusion constant. First, note that C for both the ~0.5 μm and ~1.0 μm loop is not ~100, as expected for the isolated loop, but ~1.5. This is closer to the value expected if the interference amplitude were completely suppressed at the probes. The measurement probes thus appear to have a strong affect on the amplitude of the hc/e oscillations. Second, in spite of the different dimensions of the two loops, the value of C for both of them is approximately the same (1.4 and 1.5). Similar values of C are found for other loops as well, if the correct phase breaking lengths are used. Although there is certainly some subjective bias in these values since C was chosen by fitting the data visually, the errors in these values would not change them by more than a factor of two. Thus C for the different loops is essentially the same. This is not surprising, since all the loops we have studied have similar probe configurations, so that the suppression of the hc/e amplitude due to the probes would be approximately the same. We should expect the suppression to be somewhat greater for smaller samples; from this point of view, the lower value of C obtained for the ~0.5 μm loop is suggestive, but the errors in our data and uncertainty in the analysis do not make this difference significant.

In the case of weak localisation, the amplitude of the hc/2e oscillations were found to be more sensitive to the probes than the amplitude of the background MR. For sample-specific effects, the quantity analogous to the weak localisation MR is the correlation function F(ΔH). F(ΔH) for a loop has a structure similar to the weak localisation MR of a loop: hc/e oscillations are superposed on a monotonic

background due to the aperiodic conductance fluctuations in the wire. In fact, the correlation function of Eq. (2.33) can be written in a form similar to the AAS formula

$$F(\Delta\phi) = C\left[\frac{\ell_T}{L}\right]^2 \frac{\ell_\phi}{L} \frac{\mathrm{sh}[2L/\ell_\phi]}{\mathrm{ch}[2L/\ell_\phi] - \cos(2\pi\Delta\phi/\phi_o)} \qquad (5.3)$$

where it is understood that ℓ_ϕ has a field dependence given by Eq. (2.11), with H replaced by $\Delta H/2$. It would be interesting to see if the amplitude of the hc/e oscillations in the correlation function of a loop are more sensitive to the probes than the amplitude of the aperiodic fluctuation background.

Figure 5.14 shows the field dependent correlation function of the ~1 μm Au loop, Sample SE2, at 1.25 K. The broad background is due to aperiodic conductance fluctuations. Superposed on this are oscillations of period ~70 gauss, corresponding to a flux of hc/e through the loop, which persist to a ΔH of >1 kG. The dashed line is a plot of Eq. (5.3) with the parameters $\ell_\phi = 1.58$ μm, $\ell_s = 1.2$ μm, and $\ell_{so} = 0.07$ μm. ℓ_ϕ was determined from the Nyquist formula, Eq. (2.39), and ℓ_s and ℓ_{so} were determined from weak localisation fits to the low field MR. The value of the prefactor C is determined self-consistently by requiring a match to the value of F at zero field; for these phase coherence lengths, C=27.3. This value of C should be compared to the value of 1.5 obtained by fitting only the amplitude of the hc/e oscillations for the same sample with the same parameters. It should therefore come as no great surprise that although the dashed line fits the general background of the correlation function, it greatly overestimates the amplitude of the oscillations. Smaller values of ℓ_ϕ give a reduced amplitude for the hc/e oscillations, but a larger value of C. The value C=27.3 is determined by the amplitude of the aperiodic conductance fluctuations, C=1.5 by the oscillations; both are to be compared to the isolated loop value of ~100. As in the

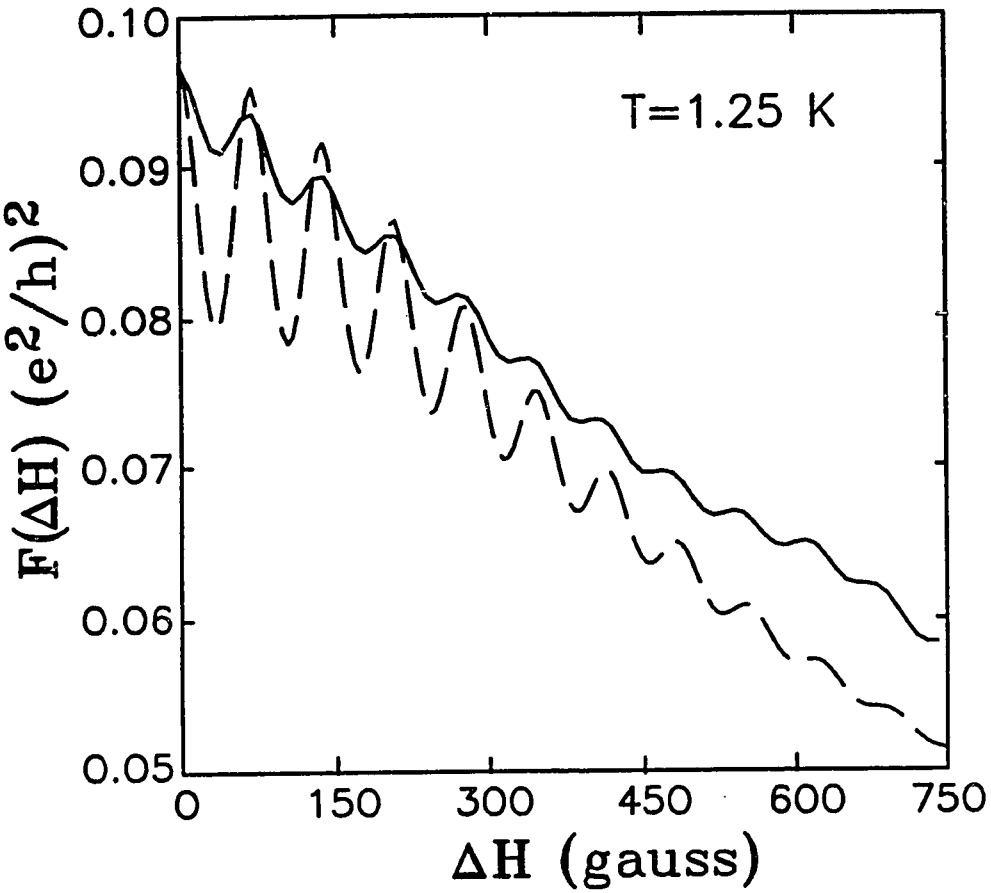

Figure 5.14. Correlation function F(ΔH) for Sample SE2, a ~1 μm Au loop. Solid line is data, dashed line is fit to Eq. (5.3) with ℓ_ϕ=1.58 μm, ℓ_s=1.2 μm, and ℓ_{so}=0.07 μm. C=27.3 for these parameters.

case of weak localisation, both the amplitude of the background aperiodic fluctuations and the amplitude of the hc/e oscillations are reduced in comparison to the isolated loop calculation, and the reduction in the amplitude of the oscillations due to the leads is greater than the reduction in the amplitude of the fluctuation background. Similar results are found in other samples.

5.3 Effect of Magnetic Scattering on the Aharonov-Bohm Effect

Figure 5.15 shows the MR of a 0.825 μm diameter circular Au loop from the IBM group, reproduced from Fig. 7a of Webb *et al.* [1985b]. Aperiodic conductance fluctuations and oscillations of period hc/e are seen, but what is remarkable about these data is the complete absence of any weak localisation contribution at low fields. Au films are known to have strong spin-orbit scattering, so that one would have expected a positive weak localisation MR at low fields. The magnitude of this weak localisation MR can be calculated from the parameters given in Webb *et al.* [1985]. In the absence of magnetic scattering, the major contribution to electron dephasing at 50 mK is from electron-electron scattering. (The contribution of electron-phonon scattering can be ignored at these temperatures.) ℓ_ϕ at 50 mK, calculated from the Nyquist formula, Eq. (2.39), works out to be 19.4 μm, giving an expected change in resistance due to weak localisation of $\Delta R \sim 0.7\ \Omega$, which is clearly not seen in the data. A more conservative estimate is obtained from the amplitude of the hc/e oscillations. $\Delta G_{hc/e} \sim e^2/h$, suggesting that ℓ_ϕ is at least as long as the distance from one voltage probe to another, 1.6 μm, giving a ΔR due to localisation of $\sim 0.06\ \Omega$. For the AAS hc/2e oscillations, there is an additional exponential factor which reduces the amplitude by about a factor of 2. These changes should be observable in the data,

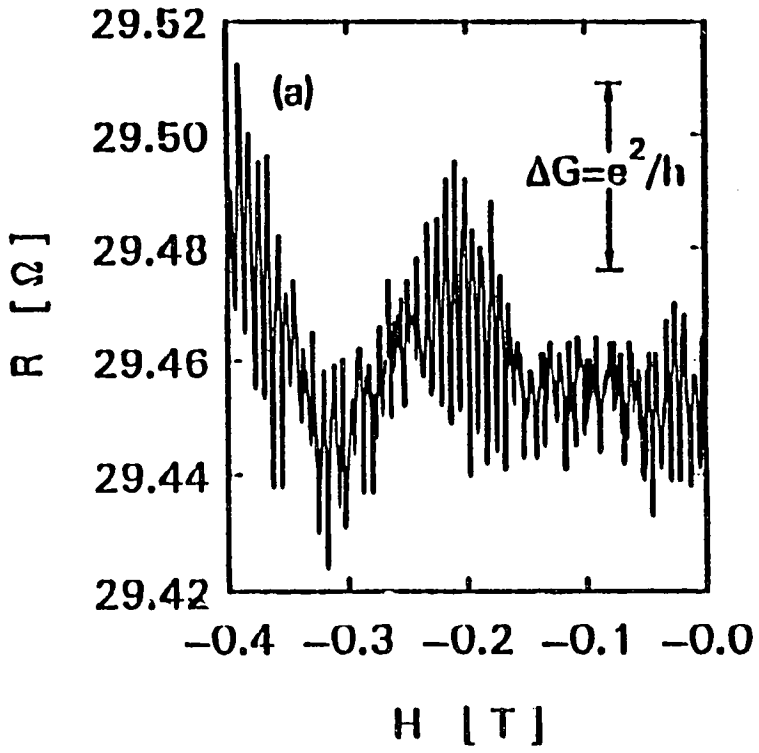

Figure 5.15. Magnetoresistance of a 0.825 μm diameter Au loop from the IBM group. From Fig. 7a of Webb *et al.*, [1985b].

but are not seen. This absence of weak localisation and AAS hc/e oscillations is ubiquitous in the IBM Au loops.

The absence of a weak localisation MR in the Au loop in Fig. 5.15 would indicate that ℓ_ϕ is very short. On the other hand, the amplitude of the hc/e oscillations suggests that ℓ_ϕ is at least $\sim$1.6 μm. Thus, it appears that the phase coherence lengths for the two effects are not the same. What could be the source of this difference? One possibility that we have investigated is that scattering by magnetic impurities possibly present in the IBM Au loops suppresses ensemble-averaged effects (such as weak localisation and the AAS oscillations) but does not affect sample-specific effects (conductance fluctuations and hc/e oscillations). Scattering by paramagnetic impurities is known to destroy the coherence required for weak localisation [Bergmann, 1982]; it is also expected to destroy sample-specific effects [Lee *et al.*, 1986], but this had not been verified experimentally at the time.

Not all Au loops in all laboratories show an absence of ensemble-averaged effects. The Yale Au loops show both weak localisation and AAS oscillations, so that the concentration of magnetic impurities in these loops must be small. One estimate of the number of magnetic impurities in the Yale Au loops is obtained from the weak localisation MR; another can be obtained from the resistance of the sample as a function of temperature. In addition to electron-phonon scattering, there are three contributions to the resistance at low temperatures: weak localisation, the Kondo effect, and electron-electron interactions. The weak localisation contribution can be eliminated by measuring the resistance as a function of temperature in a large magnetic field. The electron-electron contribution can be calculated from the relation [Altshuler and Aronov, 1985]

$$\Delta\sigma(T) = -9.82 \frac{1}{tW} \frac{e^2}{\pi\hbar} \ell_T \qquad (5.4)$$

which gives the conductivity correction at a temperature T for a system which is 1D with respect to ℓ_T. Here t and W are the thickness and the width of the 1D wire. For our samples (Sample SE2, for example), this gives an increase in resistivity of approximately 5.5 nΩ-cm in going from 10 K to 1 K. The experimentally observed increase in resistivity in our samples from 10 K to 1 K is roughly 7.5 nΩ-cm; thus, the contribution of the Kondo effect is an increase of ~2 nΩ-cm per decade of temperature. Experimentally, 1 ppm concentration of Fe impurities in Au leads to a resistivity rise of 1 nΩ-cm per decade of temperature [Heeger, 1969]. The concentration of Fe impurities in our samples therefore works out to be ~2 ppm. Using Eq. (2.49) for the spin-flip scattering time with S=2 gives ℓ_S=1.94 μm. Given the approximate nature of the calculation, this is in good agreement with the value of ℓ_S=1.2 μm inferred from weak localisation fits. Thus, it is not surprising that both conductance fluctuations and weak localisation are seen in the Yale Au films. If Fe impurities in the IBM Au films are suppressing the localisation effect, the concentration of such impurities must be much higher than a few ppm.

We have studied the effect of magnetic scattering on quantum interference by deliberately introducing magnetic impurities in a system which, in the absence of the added impurities, shows both ensemble-averaged and sample-specific effects [Chandrasekhar and Prober, 1987]. Ag loops, in the absence of magnetic impurities, show both hc/e and AAS hc/2e oscillations; Co was chosen as the magnetic impurity because it is relatively resistant to oxidation. The addition of the Co impurities is expected to suppress weak localisation; our aim was to see whether the hc/e oscillations were suppressed as well. The preparation of the Ag+Co films has been

described in detail in Chapter 3. To determine the appropriate amount of Co required, studies on 2D Ag+Co films were first carried out. It was found in the 2D films that ~0.01 atomic layers of Co on the surface of the Ag film resulted in a magnetic scattering length of ~0.2 μm as determined by analysing the weak localisation MR of the Ag+Co films. (The concentration of impurities was estimated from the rate and duration of the Co evaporation.) This concentration was used in our experiments.

Figure 5.16a shows the low field MR of Sample RR5, a ~1 μm Ag loop with added Co impurities, at 1.5 K. These data should be compared to the data for Sample RI13, a ~1 μm Ag loop without added Co impurities, shown in Fig. 5.5a. The background MR is negative in sign, indicating that $\ell_\phi < \ell_{so}$. A fit to this background using the long wire weak localisation theory without magnetic scattering gives an effective $\ell_\phi = 0.23$ μm and $\ell_{so} = 0.46$ μm, corresponding to $\ell_s = 0.32$ μm. Using these values in Eq. (5.2) with C = 1.5, the expected rms amplitude of the hc/e oscillations is 3.9×10^{-4} e^2/h. Figure 5.16b shows the MR of the same loop (Sample RR5) from 1-5 kG. The average zero to peak amplitude of the hc/e oscillations for this sample at 1.5 K is 6.7×10^{-3} e^2/h, more than an order of magnitude larger than the value predicted by theory. Note that in magnetic field in these data is small enough so that the Zeeman energy of the impurity spins is less than $k_B T$. Thus, paramagnetic spin scattering, if present, would not be suppressed by the magnetic field.

Figure 5.17 shows the zero to peak amplitude of the hc/e oscillations for another Ag loop with Co impurities, Sample RR7. $\Delta G_{hc/e}$ for this sample is approximately the same as that for the Al and Au loops in Figs. 5.13 and 5.14. The weak localisation MR of this sample does not change below 4.6 K, and fits to the long wire formula give $\ell_s = 0.5$ μm. The solid line shows the amplitude predicted by Eq. (5.2) using this

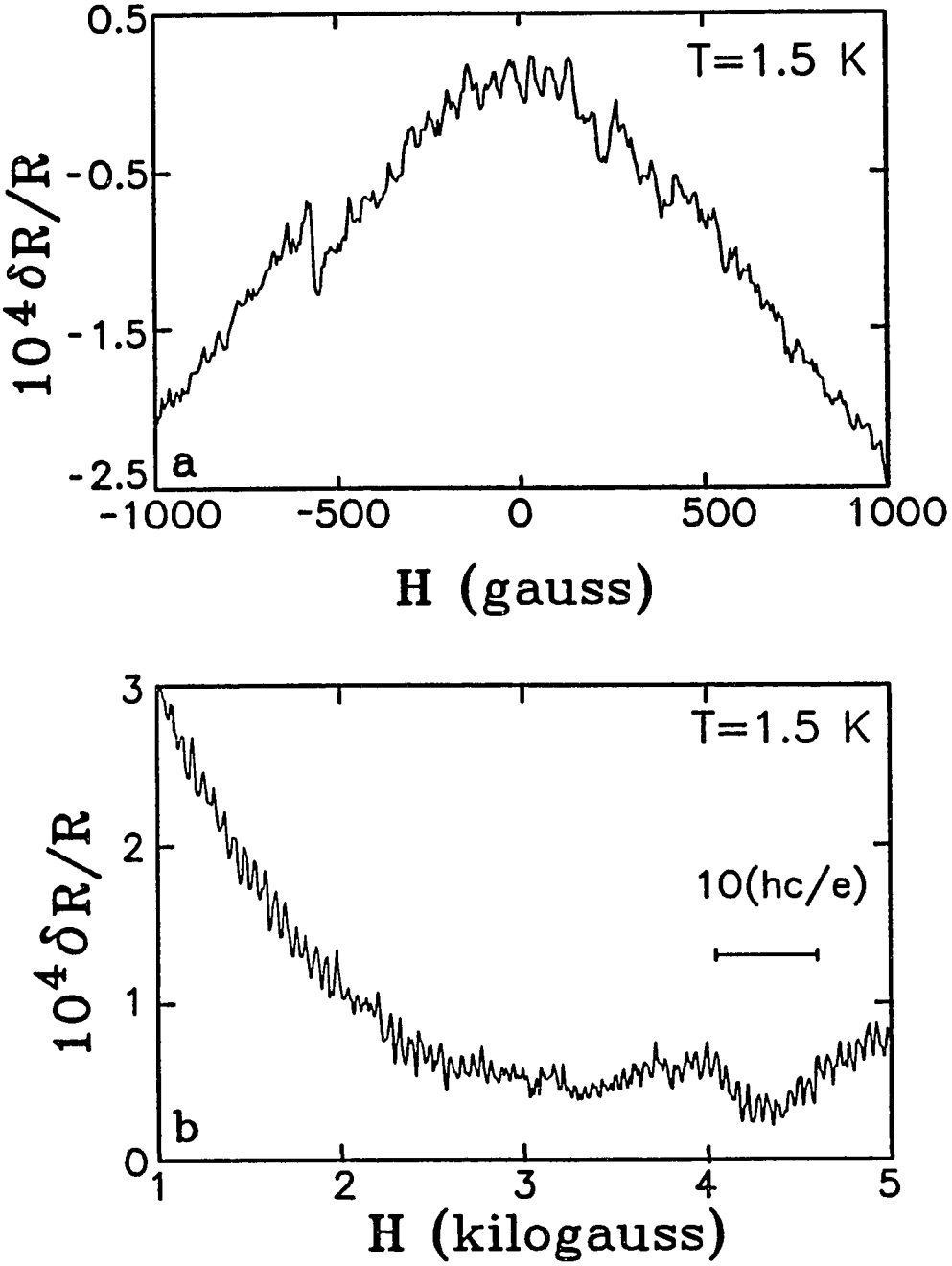

Figure 5.16. (a). Low field magnetoresistance of a ~1 μm Ag loop with Co impurities, Sample RR5, at 1.5 K. Oscillations of period hc/e are visible near zero field. (b). High field magnetoresistance of the same loop, showing clear hc/e oscillations.

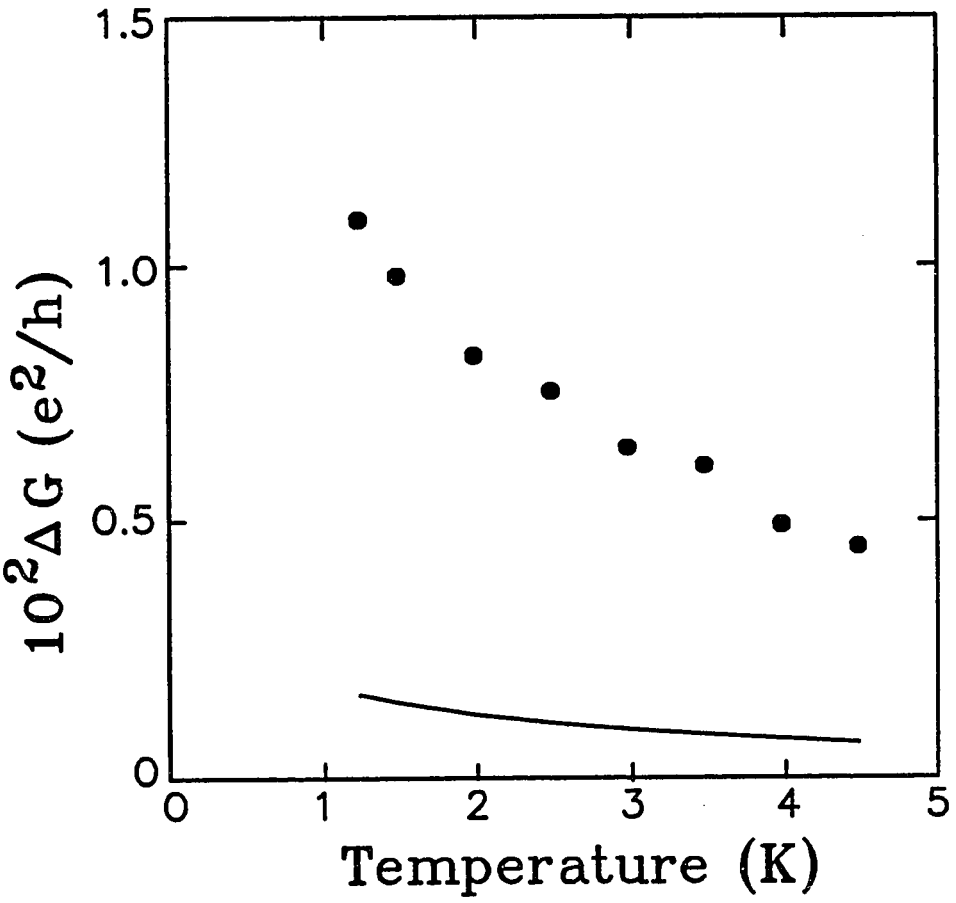

Figure 5.17. $\Delta G_{hc/e}$ for a ~1 μm Ag loop with Co impurities, Sample RR7, as a function of temperature. Circles, data; solid line, Eq. (5.2) with C=1.5.

value of ℓ_S, C=1.5 and the ℓ_ϕ predicted by the Nyquist theory, Eq. (2.39). As before, the theoretical curve grossly underestimates the amplitude of the oscillations.

Thus, it appears that with such magnetic scattering, ℓ_ϕ for weak localisation and the AAS hc/2e oscillations is not the relevant length scale for the hc/e oscillations. At first sight, this seems to contradict the predictions of the theory of Lee *et al.* [1986]. This theory predicts that scattering by *paramagnetic* impurities will destroy both ensemble-averaged and sample-specific effects. It is quite possible, however, that the surface Co impurities on the Yale Ag films are not isolated from one another, but are stuck together in small *ferromagnetic* clusters. These ferromagnetic clusters have associated with them large magnetic fields which penetrate into the Ag film. If these fields are static in time, they could destroy time-reversed interference processes like localisation, but not conductance fluctuations or hc/e oscillations. Then ℓ_ϕ for the sample specific processes would be much longer than ℓ_ϕ for weak localisation. It is our belief that a similar sort of dephasing occurs in the IBM loops as well.

A number of arguments support this interpretation. The Kondo temperature for the AgCo system, based on the data for the AuCo system, is expected to be ~500 K [Heeger, 1969]. If the Co impurities were indeed isolated, then their magnetic moments would be quenched at the temperatures at which the experiments were performed; thus, very little spin-flip scattering due to magnetic impurities would occur and the localisation contribution would not be suppressed. This argument is also valid for the IBM Au loops, where Fe is expected to be the most common dilute magnetic impurity [Kondo, 1969]. T_K for the AuFe system is ~0.8-1.0 K [Heeger, 1969]; at the lowest temperatures at which the experiments were performed (10-50 mK), spin-flip

scattering would be greatly suppressed. Further evidence comes from experiments on Au loops with ion-implanted Mn impurities [Benoit *et al.*, 1987] and Au loops dipped in cerium-magnesium-nitrate paramagnetic salt [Washburn and Webb, 1986]. The magnetic impurities in these samples, by virtue of their method of preparation, are isolated from one another. It was found that the hc/e oscillations in these samples were suppressed at low magnetic fields, but reappeared at higher magnetic fields, where spin-flip scattering is suppressed because the impurity spins are lined up with the field. Thus, scattering by isolated magnetic impurities cannot explain the experimental results on the Ag+Co and IBM Au loops. However, the difference in the phase coherence lengths for weak localisation and hc/e oscillations in the IBM samples must be due to a dephasing mechanism caused by magnetic impurities. No other dephasing mechanism we know differentiates between ensemble-averaged and sample-specific effects. These magnetic impurities may be introduced in the patterning of the IBM Au loops, which is done by contamination lithography. It is possible that this process introduces ordered clusters of magnetic impurities on the surface of the Au film. The similarity in the behaviour of the IBM Au loops and the Yale Ag+Co loops makes this a strong possibility.

6. Comparison to Other Work

Electron quantum interference in disordered metals has been an extremely popular topic of research in recent years. Early experimental work was directed towards verifying the prediction of Thouless [1977] of electron localisation in 1D metal wires; with the advent of the microscopic theory of weak localisation outlined in Chapter 2, attention turned to verifying the detailed predictions on weak localisation in 2D films and 1D wires, as well as the predictions for electron scattering rates in disordered metals. There are a number of excellent review articles which discuss both weak localisation and electron scattering rates in disordered metals (see, for example, Altshuler and Aronov [1985] for the theory, and Santhanam *et al.* [1987] for experiment; also recommended are the theses of Santhanam [1985] and Wind [1987]). More recently, experimental and theoretical work has dealt with conductance fluctuations and the Aharonov-Bohm effect in very small metal structures. A detailed treatment of the theory of conductance fluctuations can be found in Lee *et al.* [1986]; reviews of experimental work on conductance fluctuations and the Aharonov-Bohm effect are given in Washburn and Webb [1986], Washburn [1988], Kaplan and Hartstein [1988] and Aronov and Sharvin [1987].

In view of the large body of work in this field, we shall discuss in this chapter only those studies by other investigators which are directly relevant to the work in this thesis. The emphasis will be on experimental studies of mesoscopic systems with probes; an excellent review of the theoretical work on conductance fluctuations in mesoscopic samples with probes can be found in Stone and Szafer [1988]. We are

especially interested in studies which attempt to make a detailed *quantitative* comparison to theory, a major aim of this thesis. A central problem in the quantitative analysis of the experimental studies on conductance fluctuations and the Aharonov-Bohm effect has been the determination of the relevant electron scattering lengths, in particular ℓ_ϕ. Ideally, one would like an independent means of determining ℓ_ϕ. Generally, the only method available is to fit the low field MR to the theory of weak localisation; however, this method will not work if the weak localisation contribution is absent, as is the case with the IBM Au samples [Umbach *et al.*, 1984], or if it is swamped by larger aperiodic fluctuations, as in Si inversion layers [Skocpol *et al.*, 1987]. In these cases, ℓ_ϕ is not known with confidence. In metals where the weak localisation contribution is observed, as in the Sb samples of the IBM group, one has to be careful to take into account the effects of the measurement probes. As demonstrated in Chapters 4 and 5, ignoring the effects of the measurement probes will result in an incorrect (usually smaller) value of ℓ_ϕ. Most of the experiments were carried out before the theory of quantum interference in systems with probes was fully understood, and thus, the analysis given is not correct in view of our current understanding. We shall discuss a few of these experiments in detail below.

6.1 The Aharonov-Bohm Effect

Historically, it was the search for flux quantisation in normal-metal loops which initiated the study of electrical transport in mesoscopic systems. The first experiments on flux quantisation in disordered metal loops were unsuccessful [Skocpol *et al.*, 1984; Blonder *et al.*, 1984; Umbach *et al.*, 1984]. Instead of periodic

oscillations, only aperiodic conductance fluctuations were observed in these samples. The inability to observe Aharonov-Bohm oscillations in these experiments was due to the large aspect ratio (linewidth/diameter) of the loops. In a loop with a large aspect ratio, the period of the oscillations is of the same order as the characteristic field of the aperiodic conductance fluctuations [Stone, 1985], making the oscillations difficult to observe.

Subsequent attempts to observe the Aharonov-Bohm effect in disordered metals were more successful: Webb *et al.* [1985] observed hc/e oscillations in single Au loops; Chandrasekhar *et al.* [1985] observed AAS hc/2e oscillations in Al loops, and both hc/e and AAS hc/2e oscillations in Ag loops. hc/e oscillations were also seen in a GaAs quantum well device [Datta *et al.*, 1985]. With respect to this last experiment, it appears that the physics of the hc/e oscillations in GaAs devices is not the same as that in the disordered metals [Jain, 1988]. Electron transport in these devices is ballistic rather than diffusive, and the Aharonov-Bohm oscillations seen in this and more recent experiments in GaAs/AlGaAs devices [Timp *et al.*, 1987; Timp *et al.*, 1988] are attenuated at higher magnetic fields, in contrast to the hc/e oscillations in the metal loops.

6.1.1 Temperature Dependence of the Aharonov-Bohm Effect

Washburn *et al.* [1985] studied the temperature dependence of the hc/e Aharonov-Bohm in two Au loops of different diameters. They found that the amplitude of the hc/e oscillations for both loops saturated at the lowest temperatures; at higher temperatures, the amplitude for both loops was consistent with the power law $T^{-1/2}$, rather than the exponential dependence expected from Eq. (2.33). Although

they were unable to independently determine ℓ_ϕ due to the absence of a weak localisation contribution at low fields, they interpreted their results as evidence that ℓ_ϕ was much longer than the sample size at the lowest temperatures, but concluded that the detailed temperature dependence was not consistent with either energy averaging or weak localisation. This experiment, however, was performed before the theory of hc/e oscillations and the effect of measurement probes were properly understood. We believe that the temperature dependence they observed is a consequence of the effect of the probes on the amplitude of the hc/e oscillations. As ℓ_ϕ increases with decreasing temperature, the increase in the amplitude of the oscillations is partly offset by the greater influence of the probes, so that the exponential dependence is not seen. It would take a detailed calculation to see whether the effect of the probes does indeed result in a $T^{-1/2}$ dependence. Such a calculation would also have to take into account spin-orbit scattering, since Au is known to have strong spin-orbit scattering. To date, there is no calculation which gives detailed quantitative predictions enabling one to make direct comparison to experiment.

In another paper, Milliken *et al.* [1987] compared the phase coherence lengths obtained from analysing the weak localisation contribution and the amplitudes of the conductance fluctuations and hc/e oscillations in Sb loops of two different sizes. Sb was chosen because ℓ_ϕ is large and because Sb exhibits what appears to be weak localisation MR at low fields. ℓ_ϕ was determined by fitting the low field MR to the weak localisation formula of Santhanam [1987], Eq. (2.24). ℓ_ϕ inferred in this manner saturated at the lowest temperatures; the authors assumed this saturation was due to the presence of magnetic scattering, and refit the data using Eq. (2.41a) with a finite

value of ℓ_s. ℓ_ϕ from the aperiodic conductance fluctuations was obtained by fitting the fluctuation amplitude to Eq. (2.32); the prefactor in this equation was determined by matching the value of ℓ_ϕ to that obtained from the weak localisation fits at 0.5 K. ℓ_ϕ from the amplitude of the hc/e oscillations was obtained in a similar manner by fitting to the coefficient of the oscillatory part of Eq. (2.33) without the factor (ℓ_ϕ/L). The authors found remarkably good agreement between the values of ℓ_ϕ obtained by the different methods. They concluded that the aperiodic fluctuations diminish as a power law in L/ℓ_ϕ, while the hc/e Aharonov-Bohm oscillations vanish exponentially with increasing L/ℓ_ϕ, as expected from Eq. (2.33) (L is the length from one voltage probe to another).

Some of results from this experiment, however, can be subject to a different interpretation. First, although the Sb loops showed weak localisation at low fields, neither of the loops showed AAS hc/2e oscillations at any temperature [F. Milliken, private communication]. From the values of L/ℓ_ϕ quoted in the paper, AAS oscillations should have been observed. AAS hc/2e oscillations have been seen for similar values of L/ℓ_ϕ in other metals in the experiments performed at Yale. The absence of AAS oscillations raises the question as to whether the low field MR seen in the Sb loops is indeed due to weak localisation. Second, the authors assume a rather short value of ℓ_s in order to account for the saturation in the inferred values of ℓ_ϕ seen at low temperatures, although they state that there is no clear signature of magnetic scattering. The temperature dependence they obtain for ℓ_ϕ inferred in this manner ($\sim T^{-3/4}$) is inconsistent with recent studies on electron phase breaking in 1D wires [Santhanam *et al.*, 1987]. We think it more likely that the saturation is due to the effect of the measurement probes, which become important once $\ell_\phi > L$. The

correction formula of Santhanam, Eq. (2.24), is valid for a wire with four narrow measurement probes, when the length of the narrow measurement probes is at least $2\ell_\phi$. From the paper, it is not clear whether this condition holds at the lowest temperatures. If the narrow measurement probes are attached to larger 2D probes at distances shorter than ℓ_ϕ, one would expect to see a saturation. It is possible that this is the case since the dephasing lengths the authors infer saturate at a higher value for the larger loop than for the smaller loop (~2.0 μm for L=2.51 μm as opposed to 0.69 μm for L=1.64 μm); the actual value of ℓ_ϕ is probably much higher.

The remarkable agreement of the values of ℓ_ϕ inferred by the three different methods still requires an explanation. We think that this agreement arises because the measurement probes that reduce the amplitude of the weak localisation correction, resulting in a lower effective ℓ_ϕ, also reduce the amplitude of the sample-specific effects by a proportionate amount. Thus, one is able to fit the conductance fluctuations and the hc/e oscillations with the same effective ℓ_ϕ. It would be interesting to reanalyse the data from this experiment in light of our current understanding of the effect of measurement probes.

6.1.2 Effect of Magnetic Scattering

The effect of scattering by magnetic impurities on the amplitude of the hc/e effect has been investigated by Washburn and Webb [1986] and Benoit *et al.* [1987]. Webb and Washburn introduced magnetic impurities on the surface of their Au loops by dipping the loops into an alcohol solution of cerium-magnesium-nitrate, a well known paramagnetic salt. Benoit *et al.* ion-implanted 40 and 120 ppm of Mn into Au loops. Both studies found that the hc/e oscillations were suppressed at low magnetic

fields, but appeared at higher fields. They attributed the suppression of the hc/e oscillations at low fields to the increase in spin-flip scattering introduced by the magnetic impurities. As the magnetic field is increased, the impurity spins align with the field, the probability of spin-flip scattering is reduced, and the hc/e oscillations reappear. The temperature and magnetic field dependence of the amplitude of the oscillations were consistent with this picture. However, the Au loops in both studies did not show hc/2e oscillations prior to adding the paramagnetic impurities, so that some magnetic impurities must have been initially present in the samples. Nonetheless, the results of these experiments prove that scattering by paramagnetic impurities does indeed destroy the hc/e Aharonov-Bohm oscillations.

6.2 Short Wires

6.2.1 Weak Localisation

One of the earliest studies of quantum interference in 1D wires with probes was by Masden and Giordano [1982]. They measured the resistance of AuPd wires of length L=0.2-1.0 μm as a function of temperature. The wires connected two large Ag pads, as in the geometry of Fig. 2.6b. The low temperature resistance of such wires is expected to rise as the temperature is lowered, due to contributions from weak localisation and electron-electron interaction effects. The authors observed such a resistance increase, but found that the magnitude of the resistance rise was dependent on the length of the wire, being smaller for the shorter samples. They interpreted their results as implying that the length of the sample acted as a cut-off for ℓ_ϕ. Since the 1D weak localisation correction is proportional to ℓ_ϕ [Eq. (2.14)], this would imply a smaller correction for the shorter wires. However, due to a lack of

magnetoresistance data, they were not able to isolate the weak localisation contribution from the contribution of electron-electron interactions. In our way of thinking, the suppression of the quantum correction for the shorter wires is due to the greater influence of the 2D probes at small L/ℓ_ϕ. Masden and Giordano's results are consistent with this picture. Similar results were seen by Choi *et al.* [1986] in GaAs/AlGaAs heterostructures.

Bishop and Dolan [1985] measured weak localisation in long Li wires doped heavily at regular intervals L with Fe impurities. Since the magnetic Fe impurities should completely destroy phase coherence in the doped regions, the sample essentially consists of a series of short wires, each of length L. The authors measured wires with different values of L, and found that the size of the weak localisation correction was proportional to L. Like Masden and Giordano, they also interpreted their results in terms of an L dependent cut-off to ℓ_ϕ. Although the saturation observed was not related directly to the effect of measurement probes, their results can be described quite well by Eq. (2.22), with $\eta=\infty$. This value of η corresponds to the boundary condition $C(\mathbf{r},\mathbf{r}')=0$ at the ends of each segment of length L, a boundary condition induced by the complete phase randomisation caused by the Fe impurities at each doped region. A more recent study [Choi *et al.*, 1987] found a similar saturation in the weak localisation MR of 1D GaAs/AlGaAs heterostructures. In all the studies mentioned above, the data were analysed using the long wire weak localisation formula, the results being discussed in terms of an effective ℓ_ϕ which depends on sample length. The saturation in the MR seen in all the studies corresponds to the effect of the measurement probes on the magnitude of the MR seen in our wires. None of these studies, however, mention any effect on the shape of the MR, as was

seen in our samples.

6.2.2 Conductance Fluctuations

We have discussed some of the early experiments on aperiodic conductance fluctuations in metals in the section on the Aharonov-Bohm effect above. In addition to metals, aperiodic conductance fluctuations have also been investigated in Si MOSFETs [Licini *et al.*, 1985; Skocpol *et al.*, 1986; Kaplan and Hartstein, 1986] and GaAs heterostructures [Choi *et al.*, 1987; Taylor *et al.*, 1986; Ishibashi *et al.*, 1986]. In these semiconductor structures, unlike in the metal samples, $\ell_T \geq \ell_\phi$, so that they are nominally in the low temperature limit of the theory. The early studies on Si MOSFETs found conductance fluctuations of amplitude $\sim e^2/h$ both as a function of magnetic field and gate voltage [Licini *et al.*, 1985]. Skocpol *et al.* [1986] examined the detailed temperature dependence of the fluctuations, and found excellent agreement with the theory. Once again, however, ℓ_ϕ used in the analysis was not determined self consistently from the samples, but from earlier studies on 2D Si structures. Kaplan and Hartstein [1986] did attempt to determine ℓ_ϕ self-consistently from the low field MR of their samples. They found good agreement with the theory at 0.47 K, but did not attempt a detailed study of the temperature dependence. Taylor *et al.* [1986] found a $T^{-1/2}$ temperature dependence of the fluctuation amplitude in narrow GaAs wires, and interpreted this as coming from a $T^{-1/2}$ dependence of ℓ_ϕ. Thornton *et al.* [1987], on the other hand, determined ℓ_ϕ in GaAs/AlGaAs by fitting the amplitude of the conductance fluctuations to Eq. (2.31). They found that $\ell_\phi \propto T^{-1/3}$, consistent with Nyquist rate [Eq. (2.39)] for electron-electron scattering. Lastly, Ishibashi *et al.* [1986] found that the amplitude of the

conductance fluctuations in GaAs wires was essentially independent of temperature below 4.2 K. The conflicting results in GaAs samples illustrate some of the problems in analysing conductance fluctuations in semiconductors. One major problem is that there is yet no consensus on the temperature dependence of ℓ_ϕ in such samples. This knowledge is essential for a quantitative understanding of conductance fluctuations in semiconductors.

Two recent experiments have elegantly demonstrated the striking characteristics of electron transport in the mesoscopic regime. Umbach *et al.* [1987] measured two nominally identical 2 μm Au wires, each in a standard four-terminal configuration. One of the wires had attached to it a 0.7 μm diameter loop, such that the loop was outside the sample defined by the four probes. The single wire by itself showed only aperiodic conductance fluctuations, as expected, but the wire with the attached loop showed, in addition to the aperiodic fluctuations, oscillations of a period corresponding to a flux hc/e through the area of the loop, even though classically no current flowed through the loop. This experiment demonstrated beautifully the non-local nature of electron transport in the quantum regime. Since the loop is less than a phase coherence length away, the electrons in the wire can spend some time in the loop and still retain phase coherence on returning to the wire. Thus, measurement of phase coherent effects in the wire will show the presence of the loop, even though the loop is not being measured directly.

The second experiment dealt with the asymmetry in the magnetoresistance found in mesoscopic wires and loops. As we have seen, in a standard four-terminal measurement, the magnetoresistance of mesoscopic samples is in general neither symmetric nor antisymmetric. Benoit *et al.* [1986] found that the resistance of

mesoscopic samples is dependent on the arrangement of the probes. In any particular four-terminal arrangement, a combination of the longitudinal (G_{xx}) and transverse (G_{xy}) conductances is measured. When the voltage probes are far apart, the symmetric longitudinal conductance G_{xx} dominates the measurement. In the mesoscopic regime, however, both G_{xy} and G_{xx} exhibit conductance fluctuations of amplitude $\sim e^2/h$. Thus, a standard four-terminal measurement of the fluctuations, which measures a combination of both, will not be symmetric. By adding and subtracting the magnetoresistance traces measured with different probe arrangements in accordance with the four terminal conductance theory of Buttiker [1986], the authors were able to extract the purely symmetric and purely antisymmetric components.

Two other experiments also stress the importance of the measurement probes in mesoscopic samples. Benoit *et al.* [1987] measured conductance fluctuations in Au and Sb wires in the regime $L << \ell_\phi$, and found conductance fluctuations of amplitude much larger than "universal" value of e^2/h; in some cases, as large as 10^6 e^2/h. Similar results were found in narrow Si inversion layers by Skocpol *et al.* [1987]. These results are consistent with the interpretation that, regardless of the spacing L between the measurement probes, the sample being measured is always of size ℓ_ϕ. The amplitude at this length scale is $\Delta G_\phi \sim e^2/h$ [Stone and Szafer, 1988], corresponding to a resistance fluctuation of $\Delta R_\phi = R_\phi^2 \Delta G_\phi \sim \ell_\phi^2 e^2/h$. When $L < \ell_\phi$, the measured conductance fluctuation amplitude is $\Delta G = \Delta R_\phi / R^2 \sim (e^2/h)(\ell_\phi/L)^2$. Thus, when $L << \ell_\phi$, the measured ΔG can be much larger than e^2/h. These studies are a nice complement to our work on weak localisation in short wires. The conclusion one draws from all these studies is that, at least with present technology, one cannot

measure a mesoscopic sample without having the probes affect the measurement in some way.

7. Summary and Conclusions

The presence of quantum corrections to the classical resistance of a disordered metal arising from the coherent interference of electrons is now an established fact. Numerous experiments on thin films and wires have conclusively established that such quantum corrections do exist, and our understanding of these quantum corrections in *macroscopic* samples is now virtually complete. The major aim of this thesis has been to understand the results of experiments on quantum interference in *mesoscopic* samples. In this chapter, we summarise our results and the progress we have made towards this end.

7.1 Short Wires

7.1.1 Weak Localisation

Our experiments on weak localisation in short Ag wires with different probe geometries demonstrate that measurement probes strongly affect quantum interference in wires whose length is comparable to ℓ_ϕ. Experimentally, we find two specific effects of the probes. First, the measurement probes reduce the magnitude of the weak localisation MR of a short wire, in comparison to that of a long wire. This reduction is found to be greater in the short wires with larger probes. Second, the probes affect the qualitative shape of the weak localisation MR. This can be seen most clearly in the short wires with 2D probes, where the 2D nature of the probes appears directly in the low field MR of the wires.

These results obviously cannot be explained by the weak localisation theory for a

long 1D wire, which does not take into account the effect of measurement probes. We have extended the theory of weak localisation to describe short wires with both 1D and 2D probes. Fits to the experimental MR of our short wires using this theory are excellent, accounting for both the change in shape and the reduction in magnitude of the MR seen in the experiment. In addition, the phase coherence lengths inferred from these fits are in good agreement with those inferred from fits to the weak localisation MR of co-deposited long wires. Thus, we can now use the weak localisation MR of mesoscopic wires to self-consistently infer important phase coherence lengths.

7.1.2 Conductance Fluctuations

Our understanding of the effect of measurement probes on conductance fluctuations in mesoscopic wires is not as complete as it is for weak localisation. Experimentally, we find that the amplitude of the conductance fluctuations is smaller in wires with 2D probes than in wires with 1D probes, and that the characteristic field scale H_c is different for wires with different probe configurations. These results are consistent with our calculations of conductance fluctuations in wires with different probe configurations. In analogy to the case of conductance fluctuations, these calculations also show two specific effects of measurement probes. First, in agreement with our experiment, the amplitude of the fluctuations is smaller in wires with larger probes. Second, the shape of the conductance fluctuation correlation function $F(\Delta H)$ is dependent on the specific geometry of the measurement probes. Further theoretical work is required to extend these results to include the effects of energy averaging, which is important in most of our experiments on metal films.

From our experimental results, it is expected that the general trends mentioned above will still hold when energy averaging is taken into account, although the specific details may change.

We have pointed out the analogy between the weak localisation MR and the conductance fluctuation correlation function F(ΔH). The availability of a full quantitative finite temperature theory of conductance fluctuations which predicts the detailed form of F(ΔH) would enable one to use conductance fluctuations as a tool for determining electron phase coherence lengths, in much the same way as weak localisation is used today. Given a full theory, one could infer ℓ_ϕ and ℓ_{so} by fitting to the experimental F(ΔH). In general, due to the difficulty of the measurement and analysis required for conductance fluctuations, it is probably easier to use weak localisation, but conductance fluctuations would be useful in cases when, for some reason or the other, the weak localisation contribution is absent.

7.2 Single Loops

The early part of this work was directed towards observing the Aharonov-Bohm effect in single normal metal loops. We have been successful in observing oscillations of period hc/2e and hc/e in single loops of Al, Ag and Au. The magnetic field and temperature dependence of these oscillations is consistent with the picture of interference of time-reversed paths for the hc/2e oscillations, and non-time-reversed paths for the hc/e oscillations.

7.2.1 Effect of Measurement Probes

The MR of single loops is also found to be strongly affected by the measurement

probes. The MR of these loops has two components: an oscillatory component due to the doubly-connected nature of the loop, and a background MR due to the 1D wires which comprise the loop. We find that the the amplitudes of both the oscillations and the background MR are reduced compared to the values expected for an isolated loop, but that the reduction in the amplitude of the oscillations is greater than the reduction in the amplitude of the background MR. This applies to both the AAS hc/2e oscillations and the hc/e oscillations.

7.2.2 Electron Phase Coherence Lengths

A major part of our work on the Aharonov-Bohm effect has concentrated on the relevant length scales for the AAS hc/2e and hc/e oscillations. Based on previous work done at Yale and elsewhere, the effect of different electron dephasing mechanisms on ensemble-averaged effects such as weak localisation and the hc/2e Aharonov-Bohm effect was well known. However, due to some anomalous results obtained by the IBM group on conductance fluctuations and the hc/e Aharonov-Bohm effect in Au loops, there was some question about the effect of magnetic scattering on sample-specific effects.

This issue has now been clarified. We have extended the theory of conductance fluctuations to include the effect of spin-orbit scattering and scattering by paramagnetic impurities, introducing two new length scales, ℓ_3 and ℓ_4, which govern the singlet and triplet conductance fluctuation terms respectively. The inclusion of spin-dependent scattering in the theory is important for a detailed quantitative analysis of conductance fluctuations and the hc/e Aharonov-Bohm effect, as spin-dependent scattering will affect the temperature and magnetic field dependence of

these sample-specific effects.

In agreement with the predictions of Lee *et al.* [1986], we expect that, in the presence of spin-dependent scattering, the dephasing lengths for the hc/2e and the hc/e Aharonov-Bohm effects are the same, apart from some numerical constants. However, in our experiments, we found that the presence of a small number of magnetic Co impurities on the surface of an Ag loop suppressed the AAS hc/2e oscillations, but not the hc/e oscillations, thus demonstrating that, in the presence of such magnetic impurities, the dephasing lengths for the two effects can be different. We believe that this preferential suppression of the AAS hc/2e oscillations is due to the random magnetic fields generated by the impurity spins, which dephase the time-reversed interference required for the hc/2e oscillations, but do not affect the hc/e oscillations. In the absence of such magnetic impurities, the dephasing lengths for both effects should be the same, and oscillations of both periods should be observed in a *single* normal-metal loop. However, in the presence of *static* random magnetic fields, such as those that exist in a spin-glass, the dephasing lengths for the two effects can be drastically different.

One final point on phase coherence lengths. In Chapter 2, based on theoretical considerations, it was pointed out that one might expect the phase breaking length due to electron-electron interactions to be different for conductance fluctuations and weak localisation. This difference is expected to be small, however, and due to the large uncertainty in the quantitative predictions for conductance fluctuations, this question cannot be experimentally resolved at this time.

7.3 Conclusions

In the introduction to this thesis, we identified two problems which had made a quantitative analysis of quantum interference in mesoscopic systems difficult. The first was a lack of quantum interference formulae appropriate for mesoscopic systems. The second was a lack of an appropriate way to determine electron phase coherence lengths in mesoscopic samples. Our work on short metal wires has provided both an accurate quantitative description of weak localisation in mesoscopic systems and a means of determining electron phase coherence lengths self-consistently from data on mesoscopic samples. The formalism we have developed can be extended to describe loops and more complicated mesoscopic systems.

We still do not have a full quantitative understanding of conductance fluctuations and the hc/e Aharonov-Bohm effect in mesoscopic systems. Except for the calculations presented in this thesis, all the calculations on conductance fluctuations in wires with multiple probes done so far have been restricted to quasi-1D geometries. However, experimental samples quite frequently have 2D probes; we have seen that 2D probes have much larger effects on quantum interference than 1D probes. Furthermore, with the exception of the first calculations on short wires with two "perfect conductors" as probes (the "two-probe" calculations of Lee *et al.* [1986] and Altshuler and Khmelnitskii [1985]), these more recent multi-probe calculations do not take into account the effects of energy averaging. Most of the experiments on metal systems are in the finite temperature limit, where energy averaging is important. Thus, an extension of the theory is required.

Although our understanding of quantum interference in mesoscopic systems is not complete, it has progressed far enough for us to make at least one small suggestion

for the design of future experiments on quantum interference in mesoscopic systems. This suggestion is based on the knowledge that one cannot avoid the effect of measurement probes in mesoscopic systems. In the normal course of things, in measuring a small device, one is interested in obtaining as large a signal as possible. Knowing that large measurement probes will suppress the signal, one should strive to make the measurement probes as narrow as possible. In the future, it may be possible to fabricate devices with completely non-invasive probes. Until that point is reached, however, the measurement probe configuration with four narrow probes is the best.

Appendix I

Solution of the Diffusion Equation for the Cooperon in 2D

Let the plane of the 2D film be in the r, θ plane in a cylindrical co-ordinate system, with the magnetic field $\mathbf{H}=H\hat{z}$. With the cylindrical gauge $\mathbf{A}=(Hr/2)\hat{\theta}$, the homogenous part of Eq. (2.6) becomes

$$\left[-\frac{1}{r}\frac{\partial}{\partial r}\left[r\frac{\partial}{\partial r}\right] + \left[\frac{eH}{\hbar c}\right]^2 r^2 - \frac{1}{r^2}\frac{\partial^2}{\partial\theta^2} + 2i\left[\frac{eH}{\hbar c}\right] + \frac{1}{\ell_{\phi 2D}{}^2}\right] C(r,r') = 0. \qquad (AI.1)$$

Take the solutions to be of the form

$$C(r,\theta) = (1/2\pi)^{1/2}\, R(r)\, e^{im\theta} . \qquad (AI.2)$$

We are interested in the solutions with $m=0$. The equation for R(r) then becomes

$$\left[\frac{d^2}{dr^2} + \frac{1}{r}\frac{d}{dr} - \left[\frac{eH}{\hbar c}\right]^2 r^2 - \frac{1}{\ell_{\phi 2D}{}^2}\right] R = 0 . \qquad (AI.3)$$

Making the transformation $\xi=(eH/\hbar c)r^2$ and writing the solution for $R(\xi)$ as $R(\xi)=w(\xi)\exp(-\xi/2)$, we obtain an equation for $w(\xi)$

$$\left[\xi\frac{d^2}{d\xi^2} + (1-\xi)\frac{d}{d\xi} - \left(\frac{1}{2} + \frac{H_\phi}{H}\right)\right] w(\xi) = 0 , \qquad (AI.4)$$

where $H_\phi=(\hbar c/4e\ell_{\phi 2D}{}^2)$. The general solution of the equation above is in terms of the confluent hypergeometric functions [Lebedev, 1972]

$$w(\xi) = A\Phi[(1/2)+(H_\phi/H),1;\xi] + B\psi[(1/2)+(H_\phi/H),1;\xi] \qquad (AI.5)$$

where A and B are constants. Since $\Phi\to\infty$ as $\xi\to\infty$, we set $A=0$. Hence, the solution to Eq. (AI.1) is

$$C(r,r') = B\, \exp[-(eH/\hbar c)r^2]\, \psi[(1/2)+(H_\phi/H),1;(eH/\hbar c)r^2] \qquad (AI.6)$$

To determine the constant B, we must specify the boundary conditions. We would like to specify the boundary condition at r=0. However, this is not possible, because ψ diverges as r→0. This divergence is the same divergence that occurs in the calculation of the 2D weak localisation magnetoresistance. In that calculation, the problem is avoided by introducing a q space cutoff of $1/\ell$. In real space, this is equivalent to specifying the boundary condition at $r=\ell$. Setting $C(r,r')=C_a$ at $r=\ell$, we have

$$C_a = B \exp(-2H/H_o)\ \psi[(1/2)+(H_\phi/H),1;(H/4H_o)]. \qquad (AI.7)$$

Since $H/4H_o$ is small, we can take the small argument limit of the ψ function and set the exponential~1 to obtain

$$B = -\frac{\Gamma[(1/2)+(H_\phi/H)]C_a}{\{\ln(H/4H_o) + \Psi[(1/2)+(H_\phi/H)]\}}, \qquad (AI.8)$$

where Γ is the gamma function and Ψ is the digamma function.

To determine the constant η_1 of Eqs. (2.21) and (2.22), we need the limit as r→0 of C'(r,r'). Recalling that the limit of $\psi'(x,1;z)$ as z→0 is $-[x\Gamma(1)/\Gamma(x+1)z]$ we obtain as our final result

$$\lim_{r\to 0} C'(r,r') = \frac{2C_a}{r\{\ln(H/4H_o)+\Psi[(1/2)+(H_\phi/H)]\}}. \qquad (AI.9)$$

As H→0, this becomes $-(C_a/r)/[\ln(2\ell_{\phi 2D}/\ell)]$. The parameter η_1 is obtained from this by integrating over the angular co-ordinate, which, in our approximation, is equivalent to multiplying by $r\theta$, the arc subtended at radius r by an angle θ.

Appendix II

Amplitude of the hc/e Aharonov-Bohm Effect for a Single Isolated Loop

In this appendix, we shall follow the notation and calculation for a 1D wire in the review paper on conductance fluctuations by Lee *et al* (LSF) [1986].

We shall only consider the diagrams in Figs. 13a-d of LSF, as we are interested in the qualitative dependence of the correlation function on ℓ_ϕ and ℓ_T. Consider first the diagram in Fig. 13a of LSF. The correlation function is defined as (Eq. (A1) of LSF)

$$F_a = \left[\frac{1}{m^2 L_z^2}\right]^2 N_a \int dr_3 dr_4 dr_5 dr_6 (c_i u^2)^2 \; P(r_6,r_5)P(r_4,r_3) \times j(r_3,r_6)j(r_4,r_5), \qquad \text{(AII.1)}$$

where

$$j(r_1,r_2) = j_o \delta(r_1-r_2), \; j_o = 4\pi\tau^3 N(0) k_F^2/d. \qquad \text{(AII.2)}$$

With the substitutions, $\tau^{-1}=2\pi N(0)c_i u^2$ and $D=k_F^2\tau/m^2 d$, Eq. AII.1 becomes

$$F_a = [2/L_z^2]^2 N_a (D\tau)^2 \int dr_3 dr_4 \; P(r_3,r_4)P(r_4,r_3). \qquad \text{(AII.3)}$$

P is the Diffuson or Cooperon. For this calculation, we shall only consider the Diffuson. The calculation can be easiiy extended to the Cooperon. In the presence of a finite magnetic field difference ΔH and energy difference ΔE, P satisfies the diffusion equation

$$\{[i\nabla+(e/\hbar c)\Delta A]^2 - i(\Delta E/D)+\ell_\phi^{-2}\} \; P(r,r',\Delta E) = \delta(r-r')/D\tau, \qquad \text{(AII.4)}$$

where $\Delta H = \text{curl}(\Delta A)$. The corresponding equation for a Cooperon would have another term in the vector potential. Let the loop of radius a be in the r, θ plane of a cylindrical coordinate system and the magnetic field difference be in the z direction,

$\Delta H = \Delta H \hat{z}$. The normalised eigenfunctions of Eq. (AII.4) are $\psi_m(\theta) = (1/2\pi)^{1/2} \exp(im\theta)$, where m must be an integer for the eigenfunctions to be single-valued. Choosing the gauge $\Delta A = \Delta H a/2\ \hat{\theta}$ on the loop, Eq. (AII.4) becomes

$$\left[(i\frac{\partial}{\partial\theta} + \frac{\Delta\Phi}{\Phi_o})^2 - \frac{i\Delta E a^2}{D} + \frac{a^2}{\ell_\phi^2} \right] P(\theta,\theta',\Delta E) = \frac{a}{D\tau}\, \delta(\theta-\theta'), \qquad \text{(AII.4)}$$

where $\Delta\Phi = \Delta H \pi a^2$ is the magnetic flux through the loop and $\Phi_o = hc/e$ is the normal metal flux quantum. Expanding $P(\theta,\theta',\Delta E) = \Sigma \psi_m^*(\theta')\psi_m(\theta)/\lambda_m$, we obtain

$$\lambda_m = (D\tau/a)\{[m-(\Delta\Phi/\Phi_o)]^2 - i[\Delta E a^2/D] + (a^2/\ell_\phi^2)\}. \qquad \text{(AII.6)}$$

We now substitute this into Eq. (AII.3). There are two different P's in Eq. (AII.3), each which involves a sum over two different indices, say m and m'. On performing the integration over the two spatial coordinates, however, the orthogonality of the eigenfunctions ensures that only the terms with m=m' survive. Writing $L_z = \pi a/2$ and taking $N_a = 2$ as in LSF, Eq. (AII.3) becomes

$$F_a = 2(8/\pi^2)^2 \Sigma\, \lambda\!\!\!^{-}_m{}^{-2}$$

where $\lambda\!\!\!^{-}_m = (a/D\tau)\lambda_m$. If we take Figs. 13b-d of LSF into account as well, we have instead

$$F_a = 2(8/\pi^2)^2 \Sigma\, [1/\lambda\!\!\!^{-}_m + 1/\lambda\!\!\!^{-*}_m]^2 \qquad \text{(AII.7)}$$

where $\lambda\!\!\!^{-*}_m$ is the complex conjugate of $\lambda\!\!\!^{-}_m$. To evaluate the sum over m, we use the Poisson summation formula

$$S = \sum_{-\infty}^{\infty} f(m+1/2) = \int_{-\infty}^{\infty} f(x)dx + 2\sum_{s=1}^{\infty}(-1)^s \int_{-\infty}^{\infty} f(x)\cos(2\pi s x)dx.$$

For us

$$f(x) = \left[\frac{1}{\{x-[(\Delta\Phi/\Phi)+1/2]\}^2 - i(\Delta E a^2/D) + (a^2/\ell_\phi^2)} + cc \right]^2.$$

For the second integral in the Poisson summation formula, we make the substitution

$$x \to x + [(\Delta\Phi/\Phi_o)+1/2],$$

$$\cos\{2\pi s[x+(\Delta\Phi/\Phi_o)+1/2]\} \to \cos(2\pi sx)\cos\{2\pi s[(\Delta\Phi/\Phi_o)+1/2]\} - \sin(2\pi sx)\sin\{2\pi s[(\Delta\Phi/\Phi_o)+1/2]\}.$$

We can ignore the term involving the sines, since the function is even in x and sin(2πsx) is odd. The sum S then becomes

$$S = \int_{-\infty}^{\infty} g(x)dx + 2\sum_{s=1}^{\infty} \cos[2\pi sx(\Delta\Phi/\Phi_o)] \int_{-\infty}^{\infty} g(x)\cos(2\pi sx)dx,$$

where

$$g(x) = \left[\frac{1}{x^2-(i\Delta Ea^2/D)+(a^2/\ell_\phi{}^2)} + cc\right]^2.$$

The correlation function therefore oscillates as a function of the magnetic flux $\Delta\Phi$ with period Φ_o.

Let us first evaluate the zero temperature correlation function. For this, we can take $\Delta E=0$. The integrals can be found in Gradshteyn and Ryzhik [1980]. The correlation function at $T\to 0$ is then

$$F(\Delta\Phi) \sim \left[\frac{\ell_\phi}{\pi a}\right]^3 \left[1 + 2\sum_{s=1}^{\infty} (1+(2\pi sa/\ell_\phi))\exp[-(2\pi sa/\ell_\phi)] \times \cos[2\pi s(\Delta\Phi/\Phi_o)]\right]. \qquad \text{(AII.8)}$$

The first term is just the result for a 1D wire. The oscillatory terms are exponentially damped as a function of ℓ_ϕ, so we expect only the $s=1$ and perhaps the $s=2$ terms to be large enough to be observable. If we consider only the $s=1$ term, since $F\sim\exp[-(2\pi a/\ell_\phi)]$, the rms amplitude of the oscillations goes as $\exp[-(\pi a/\ell_\phi)]$.

For $T>0$, following LSF, we need to calculate

$$\bar{F}(T) = \frac{1}{k_BT}\int_0^{k_BT} d(\Delta E)\ F(\Delta E).$$

This involves the integral $\int g(x)d(\Delta E)$, with g(x) defined as before. To do this, we expand the square in g(x). The integrals over ΔE are not difficult. As it turns out, only the cross term gives a contribution which is appreciable. The integral over ΔE involving this term is

$$\frac{2}{k_BT}\int_0^{k_BT}\left[\frac{1}{[x^2+(a^2/\ell_\phi^2)]^2+[\Delta E a^2/D]^2}\right] d(\Delta E) =$$

$$2\left[\frac{(\ell_T^2/a^2)}{x^2+(a^2/\ell_\phi^2)}\right]\arctan\left[\frac{(a^2/\ell_T^2)}{x^2+(a^2/\ell_\phi^2)}\right].$$

Here ℓ_T is the thermal diffusion length. Now if $\ell_T << \ell_\phi$, arctan$\rightarrow\pi/2$. The integrals over x in the sum S can be done easily. The final result is

$$\bar{F}(\Delta\Phi,T) \sim \left[\frac{\ell_T}{\pi a}\right]^2\left[\frac{\ell_\phi}{\pi a}\right]\left[1 + 2\sum_{s=1}^{\infty}\exp[-(2\pi sa/\ell_\phi)]\cos[2\pi s(\Delta\Phi/\Phi_o)]\right]. \quad \text{(AII.9)}$$

As before, the first term is just the 1D wire result and the oscillations are exponentially damped with ℓ_ϕ. The terms that we have neglected in the square of g(x) give a contribution which goes as $\exp[-(2\pi a/\ell_T)]$. Since $\ell_T << 2\pi a$, this contribution is very small.

Appendix III

Effect of Spin-Dependent Scattering on Conductance Fluctuations

In this appendix, we evaluate the effect of spin-orbit scattering and scattering by paramagnetic impurities on conductance fluctuations. For this, we must evaluate the effect of spin-dependent scattering on the Diffuson and Cooperon. The difference between this calculation and equivalent one for weak localisation is that now we do not allow magnetic impurity scattering to connect the two lines in the Diffuson or Cooperon, since they refer to two different measurements and the impurity spin will not remain static between measurements. Normal elastic impurity scattering and spin-orbit scattering are allowed to connect the two lines, however, since we do not expect the corresponding potentials to change between the measurements.

In what follows, we shall consider only the Diffuson. The calculation for the Cooperon is, except for minor differences, identical, and gives an identical result. The total scattering potential is

$$U_{ss'}(k,k') = U + U_s S\cdot\sigma_{ss'} + iU_{so}(\hat{k}x\hat{k}')\cdot\sigma_{ss'}. \qquad \text{(AIII.1)}$$

The first term is the elastic scattering potential, the second the potential due to the impurity spin S and the third the spin-orbit potential. $\sigma_{ss'}$ refers to the Pauli spin matrix of the scattered electron, $\hat{k}$ is the wavevector of the incident electron and $\hat{k}'$ the wavevector of the scattered electron. The total scattering rate is given by

$$\tau^{-1} = 2\pi N(0)[\, U^2 + U_{so}^2 \Sigma|(\hat{k}x\hat{k}')_i|^2 + U_s^2 \Sigma\langle S_i^2\rangle \,]$$
$$= \tau_o^{-1} + \tau_{so}^{-1} + \tau_s^{-1}. \qquad \text{(AIII.2)}$$

N(0) is the electron density of states at the Fermi energy. A single part of the

impurity scattering potential in the particle hole ladder is given by

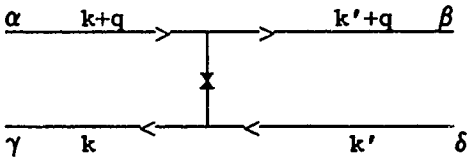

$F^{\alpha\beta}_{\gamma\delta}$

where the cross denotes the scattering potential *without* magnetic impurity scattering. F can be easily evaluated to give

$$F^{\alpha\beta}_{\gamma\delta} = [2\pi N(0)]^{-1}[(\tau_o^{-1})\delta_{\alpha\beta}\delta_{\delta\gamma} + (1/3)(\tau_{so}^{-1})\sigma_{\alpha\beta}\sigma_{\delta\gamma}] \qquad \text{(AIII.3)}$$

where we have assumed isotropic scattering. The factor 1/3 arises from the fact that we are not summing over the directions i of Eq. (AIII.2). The Diffuson is given by the series in Fig. 2.8c. This series can be written in matrix form

$$D = F + 2\pi N(0)\tau F(1 + i\omega\tau - Dq^2\tau)D,$$

where D is the diffusion coefficient. This can be rewritten as

$$2\pi N(0)\tau D = [F'^{-1} - (1 + i\omega\tau - Dq^2\tau)I]^{-1}, \qquad \text{(AIII.4)}$$

where $F'=2\pi N(0)\tau F$ and I is the unit matrix. Now since $\sigma_1\cdot\sigma_2=-2[J^2-s_1^2-s_2^2]$, where $s_{1,2}=(1/2)\sigma_{1,2}$ and $J=s_1-s_2$ (the minus sign is because one of the σ's refers to a hole), F' can be written in the J^2, s_1^2, s_2^2 representation as

$$F' = (\tau/\tau_o+\tau/\tau_{so})I - (2/3)(\tau/\tau_{so})J^2, \qquad \text{(AIII.5)}$$

so that the singlet and triplet matrix elements are given by

$$F'^0 = (\tau/\tau_o) + (\tau/\tau_{so}) = 1 - (\tau/\tau_s), \qquad \text{(AIII.6a)}$$

$$F'^1 = 1 - (\tau/\tau_s) - (4/3)(\tau/\tau_{so}). \qquad \text{(AIII.6b)}$$

The corresponding matrix elements for D are

$$D^0 = [2\pi N(0)\tau^2]^{-1}[-i\omega + Dq^2 + (\tau_s^{-1})]^{-1}, \qquad \text{(AIII.7a)}$$

$$D^1 = [2\pi N(0)\tau^2]^{-1}[-i\omega + Dq^2 + (\tau_s^{-1}) + (4/3)(\tau_{so}^{-1})]^{-1}. \qquad \text{(AIII.7b)}$$

The diagrams for the correlation function involve products of two Diffusons or two Cooperons. To see which matrix elements are allowed by spin conservation, we should transform the matrix **D** into the s_1, s_{1z}, s_2, s_{2z} representation. In this representation, the matrix **D** is

$$\mathbf{D} = \begin{vmatrix} (D^0+D^1)/2 & 0 & 0 & (D^0-D^1)/2 \\ 0 & D^1 & 0 & 0 \\ 0 & 0 & D^1 & 0 \\ (D^0-D^1)/2 & 0 & 0 & (D^0-D^1)/2 \end{vmatrix}$$

Labelling the spin indices by $<\alpha\beta\gamma\delta>$, the only matrix elements that contribute to conductance fluctuations are $<++++>=<---->=[(D^0+D^1)/2]^2$, $<++-->=<--++>=[(D^0-D^1)/2]^2$, and $<+-+->=<-+-+>=(D^1)^2$. Summing all six contributions gives us $3(D^1)^2+(D^0)^2$. The appropriate length scales for D^0 and D^1 are

$$D^0: \quad \ell_3^{-2} = \ell_\phi^{-2} + \ell_s^{-2}, \tag{AIII.8a}$$

$$D^1: \quad \ell_4^{-2} = \ell_\phi^{-2} + \ell_s^{-2} + (4/3)\ell_{so}^{-2}. \tag{AIII.8b}$$

In the absence of spin-dependent scattering, $D^1=D^0$ and the total contribution is $4(D^0)^2$. The Cooperon contribution is also split into a singlet and a triplet part, with the length dependence of C^0 given by ℓ_3 and that of C^1 by ℓ_4. Thus, strong magnetic impurity scattering will destroy the conductance fluctuations, whereas strong spin-orbit scattering will reduce their amplitude to a quarter.

Appendix IV

Fabrication Process for Small Devices

Spin Resist

1. Spin 185K molecular weight (MW) PMMA (~3% by weight in xylene) on oxidised Si wafer at 2500 RPM for 1 minute.
2. Bake at 185° C for 1 hour.
3. Spin ~3% (in xylene) 450K MW PMMA at 8000 RPM for 1 minute.
4. Bake at 185° C for 2 hours.

Pattern

1. Expose deep ultra-violet (DUV) mask (Fig. 3.2) in HTG mask aligner for 15 minutes.
2. Develop by soaking in MIBK:IPA 1:3 solution at 23.5° C for 30 seconds.
3. Expose individual dies using electron-beam mask.
4. Develop by squirting MIBK:IPA 1:3 solution at 23.5° C from wash bottle for 30 seconds.

Metal Evaporation and Liftoff

1. Evaporate metal at ~0.5 nm/sec.
2. Soak in acetone for 1 hour.
3. Squirt acetone from wash bottle or syringe. Repeat soak if necessary.
4. Store samples immediately under liquid nitrogen.

References

Abrahams, E., P.W. Anderson, P.A. Lee, and T.V. Ramakrishnan, Phys. Rev. **B 24**, 6783 (1981).

Abrikosov, A.A., and L.P. Gorkov, Sov. Phys. JETP **8**, 1090 (1959); Sov. Phys. JETP **9**, 220 (1959).

Abrikosov, A.A., and L.P. Gorkov, Sov. Phys. JETP **15**, 752 (1962).

Abrikosov, A.A., L.P. Gorkov, and I.E. Dzyaloshinski, *Methods of Quantum Field Theory in Statistical Physics*, Dover (1975).

Adler, J.G., and J.E. Jackson, Rev. Sci. Instrum. **37**, 1049 (1966).

Aharonov, Y, and D. Bohm, Phys. Rev. **115**, 485 (1959).

Alexander, J.A.X., P.M. Tedrow, and T.P. Orlando, Phys. Rev. **B 34**, 8157 (1986).

Altshuler, B.L., Pis'ma Zh. Eksp. Teor. Fiz. **41**, 530 (1985) [JETP Lett. **41**, 648 (1985)].

Altshuler, B.L., and A.G. Aronov, Zh. Eksp. Teor. Fiz. **75**, 1610 (1978) [Sov. Phys. JETP **48**, 812 (1978)]

Altshuler, B.L., and A.G. Aronov, Pis'ma Zh. Eksp. Teor. Fiz. **30**, 514 (1979) [JETP Lett. **30**, 482 (1979)].

Altshuler, B.L., and A.G. Aronov, Pis'ma Zh. Eksp. Teor. Fiz. **33**, 515 (1981) [JETP Lett. **33**, 499 (1981)].

Altshuler, B.L., and A.G. Aronov, chapter in *Electron-Electron Interactions in Disordered Systems*, Eds., V.M. Agranovich and A.A. Maradudin (North Holland, 1985).

Altshuler, B.L., and D.E. Khmelnitskii, Pis'ma Zh. Eksp. Teor. Fiz. **42**, 291 (1985) [JETP Lett. **42**, 359 (1985)].

Altshuler, B.L., D.E. Khmelnitskii, A.I. Larkin, and P.A. Lee, Phys. Rev. **B 22**, 5142 (1980).

Altshuler, B.L., A.G. Aronov, and B.Z. Spivak, Pis'ma Zh. Eksp. Teor. Fiz. **33**, 101 (1981) [JETP Lett. **33**, 94 (1981)].

Altshuler, B.L., A.G. Aronov, and D.E. Khmelnitskii, J. Phys. **C 15**, 7367 (1982a).

Altshuler, B.L., A.G. Aronov, and D.E. Khmelnitskii, "Coherent Effects in Disordered Conductors," chapter in *Quantum Theory of Solids*, Ed. I.M. Lifshits, Mir Publishers,

Moscow (1982b).

Altshuler, B.L., A.G. Aronov, B.Z. Spivak, D.Yu. Sharvin, and Yu.V. Sharvin, Pis'ma Zh. Eksp. Teor. Fiz. **35**, 476 (1982) [JETP Lett. **35**, 588 (1982c)].

Altshuler, B.L., A.G. Aronov, and A. Yu. Zyuzin, Zh. Eksp. Teor. Fiz. **86**, 709 (1984) [Sov. Phys. JETP **59**, 415 (1984)].

Altshuler, B.L., V.E. Kratsov, and I.V. Lerner, Pis'ma Zh. Eksp. Teor. Fiz. **43**, 342 (1986) [JETP Lett. **43**, 441 (1986)].

Aronov, A.G., Physica **126B**, 314 (1984).

Aronov, A.G., and Yu. V. Sharvin, Rev. Mod. Phys. **59**, 755 (1987).

Ashcroft, N.W., and N.D. Mermin, *Solid State Physics*, (Holt, Rinehart and Winston, 1976).

Aslamazov, L.G., and A.I. Larkin, Fiz. Tverdogo Tela **10**, 1104 (1968) [Soviet Physics-Solid State **10**, 875 (1968)].

Baranger, H.U., A.D. Stone, and D.P. DiVincenzo, Phys. Rev. **B 37**, 6521 (1988).

Belitz, D. and S. Das Sarma, Phys. Rev. **B 36**, 7701 (1987).

Benoit, A.D., S. Washburn, C.P. Umbach, R.B. Laibowitz, and R.A. Webb, Phys. Rev. Lett. **57**, 1765 (1986).

Benoit, A., C.P. Umbach, R.B. Laibowitz, and R.A. Webb, Phys. Rev. Lett. **58**, 2343 (1987).

Benoit, A., S. Washburn, C.P. Umbach, R.A. Webb, D. Mailly, and L. Dumoulin, *Proceedings of the International Symposium on Anderson Localization*, Tokyo, Japan, August 1987 [Springer-Verlag, 1988].

Bergmann, G., Phys. Rev. **B 3**, 3797 (1971).

Bergmann, G., Phys. Rev. Lett. **49**, 162 (1982).

Bergmann, G., Phys. Rep. **107**, 1 (1984).

Bergmann, G., Phys. Rev. Lett. **57**, 1460 (1986).

Bishop, D.J., and G. Dolan, Phys. Rev. Lett. **55**, 2911 (1985).

Blonder, G., Bull. Am. Phys. Soc. **29**, 535 (1984).

Bloomfield, P.E., and D.R. Hamann, Phys. Rev. **164**, 856 (1967).

Buttiker, M., Phys. Rev. Lett. **57**, 1761 (1986).

Buttiker, M., Phys. Rev. **B 35**, 4123 (1987).

Caeci, M.S., and W.P. Cacheris, BYTE Magazine **9**, 341 (1984).

Callen, H.B., and T.A. Welton, Phys. Rev. **83**, 34 (1951).

Castellani, C., C. DiCastro, G. Kotliar, and P.A. Lee, Phys. Rev. Lett. **56**, 1179 (1986).

Chandrasekhar, V. and D.E. Prober, *Proceedings of the 18th International Conference on Low Temperature Physics*, Kyoto, 1987 [Jpn. J. Appl. Phys. **26**, Supplement 26-3 (1987)].

Chandrasekhar, V., M.J. Rooks, S. Wind, and D.E. Prober, Phys. Rev. Lett. **55**, 1610 (1985).

Chandrasekhar, V., D.E. Prober, and P. Santhanam, Phys. Rev. Lett. **61**, 2253 (1988).

Choi, K.K., D.C. Tsui and S.C. Palmateer, Phys. Rev. **B 33**, 8216 (1986).

Choi, K.K., D.C. Tsui and K. Alavi, Phys. Rev. **B 36**, 7751 (1987).

Dalrymple, B.J., Ph.D. Thesis, Yale University (1983).

Datta, S., M.R. Melloch, S. Bandyopadhyay, R. Noren, M. Vaziri, M. Miller, and R. Reifenberger, Phys. Rev. Lett. **55**, 2344 (1985).

Daybell, M.D., "The s-d Model and the Kondo Effect: Thermal and Transport Properties," chapter in *Magnetism*, vol. V, Ed. H. Suhl, (1973).

DiVincenzo, D.P., and C.L. Kane, Phys. Rev. **B 38**, 3006 (1988).

Doucot, B., and R. Rammal, Phys. Rev. Lett. **55**, 1148 (1985); J. Physique **47**, 973 (1986).

Eiler, H., J. Low Temp. Phys. **56**, 481 (1984).

Feng, S., P.A. Lee , and A.D. Stone, Phys. Rev. Lett. **56**, 1960 (1986).

Feuer, M.D., and D.E. Prober, IEEE Trans. on Elec. Dev. **28**, 1375 (1981).

Fukuyama, H. and E. Abrahams, Phys. Rev. **B 27**, 5976 (1983).

Gershenzon, M.E., V.N. Gubankov, and Yu.E. Zhuravlev, Pis'ma Zh. Eksp. Teor. Fiz. 35, 467 (1982) [JETP Lett. **35**, 576 (1982)].

Gijs, M., C. Van Haesondonck, and Y. Bruynseraede, Phys. Rev. Lett. **52**, 2069 (1984a).

Gijs, M., C. Van Haesondonck, and Y. Bruynseraede, Phys. Rev. **B 30**, 2964 (1984b).

Giordano, N, W. Gilson, and D.E. Prober, Phys. Rev. Lett. **43**, 725 (1979).

Gordon, J.M., Phys. Rev. **B 30**, 6770 (1984).

Gordon, J.M., C.J. Lobb, and M. Tinkham, *Proceedings of the International Conference on Localization, Interaction, and Transport Phenomena in Impure Metals*, Braunschweig, September 1984.

Gorkov. L.P., A.I. Larkin, and D.E. Khmelnitskii, Pis'ma Zh. Eksp. Teor. Fiz. **30**, 248 (1979) [JETP Lett. **30**, 228 (1979)].

Gradshteyn, I.S., and I.M. Ryzhik, *Table of Integrals, Series, and Products*, (Academic Press, Orlando, Florida, 1980).

Hamann, D.R., Phys. Rev. **158**, 570 (1967).

He, S., and J.D. Maynard, Phys. Rev. Lett. **57**, 3171 (1986).

Heeger, A.J., "Localized Moments and Nonmoments in Metals, The Kondo Effect," chapter in *Solid State Physics*, vol. 23, Eds. F. Seitz and D. Turnbull, (1969).

Hershfield, S, and V. Ambegaokar, Phys. Rev. **B 38**, 7909 (1988).

Hikami, S., A.I. Larkin, and Y. Nagaoka, Prog. Theor. Phys. **63**, 707 (1980).

Howard, R.E., and D.E. Prober, "Nanometer-Scale Fabrication Techniques," from *VLSI Electronics: Microstructure Science*, vol. 5 (Academic Press, New York, 1982).

Imry, Y. "Physics of Mesoscopic Systems," chapter in *Directions in Condensed Matter Physics*, G. Grinstein and E. Mazenko, Eds., World Publishing Co., Singapore (1986).

Isawa, Y, H. Ebisawa, and S Maekawa, J. Phys. Soc. Jpn. **55**, 2523 (1986).

Ishibashi, K., K. Nagata, S. Ishida, K. Gamo, Y. Aoyagi, M. Kawabe, K. Murase, and S. Namba, "Quantum Interference Effect in Narrow n+-GaAs Wires," preprint (1986).

Israeloff, N.E., and M.B. Weismann, "Electrical Noise from Spin Glass Fluctuations," preprint (1988).

Jain, J.K., Phys. Rev. Lett. **60**, 2074 (1988).

Kane, C.L., P.A. Lee, and D.P. DiVincenzo, Phys. Rev. **B 38**, 2995 (1988).

Kaplan, S.B., and A. Hartstein, Phys. Rev. Lett. **56**, 2403 (1986).

Kaplan, S.B., and A. Hartstein, IBM J. Res. Develop. **32**, 347 (1988).

Kaplan, S.B., CC. Chi, D.N. Langenberg, J.J. Chang, S. Jafarey, and D.J. Scalapino, Phys. Rev. **B 14**, 4854 (1976).

Keck, B., and A. Schmid, J. Low Temp. Phys. **24**, 611 (1976).

Khmelnitskii, D.E., Physica **126B**, 235 (1984).

Kondo, J., Prog. Theor. Phys. **32**, 37 (1964).

Kondo, J., "Theory of Dilute Magnetic Alloys," chapter in *Solid State Physics*, vol. 23, Eds. F. Seitz and D. Turnbull (1969).

Landau, L.D., and E.M. Lifshitz, *Quantum Mechanics*, Volume 3 of *A Course of Theoretical Physics*, Pergamon Press (1977).

Larkin, A.I., Pis'ma Zh. Eksp. Teor. Fiz. **31**, 239 (1980) [JETP Lett. **31**, 219 (1980)].

Lawrence, W.E., and A.B. Meador, Phys. Rev. **B 18**, 1154 (1978).

Lebedev, N.N., *Special Functions and Their Applications*, (Dover Publications, New York, 1972).

Lee, P.A., and T.V. Ramakrishnan, Rev. Mod. Phys. **57**, 287 (1984).

Lee, P.A., and A.D. Stone, Phys. Rev. Lett. **55**, 1622 (1985).

Lee, P.A., A.D. Stone, and H. Fukuyama, Phys. Rev. **B35**, 1039 (1986).

Licini, J.C., D.J. Bishop, M.A. Kastner, and J. Melngailis, Phys. Rev. Lett. **55**, 2987 (1985).

Lopes dos Santos, J.M.B., Phys. Rev. **B 28**, 1189 (1983).

Ma, M., and P.A. Lee, Phys. Rev. **B 35**, 1448 (1987).

Maekawa, S., and H. Fukuyama, J. Phys. Soc. Jpn. **8**, 2516 (1981).

Maekawa, S., Y. Isawa, and H. Ebisawa, J. Phys. Soc. Jpn. **56**, 25 (1987).

Mackie, S., and S.P. Beaumont, Solid State Technol. **28**, 117 (1985).

Maki, K., Prog. Theor. Phys. **39**, 897, (1968).

Masden, J.T., and N. Giordano, Phys. Rev. Lett. **49**, 819 (1982).

Milliken, F.P., S. Washburn, C.P. Umbach, R.B. Laibowitz, and R.A. Webb, Phys. Rev. B **36**, 4465 (1987).

Pannetier, B., J. Chaussy, R. Rammal, and P. Gandit, Phys. Rev. Lett. **53**, 718 (1984).

Peters, R.P., G. Bergmann, and R.M. Mueller, Phys. Rev. Lett. **58**, (1987).

Pippard, A.B., Philos. Mag. **46**, 1104 (1955).

Prober, D.E., M.D. Feuer, and N. Giordano, Appl. Phys. Lett. **37**, 94 (1980).

Rammer, J., and A. Schmid, Phys. Rev. **B 34**, 1352 (1986).

Rickayzen, G., *Green's Functions and Condensed Matter*, Academic Press (1980).

Rooks, M.J., Ph. D. Thesis, Yale University (1987).

Rooks, M.J., S. Wind, P. McEuen, and D.E. Prober, J. Vac. Sci. Technol. **B 5**, 318 (1987.

Santhanam, P., Ph.D. Thesis, Yale University (1985).

Santhanam. P., Phys. Rev. **B 35**, 8737 (1987).

Santhanam, P., "Weak Localization in Normal Metal Loops: Influence of Boundary Conditions," preprint (1988).

Santhanam, P., S. Wind, and D.E. Prober, *Proceedings of the Seventeenth International Conference on Low Temperature Physics*, North Holland (1984).

Santhanam, P., S. Wind, and D.E. Prober, Phys. Rev. **B 35**, 3188 (1987).

Schmid. A., Z. Phys. **271**, 251 (1974).

Serota, R.A., S. Feng, C. Kane, and P.A. Lee, Phys. Rev. **B 36**, 5031 (1987).

Sharvin, D.Yu., and Yu.V. Sharvin, Pis'ma Zh. Eksp. Teor. Fiz. **34**, 285 (1982) [JETP Lett. **34**, 272 (1982)].

Skocpol, W.J., L.D. Jackel, R.E. Howard, P.M. Mankiewich, R.E. Behringer, L.A. Fetter, and D.M. Tennant, in *Proceedings of the International Conference on Localization, Interaction and Transport Phenomena in Impure Metals, Suppl.*, (PTB, Braunschweig, 1984).

Skocpol, W.J., P.M. Mankiewich, R.E. Howard, L.D. Jackel, D.M. Tennant, and A.D. Stone, Phys. Rev. Lett. **56**, 2865 (1986).

Skocpol, W.J., P.M. Mankiewich, R.E. Howard, L.D. Jackel, D.M. Tennant, and A.D.

Stone, Phys. Rev. Lett. **58**, 2347 (1987).

Stone, A.D.,,Phys. Rev. Lett. **54**, 2692 (1985).

Stone, A.D., "Universal Conductance Fluctuations and Quantum Interference Effects in Microstructures,", chapter in *Physics and Technology of Submicron Structures*, Springer Series in Solid-State Sciences, vol. 83, eds. H Heinrich and F. Kuchar (Springer-Verlag, Berlin Heidelberg 1988).

Stone A.D., and Y. Imry, Phys. Rev. Lett. **56**, 189 (1985).

Stone, A.D., and A. Szafer, IBM J. Res. Develop. **33**, 384 (1988).

Takayama, H., Z. Phys. **263**, 329 (1973).

Taylor, R.P., L. Eaves, P.C. Main, G.P. Whittington, S. Thoms, S.P. Beaumont, and C.D.W. Wilkinson, *Proceedings of the International Conference on the Application of High Magnetic Fields in Semiconductor Physics*, Wurzburg, August 1986 [Springer-Verlag (1987)].

Thompson, R.S., Phys. Rev. **B 1**, 327 (1970).

Thornton, T.J., M. Pepper, H. Ahmed, G.J. Davies and D. Andrews, Phys. Rev. **B 36**, 4514 (1987).

Thouless, D.J., Phys. Rev. Lett. **39**, 1167 (1977).

Timp, G., A.M. Chang, J.E. Cunningham, T.Y. Chang, P. Mankiewich, R. Behringer, and R.E. Howard, Phys Rev. Lett. **58**, 2814 (1987).

Timp, G., P.M. Mankiewich, P. deVegvar, R. Behringer, J.E. Cunningham, R.E. Howard, H.U. Baranger, and J.K. Jain, "Suppression of the Aharonov-Bohm Effect in the Quantized Hall Regime," preprint (1988).

Umbach, C.P., S. Washburn, R.B. Laibowitz, and R.A. Webb, Phys. Rev. **B 30**, 4048 (1984).

Umbach, C.P., C. Van Haesondonck, R.B. Laibowitz, S. Washburn and R.A. Webb, Phys. Rev. Lett. **56**, 386 (1986).

Umbach, C.P., P. Santhanam, C. Van Haesondonck, and R.A. Webb, Appl. Phys. Lett. **50**, 1289 (1987).

Van Albada, M.P., and A. Lagendijk, Phys. Rev. Lett. **55**, 2692 (1985); Wolf, P., and G. Maret, Phys. Rev. Lett. **55**, 2696 (1985).

Van Haesendonck, C., J. Vranken, and Y. Bruynseraede, Phys. Rev. Lett. **58**, 1968 (1987).

Van Haesendonck, C., J. Vranken, and Y. Bruynseraede, "Spin-Glass Transition and Resonant Kondo Scattering in Weakly Localized Metal Films," article in *Anderson Localization: Proceedings of the International Symposium*, Tokyo, Japan, 1987 (Springer-Verlag).

Washburn, S., IBM J. Res. Develop. **32**, 335 (1988).

Washburn, S., and R.A. Webb, Adv. Phys. **35**, 375 (1986).

Washburn, S. C.P. Umbach, R.B. Laibowitz, and R.A. Webb, Phys. Rev. **B 32**, 4789 (1985).

Webb, R.A., S. Washburn, C.P. Umbach, and R.B. Laibowitz, Phys. Rev. Lett. **54**, 2696 (1985a).

Webb, R.A., S. Washburn, C.P. Umbach, and R.B. Laibowitz, in *SQUID '85- Proceedings of the conference on Superconducting Quantum Interference Devices and their Applications*, Eds., H.D. Hahlbohm and H. Lubbig, (Walter de Gruyter and Co., Berlin 1985b).

Wind, S., Ph.D. Thesis, Yale University (1987).

Wind, S., M.J. Rooks, V. Chandrasekhar, and D.E. Prober, Phys. Rev. Lett. **57**, 633 (1986).

Wisnieff, R.L., Ph.D. Thesis, Yale University (1987).

Yosida, K., Phys. Rev. **106**, 893 (1957).

Ziman, J.M., *Electrons and Phonons*, Oxford University Press (1960).

Ziman, J.M., *Principles of the Theory of Solids*, Cambridge University Press (1964).

Ziman, J.M., *Elements of Advanced Quantum Theory*, Cambridge University Press (1969).